Pseudo Halide Vapor Phase Epitaxy Growth of GaN Crystals

DISSERTATION

zur Erlangung des akademischen Grades

doktor rerum naturalium

(Dr. rer. nat.)

im Fach Physik

eingereicht an der

Mathematik-Naturwissenschaften Fakultät

Humboldt Universität zu Berlin

von

M.Sc. Krzysztof Kamil Kachel

Präsident der Humboldt-Universität zu Berlin:

Prof. Dr. Jan-Hendrik Olbertz

Dekan der Matematisch-Naturwissenschaftlichen Fakultät:

Prof. Dr. Elmar Kulke

Gutachter:

1. Dr. hab. Michał Boćkowski
2. Prof. Roberto Fornari
3. Prof. Dietmar Siche

Tag der mündlichen Prüfung: 13.03.2015

Abstract

Gallium nitride (GaN) is a semiconductor with a great potential for many device applications. It has a direct wide band gap of 3.4 eV at room temperature which corresponds to 365 nm wavelength. However, the doping of the crystals for semi insulating (SI) properties remains still a great challenge. It is crucial for making the GaN crystals suitable for high power electronics.

Within the frame of this work the pseudo halide vapor phase epitaxy process (PHVPE) was developed for GaN crystals growth. The process is based on cyanide as a transport agent for Ga. The source of HCN was the reaction of hot NH_3 with either graphite or gaseous carbon precursor. Source of reactive nitrogen was NH_3.

In the first approach the reactor made of graphite was used. In this case growth rates of 60 $\mu m/h$ were achieved. Additionally, the crystals exhibit poor quality with high V-pit density.

The second approach was to provide the reactor with pyrolytical boron nitride covered parts. Changing the concept helped to improve the crystals' quality but simultaneously reduced drastically the growth rate, due to the lack of sufficient supply of Ga transport agent.

Newly designed graphite free setup is used in the third approach for PHVPE. In this case HCN forms during Degussa process on Pt catalyst inside the growth reactor. For investigation of the reaction paths, an in-situ exhaust gas measurement system based on FTIR was developed. GaN crystals were grown on sapphire and $\beta - Ga_2O_3$ substrates, AlN/Al_2O_3 and GaN/Al_2O_3 templates. Self separation was achieved for thick GaN crystals grown on $\beta - Ga_2O_3$.

The samples were characterized by various methods i.e. x-ray diffraction spectroscopy (XRD) and electron back scattering diffraction EBSD for crystal quality and crystallographic orientation, transmission electron microscopy (TEM) for investigating disloca-

tions and interface between GaN and $\beta - Ga_2O_3$, scanning electron microscopy (SEM) for surface morphology and layer thickness, energy dispersive x-ray spectroscopy (EDX) for crystals compositions, ex-situ and in-situ exhaust gas analysis by Fourier transform infrared spectroscopy (FTIR) for investigation of the reaction paths.

Kurzfassung

Galliumnitrid (GaN) ist ein Halbleiter mit großem Anwendungspotenzial für viele Bauelemente. Es hat bei Raumtemperatur eine breite direkte Bandlücke von $3,4\ eV$, was einer Wellenlänge von 365 nm entspricht. Das Dotieren der Kristalle, damit diese semi-isolierend (SI) werden, bleibt jedoch eine große Herausforderung. Es ist wesentlich, damit die GaN-Kristalle für die Leistungselektronik geeignet werden.

Im Rahmen dieser Arbeit wurde der pseudo-halogenide Gasphasenepitaxie (PHVPE) -Prozess für die GaN-Kristallzüchtung entwickelt. Dieser Prozess basiert auf dem Zyanid als Transportmittel für Ga. Das HCN wurde aus der Reaktion von heißem NH_3 entweder mit Graphit oder einem gasförmigen Kohlenstoffträger gewonnen. Als Quelle für reaktiven Stickstoff diente NH_3. Im ersten Ansatz wurde ein Reaktor aus Graphit genutzt. In diesem Fall wurden Wachstumsraten von 60 $\mu m/h$ erreicht. Außerdem zeigte der Kristall eine geringe Perfektion mit hoher V-Grubendichte.

Im zweiten Ansatz bestand der Reaktor aus mit pyrolytischem Graphit beschichteten Teilen. Diese Änderung des Konzeptes half die Kristallqualität zu verbessern, reduzierte aber gleichzeitig die Wachstumsrate drastisch, weil das Ga-Transportmittel nicht mehr ausreichend zur Verfügung stand.

Der neu konstruierte, graphitfreie Aufbau stellt den dritten Zugang zur PHVPE dar. In diesem Fall entsteht HCN während eines Degussa-Prozesses am Pt-Katalysator im Züchtungsreaktor. Zur Untersuchung der Reaktionswege wurde ein FTIR-basiertes in-situ Abgasmesssystem entwickelt. GaN-Kristalle wurden auf Saphir und $\beta - Ga_2O_3$ Substraten, AlN/Al_2O_3 und GaN/Al_2O_3 Templates gezüchtet. Eine Selbstseparation wurde für dicke GaN-Schichten auf $\beta - Ga_2O_3$ erreicht.

Die Proben wurden mit verschiedenen Methoden charakterisiert, z.B. mit der Röntgenbeugungs-Spektroskopie (XRD) und Elektronenrückstreubeugung (EBSD) für die Kristallperfektion und kristallographische Orientierung, der Transmissionselektronenmikroskopie

(TEM) zur Untersuchung von Versetzungen und der Grenzfläche zwischen GaN und dem $\beta - Ga_2O_3$, der Rasterelektronenmikroskopie (REM) für die Oberflächenmorphologie und Schichtdicke, der energiedispersiven Röntgenspektroskopie (EDX) für die Kristallzusammensetzung, sowie der ex-situ und in-situ Abgasanalyse mit der Fourier-Transform-Infrarotspektroskopie (FTIR) zum Studium der Reaktionswege.

Contents

1 Introduction

The wide band gap compound semiconductor GaN is recognized, at least since the Nobel prize was awarded in 2014, as the basic material to revolutionize general lighting. But it has also enormous potential at saving energy in high power and high frequency devices. This is why GaN is recently one of the most studied materials. As shown in Fig. 1.1

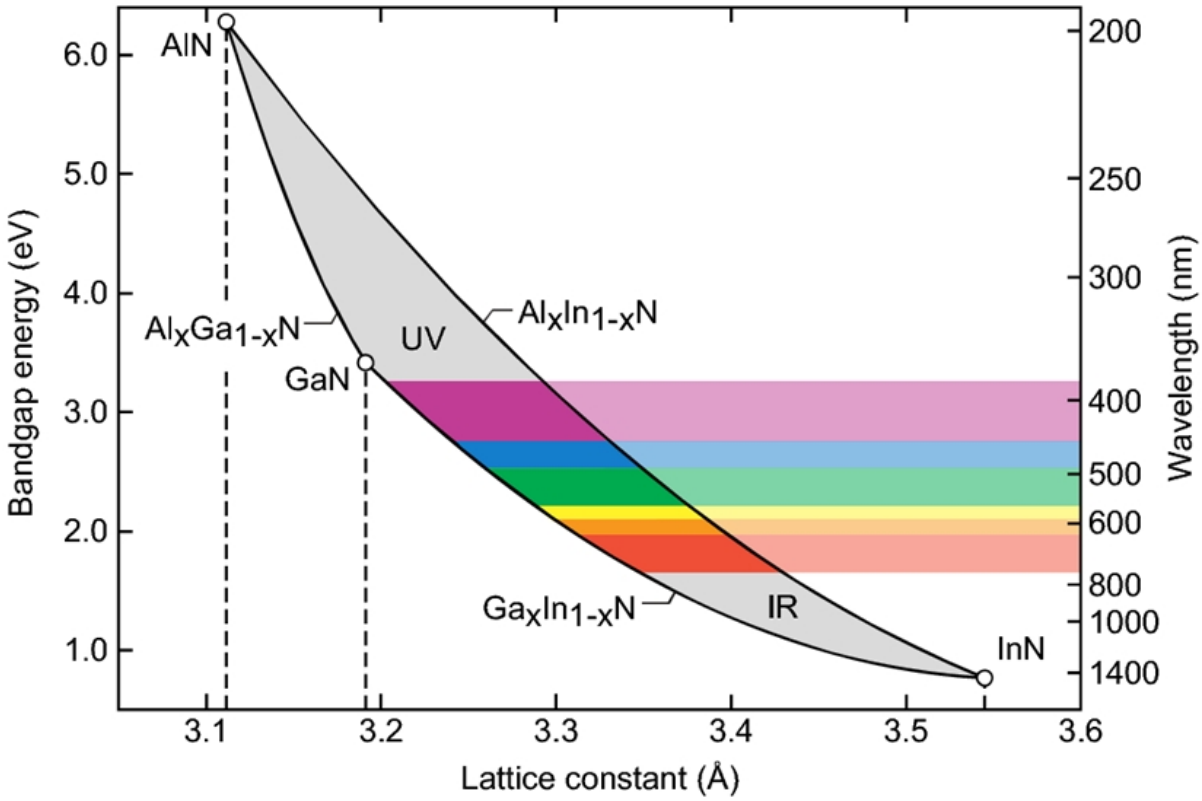

Figure 1.1: Band gap vs. lattice constant for (Al, Ga, In) - Nitrides [1]

(Al, Ga, In) - nitrides can illuminate at any wavelength in the visible spectrum range. Therefore, for applications as laser diodes (LD) or light emitting diodes (LED) using GaN is advantageous.

The second field of applications is due to the wide band gap and other unique properties such as high temperature stability and chemical resistivity. Devices in this area are high power (HP) transistors and high-frequency devices e.g. monolithic microwave integrated circuit (MMIC). GaN high electron mobility transistor (HEMT) based device structures show great potential as gas detectors and micro-Hall effect sensors due to presence of two-dimensional electron gas (2-DEG) on $AlGaN/GaN$ heterointerface [2, 3].

For the applications described above epitaxial layers of GaN grown on foreign substrates such as: SiC, Al_2O_3 or Si, exhibit satisfactory properties and the use of the expensive native bulk substrates is not necessary. Nevertheless, for multi-quantum wells LDs native GaN substrates are a prerequisite. Moreover, the substrates must be of high crystalline quality i.e. structurally flat (radius of lattice bow $> 30\ m$ for 2" substrates [4]) and low threading dislocations densities ($TDD << 10^6$) [5, 6]. Additionally, according to Soraa, Inc., US manufacturer of GaN-based LEDs, GaN substrates enable much simpler epitaxial structures compared to e.g. epitaxial lateral overgrowth (ELO), which makes LED devices more cost-efficient compared to devices on sapphire or silicon.

To reduce cost of single device the diameter of native crystals should be as high as possible. For commercial power electronics industry the minimum substrate size is 4". It is also necessary to provide different types of the substrates from highly $n-$type to semi-insulating (SI).

Nowadays only 1" diameter native substrates grown by ammonothermal solution growth (AT), fulfilling above mentioned structural prerequisites, are commercially available at a limited number and extremely high prices. Due to lack of a satisfactory technique to grow truly bulk GaN in industrially preferred sizes by AT, the most of commercially available substrates up to 6 in are grown by the halide vapor phase epitaxy ($HVPE$), usually on sapphire as native substrates are not available. Due to the high growth rate $> 200\ \mu m/h$ HVPE is currently most used technique for growth of GaN crystals.

The crystals grown by classical $HVPE$ are usually n-type conductive, due to the unintentional doping with oxygen and Si impurities [7] from the quartz parts of the growth reactor. To achieve $SI\ GaN$ it is necessary to compensate the parasitic doping with either iron, magnesium or carbon [8, 9, 10, 11, 12]. In this method it is challenging, due to high reactivity of the *chloride*-compounds.

Therefore, the approach of this work was to investigate and establish the pseudo-$HVPE$ ($PHVPE$) process based on cyanide (CN^-) instead of chloride (Cl^-) chemical transport of Ga for growing carbon doped GaN crystals. Previous work at the IKZ already proved that the grown layers exhibit SI properties due to carbon incorporation.

The focus of the work, however, is not on the doping process and incorporation behavior, but rather on the development of a viable and controllable growth process. That is why two general approaches to grow GaN by $PHVPE$ were studied. First one, based on graphite as the source of carbon and the second one graphite-free, with methane (CH_4) as a gaseous carbon precursor. The growth of GaN on different substrates and templates in a graphite containing $PHVPE$ setup is also described. Part of the work is concentrated on developing an in-situ exhaust gas measurement system, based on a Fourier transform infrared spectroscopy ($FTIR$). The preliminary GaN growth results, in the newly designed graphite-free growth reactor, are shown as well.

2 Theoretical background

2.1 GaN properties

GaN is a semiconductor with direct band gap of 3.4 eV at room temperature. It is highly resistive for wet etching used for processing classical semiconductors. At high temperature it dissolves in alkali solutions at very slow rate. Nevertheless, low quality material could be etched at reasonably high rate in $NaOH$, H_2SO_4, and H_3PO_4 [13]. Besides the chemical stability GaN also is very hard and mechanically stable. Above described parameters are advantageous for the devices application, but at the same time they are disadvantageous for processing of devices. Classical methods known from Si-industries do not work for GaN e.g. all etching processes have to be done with plasma, which increase the cost of the wafers processing.

The high critical breakdown field allows the GaN-based devices to work at much higher voltages and lower leakage currents as compared to Si-based devices. Electron mobility and electron saturation velocity higher than in both Si and SiC are advantageous in high frequency devices.

All above described unique properties of GaN crystals combined with its wide and direct bandgap make it the best choice for many device applications.

GaN does not melt stoichiometrically at moderate pressure. The results published by Utsumi et al. [16] set the melting point temperature of GaN at $T_m > 2220°C$ at an N_2 pressure of $p > 6\ GPa$. An explanation why GaN could be melted only at such high pressure is that the bonding energy of GaN compound is 9.12 eV [17], which is very strong in comparison to the other classical semiconductors such as: $GaAs$ - 2.1 eV [18],

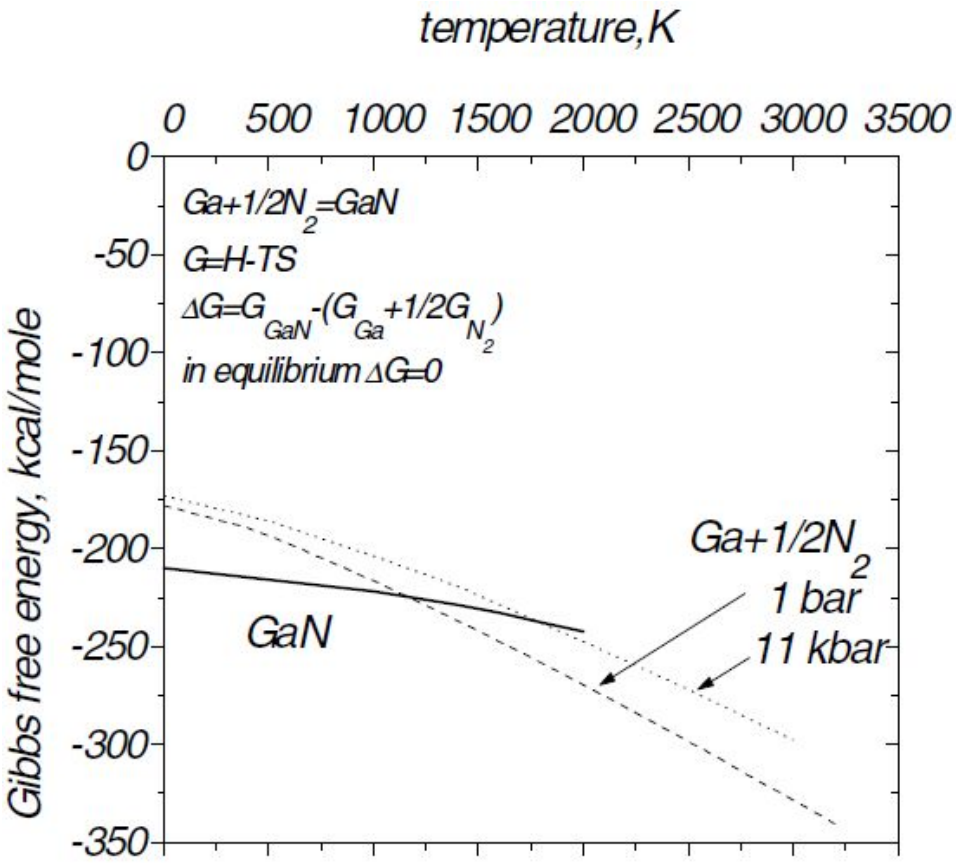

Figure 2.1: Gibbs free energy of GaN and its constituents [14]

SiC - 3.66 eV [19]. Nevertheless, the bonding energy of the N_2 molecule is also very strong - the strongest bonded diatomic molecule - 9.8 eV [20]. Therefore, the GaN is stable until $\sim 800°C$ at atmospheric pressure. On the other hand, the function of the Gibbs free energy depends strongly on the temperature:

$$G(p,T) = U + pV - TS \tag{1}$$

Where:

U is the internal energy

p is pressure

V is volume

T is the temperature

S is the entropy.

The Gibbs free energy of GaN decreases slower than of its constituents. Therefore, at higher temperatures GaN become thermodynamically unstable. It means that the existence of the N_2 molecule is of higher probability than GaN [21]. This behavior is shown in Fig. 2.1 [14]. The equilibrium curve of GaN - pressure vs. temperature determined by Karpinski et al. [15] is shown in Fig. 2.2.

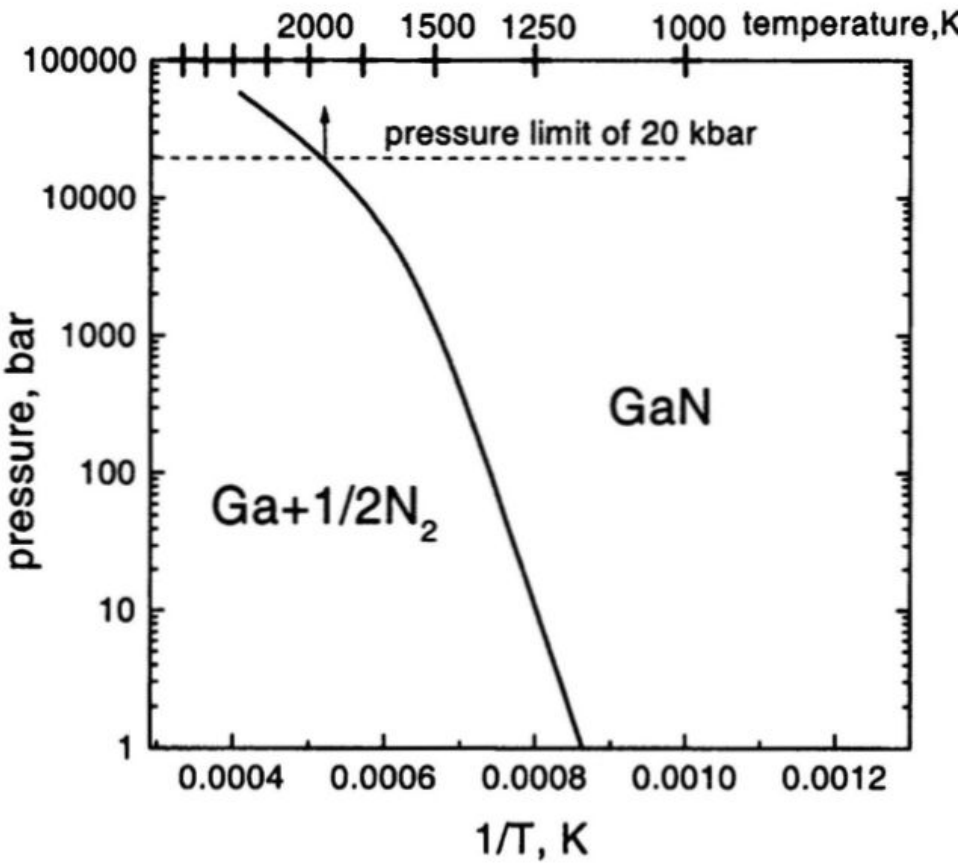

Figure 2.2: Equlibrium curve for GaN [15]

2.1.1 GaN crystal structure

The GaN crystallizes in wurzite, zinc-blende [23] or rock-salt [24] structure. Nevertheless, the first one exhibit the most interesting properties and is the most stable at reasonable temperatures and pressures and therefore, most wanted structure, thus it will be of interest for the work presented here.

Wurzite GaN represents the space group $C_{6v}^4 - P63mc$. As it is shown in Fig. 2.3, it has clear hexagonal structure with the lattice parameters $a = b = 3.189$ $\mathring{A}$ and $c = 5.185$ $\mathring{A}$.

In the wurzit structure, each atom of gallium is bonded with four neighboring atoms of nitrogen, for nitrogen atoms the situation is adequate. Views are shown in Fig. 2.4 from the different sides of GaN crystal.

Due to the fact that wurzit GaN has no inversion center, it is possible to distinguish between polar, non-polar and semi-polar plane. There are two polar surfaces that are both perpendicular to the c and $-c$ directions. Non polar planes are represented by m and a planes perpendicular to the a and $-a$, $a + b$ and $-a - b$ directions respectively.

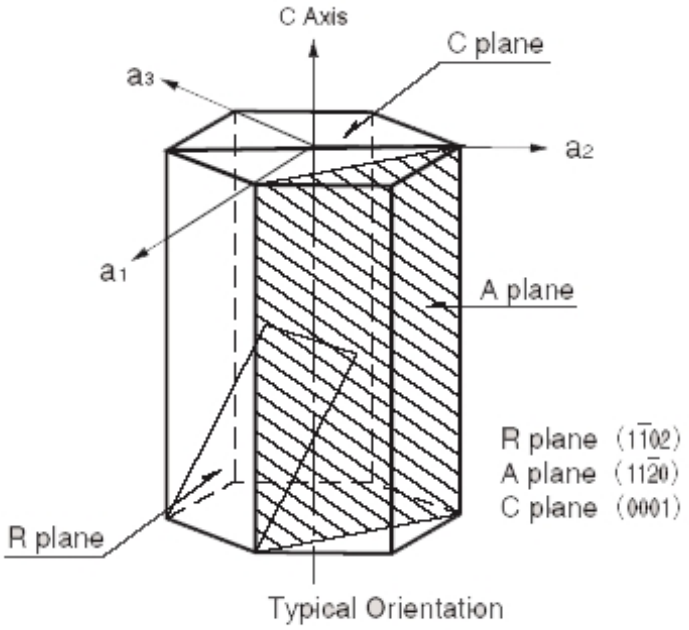

Figure 2.3: Hexagonal structure of GaN [22]

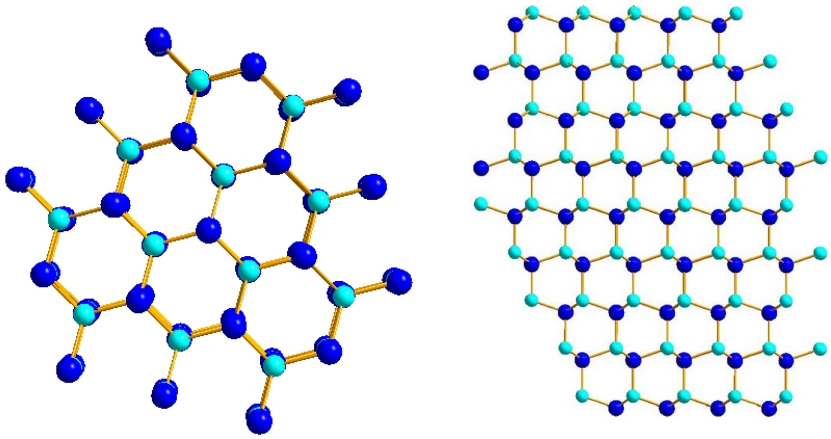

(a) c - plane view

(b) a - plane view

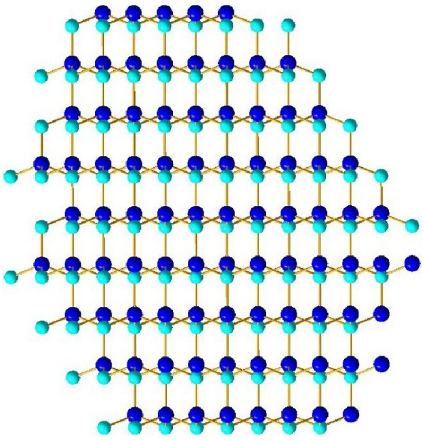

(c) m - plane view

Figure 2.4: Lattice structure of GaN - different views. Light blue colour corresponds to Ga atoms, dark blue corresponds to N atoms

Semipolar planes are represented by r plane, the predominant semipolar planes are all those, that could be defined between c planes and m planes defined as $(10\bar{1}n)$.

Moreover, there is a division of the polar plane $+/-$ c for two different axes of view - nitrogen or gallium polarity respectively. The difference between these two surfaces is denoted by the fact that either gallium or nitrogen atoms are on top of the unit cell. The difference of the crystal structure is shown in Fig. 2.4b with Ga atoms on top of the structure, what make it the gallium-polar plane, and Fig. 2.4c with N atoms on top

which make it the nitrogen-polar plane.

The different polarity of GaN will affect properties of the crystal when grown or probed on these planes such as: growth rates, etching, defect generation, plasticity, and piezoelectricity [25, 26]. As an example of its influence on the growth, the growth rate of the crystal is significantly different for the N and the Ga plane. The growth is slower on the $N - polar$ plane as has been reported by Northrup et al. [27]. Moreover, the incorporation of the doping elements depends strongly on the crystal polarity. The semi-polar planes, that are exposed at the beginning of the growth - before 2D growth starts, are adsorbing and incorporating much more doping elements as compared to the Ga polar plane. This also leads to high non-homogeneity in the crystal structure [28] in terms of e.g. dopands level and carriers concentration.

2.2 Growth methods

Today it is technologically not possible to grow GaN just from the melt using e.g. Czochralski or floating zone techniques, due to the high temperature melting point under extremely high N_2 pressure. Therefore, GaN is grown by the techniques in which such a high pressure is not necessary, i.e. either from solution or gas phase, eventually with combination of this both methods. In case of growth from solution high pressures are required although they are significantly lower than the pressure required for stoichiometrical melting of GaN. In all three solution growth methods described below using the high pressure has other physical purpose.

2.2.1 Solution growth techniques

High Nitrogen Pressure Solution Growth

In case of High Nitrogen Pressure Solution Growth (HNPS) the high pressure is used to dissolve nitrogen into the Ga melt. It is a temperature gradient method in which the highest crystal qualities in terms of threading dislocation density (TDD) in the range of $TDD = 10 - 10^2\ cm^{-2}$ are obtained [30]. In this method, the crystals grow closest to

equilibrium as compared to all of the growth techniques. The method based on a direct reaction between liquid Ga and gaseous N_2 at an extremely high pressure of nitrogen gas $p = 10 - 20$ $kbar$ and temperature up to $1500°C$ [14, 31, 32], a scheme of a crucible is shown in Fig. 2.5.

The principle of this method is to dissociate N_2 molecules on Ga surface and dissolve them in the metal. Due to implementation of the temperature gradient a nitrogen supersaturation occurs in the Ga melt at the colder (bottom) part of the crucible and therefore, GaN crystallizes on the bottom of the crucible, either spontaneously or on the seed. The mass transport in this method is provided by the convection inside the solution.

The limitation of HNPS method is the scalability of the reactor, due to the extremely high pressure it is dangerous and technically difficult. Moreover, the growth rates are

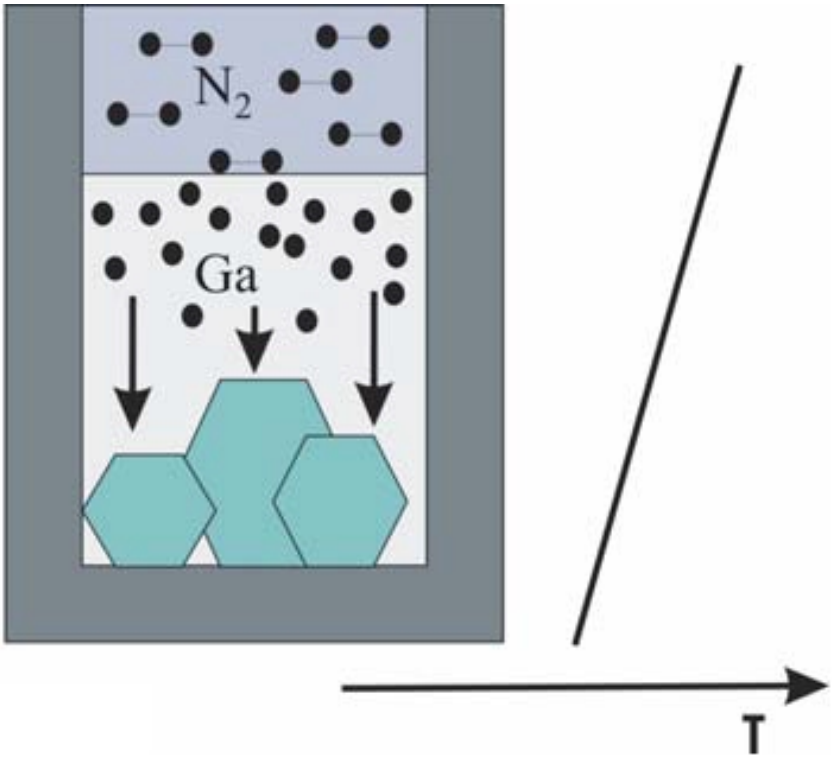

Figure 2.5: Schematic illustration of the crystallization of GaN from the solution in a temperature gradient [29]

very low - about 2 $\mu m/h$ [32].

Growth from Na-flux

Similar to HNPS, in case of Na-flux high pressure is required to provide supersaturation in the flux. Na-flux growth is a kind of liquid phase epitaxy (LPE). It is based on the phenomenon of increased solubility of N_2 in Ga if it is mixed with sodium. It is also discovered that adding Ca and Li to the $Ga-Na$ mix increases the solubility of N_2 [34]. This method requires N_2 pressures of $20-50$ bar at a temperature of approx. $T = 750°C$ [35, 36]. Growth rate is in the range of 20 $\mu m/h$ [37].

In Fig. 2.6, the sketch of the growth principle is presented. The $Ga-Na$ melt is kept in an Al_2O_3 ceramic crucible. On the bottom of the crucible, a MOCVD grown

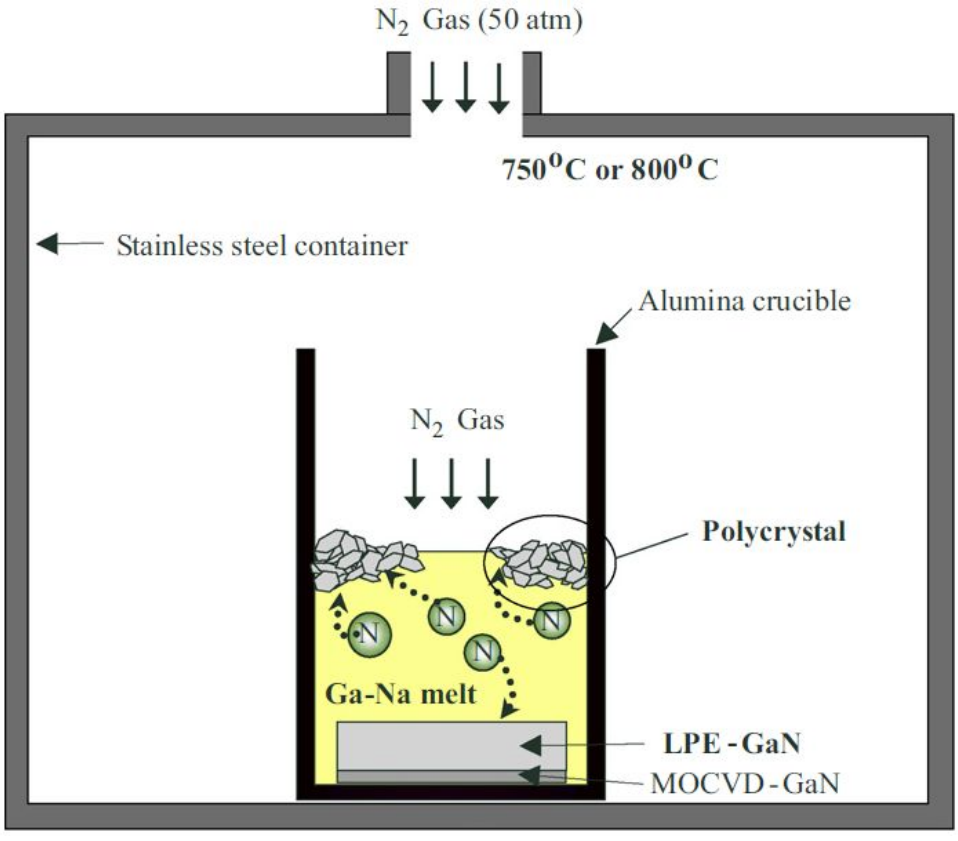

Figure 2.6: Scheme of the Na-flux LPE [33]

GaN/Al_2O_3 template is placed. N_2 gas is introduced under pressure into the stainless steel container. Aided by the Na content, nitrogen is dissolved in the melt solution. Gallium atoms interact with nitrogen, and due to the temperature gradient between the surface and bottom of the melt, the supersaturation leads to GaN crystallization on the GaN/Al_2O_3 template. High supersaturation near gas-liquid interface causes the parasitic generation of polycrystals as shown in Fig. 2.6.

In contrast to HNPS the mass transport is obtained by stirring of the solution, not by thermal convection. Interesting aspect of this growth technology is that the flow velocity can be increased by a factor of 30 just by stirring the solution [36], which is in fact introduced by a seesaw motion of the whole growth chamber.

Ammonothermal solution growth

In contrast to two previously described growth methods in this case high pressure is required to obtain supercritical ammonia, which is necessary to dissolve GaN.

Nowadays, the ammonothermal solution growth (AT) method is the only one supplying high quality substrates up 1" to for epitaxy.

AT is similar to the hydrothermal method for quartz crystallization, but the water is replaced by supercritical ammonia. The working principle is based on the dissolution of GaN in supercritical NH_3 enhanced by a mineralizer. There are two choices of mineralizers. It might facilitate formation of either basic NH_2^- [38] or acidic NH_4^+ [39]. The big advantage of using ammonobasic mineralizers over the ammonoacidic is that the solubility of GaN in NH_3 is retrograde i.e., higher at lower temperatures. Therefore, it is possible to grow crystals at higher temperatures, which has some advantages from the technological point of view.

In Fig. 2.7 the scheme of autoclave for crystal growth with ammonobasic AT method is shown. In the upper area of the autoclave the feedstock of GaN is placed in a temperature zone T_1. It is gradually dissolved in the supercritical ammonia and transported to the zone of the temperature T_2. When $T_2 > T_1$, due to using ammonobasic mineralizer, GaN starts to grow on the seeds placed in the higher temperature zone. Retrograde

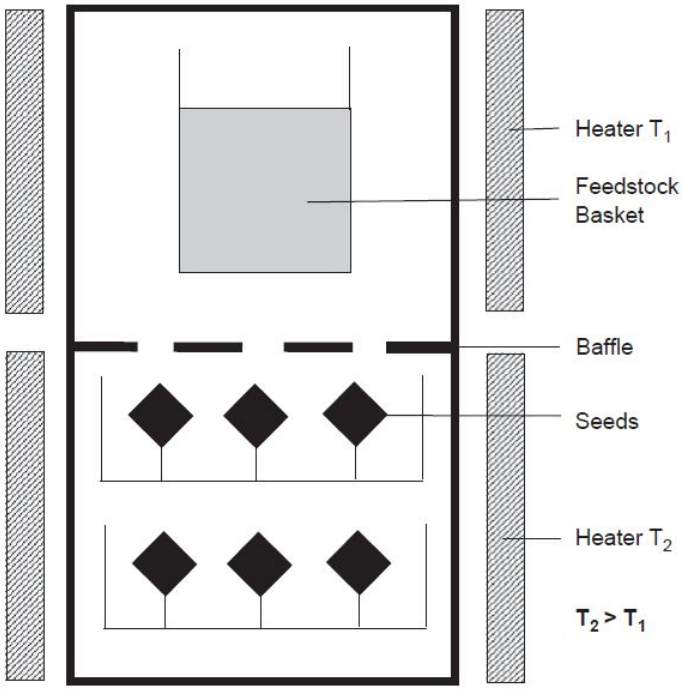

Figure 2.7: Scheme of an autoclave for the ammonobasic AT method [40]

solubility allows to decrease temperature in the autoclave on the feedstock side and therefore, supercritical ammonia does not attack autoclave parts as strong as in higher temperature. Moreover, basic conditions allow to use less expensive ceramic parts instead of expensive Pt. One of the biggest disadvantages of this method is the low growth rate of approx. $1-4\ \mu m/h$ [41]. Nevertheless, the threading dislocation densities (TDD) stay at the very low level of $TDD = 10^3\ cm^{-2}$ [42]. Moreover, $p-$ and $n-$ type substrates could be grown. Typical carrier densities for both n-type and p-type are in range of $10^{17} - 10^{18}\ cm^{-3}$ and can be controlled by doping [40].

2.2.2 Gas phase growth techniques

In contrast to the solution growth techniques growing from the gas phase does not require pressures higher than 1 bar. Reactive nitrogen is supplied by the gaseous precursor which is ammonia in HVPE and MOCVD. In case of molecular beam epitaxy (MBE) or its most

common version - plasma assisted MBE (PAMBE) the reactive nitrogen is produced by plasma source (usually radio frequency plasma). The MBE is an ultra high vacuum technique (pressure in range of $p = 10^{-6}\ mbar$), where Ga transport is based on the ballistic effect. In the MBE the growth temperatures are low $T_{gr} = 650 - 800°C$ [43]. The conditions used for MBE growth processes makes it far from equilibrium technique and therefore it will not be described here.

Halide Vapour Phase Epitaxy

Halide vapor phase epitaxy is the growth technique used to produce commercially available free-standing GaN substrates up to 6" with TDD in the range of $\sim 10^6\ cm^{-2}$ in case of heteroepitaxy on sapphire substrates with epitaxial lateral overgrowth (ELO) and masking techniques to reduce the TDD and improve crystal quality [45]. On the other hand, homoepitaxial GaN growth by HVPE on AT grown GaN was reported very recently by Sochacki et al. [46]. Authors presented a 1" diameter crystal with $TDD \sim 10^4\ cm^{-2}$. They claim, that growth by HVPE does not introduce new dislocations in comparison to the substrate. It proves, that the quality of crystals grown by HVPE depends

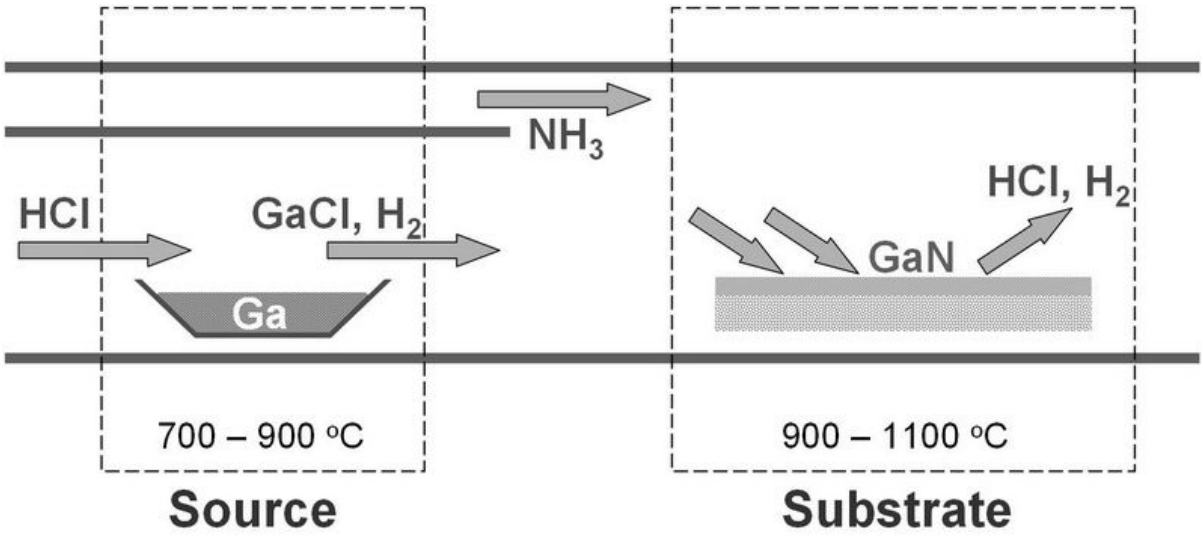

Figure 2.8: Scheme of the HVPE for GaN growth [44]

mostly on the substrate material. It is the fastest technique for growing GaN crystals. Most commonly the HVPE reactors are made in horizontal arrangement. Nevertheless there are also groups working with vertical designed reactors [47, 48].

The working principle of HVPE is schematically presented in the Fig. 2.8. In usual reactors there are two heating zones: Ga source zone and substrate zone.

The first one is colder and stays at the temperature in the range of $T = 800 - 900°C$. In this zone, the gaseous HCl flows over metallic Ga. HCl reacts with Ga on its surface and forms gaseous (at this temperatures) $GaCl$ molecules:

$$2Ga(l) + 2HCl(g) \rightarrow 2GaCl(g) + H_2(g) \tag{2}$$

The next step is the reaction to form GaN. Due to very rapid reaction between $GaCl$ and NH_3 those compounds are mixed next to the substrate which is kept usually at temperature of $T = 900 - 1100°C$ depending on the process [49, 50]. Here the reaction to form GaN occurs:

$$GaCl(g) + NH_3(g) \rightarrow GaN(s) + HCl(g) + H_2(g) \tag{3}$$

Drawback of the HVPE method is parasitic GaN nucleation on the outlet of $GaCl$ supply lines. Depending on the reactor design it might either decrease flow of Ga precursor, limiting the growth rate, or even completely block the flow of $GaCl$. The second drawback is NH_4Cl formation in the exhaust line and the filters, deposited in the exhaust line in front of the pump. Both obstacles reduce the possible growth time significantly. Moreover, there is the requirement of time consuming cleaning of the line after each process and filter after each $60 - 200$ h of the process, depending on the filter size and design.

Additionally, in the HVPE large amounts HCl and NH_3 are used and only a small percentage reacts to GaN. Therefore, the exhaust gas must be filtered and stored or neutralized [23, 33].

Metal Organic Chemical Vapour Deposition

The metal organic chemical vapor deposition (MOCVD) is the commonly used technique for GaN based device epitaxy. The principle of MOCVD is based on chemical transport of Ga by trimethylgallium - $Ga(CH_3)_3$ (TMG) and reaction on the surface of the substrate with ammonia to form GaN [52].

Wide choice of precursors for many different substances such as: trimethylaluminum (TMA), trimethylindium (TMI), silan (SiH_4), bis-cyclopentadienyl magnesium ($CP_4 - Mg$), etc. gives the opportunity to deposit not only GaN but also ternary compounds such as: $AlGaN$ [53], $InGaN$ [54] or $InAlN$ [55]. Moreover, using SiH_4 or $CP_4 - Mg$

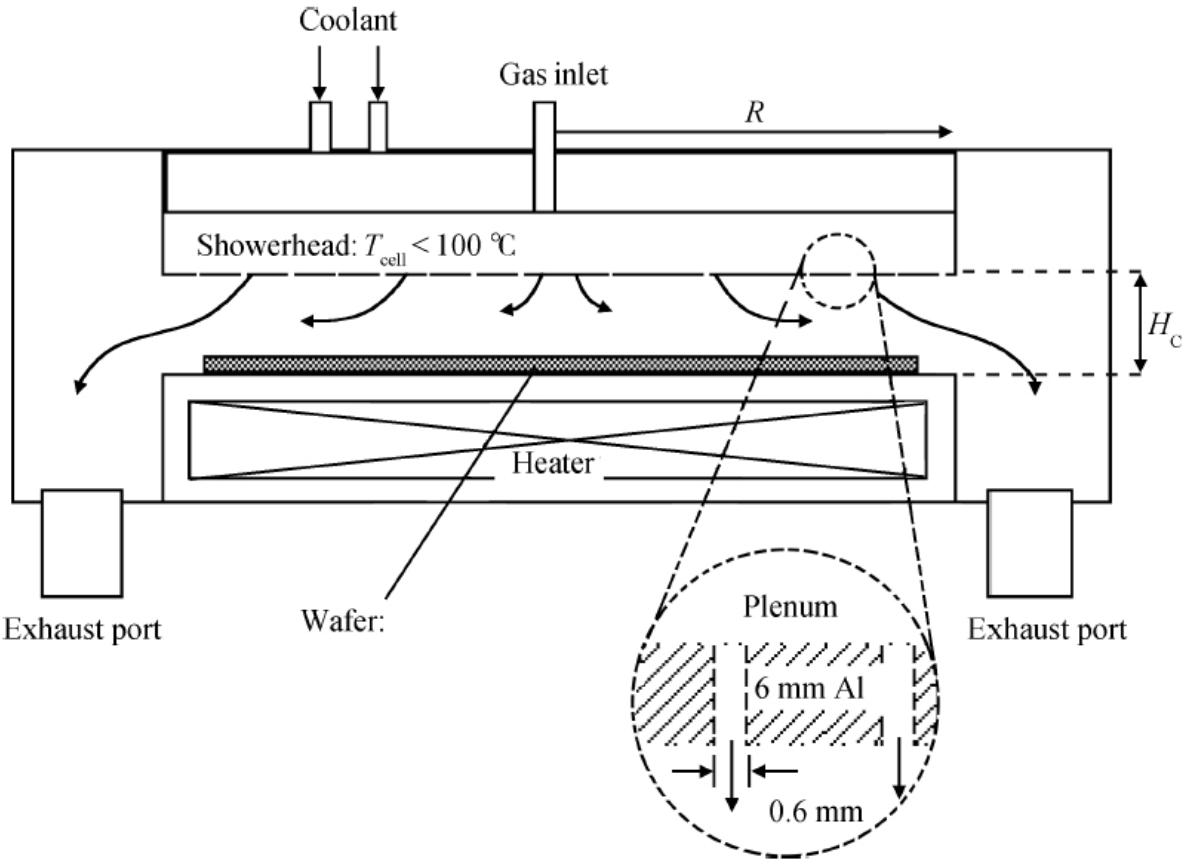

Figure 2.9: Schematic of the showerhead MOCVD reactor [51]

it is possible to dope grown films for $n-$ or $p-$ type respectively. Low growth rate $< 2\ \mu m/h$ [56] enables growing layers with precisely defined thickness. Those unique properties make MOCVD the industrial technique for device fabrication such as: lasers, LED's, transistors, etc.

Commercially available growth reactors e.g. Aixtron CRIUS II-L/XL, are showerhead designed with many tubes supplying reagents to the substrates. The working principle is schematically shown in Fig. 2.9. Metal precursors: TMG, TMA, TMI, etc. are supplied by the lines placed in the showerhead together with NH_3. Reaction path could be in general described by the following balanced equation:

$$Ga(CH_3)_3(g) + NH_3(g) \rightarrow GaN(s) + 3CH_4(g) \tag{4}$$

The equation above ignores the fact that specific reaction paths and reactive species are largely unknown. The detailed reactions are not well known, but they are thought to be more complex.

To avoid the parasitic nucleation on the gas outlets, the showerhead is held at lower temperatures ($T < 100°C$). Substrates are placed on the rotating susceptor and heated up to the growth temperatures. The typical temperature of the substrate during growth of GaN is in the order of $T \sim 1000°C$ [57]. The pressure range is from $p = 10\ mbar$ up to $p = 1000\ mbar$ [56, 58, 59].

The most often used substrate for this technique is sapphire. Before growing on bare sapphire there is a necessity of substrate nitridation. In this stage, low temperature ($800°C$) AlN buffer layer forms on top of the Al_2O_3 substrate. After the nitridation GaN could be grown on top of this surface [58]. As reported by Akasaki et al. [60] 500 $\mathring{A}$ thick buffer improved quality of the grown GaN dramatically in terms of pits and grain boundaries. The possibility of growing on nitrided sapphire by MOCVD makes it suitable for preparation of the GaN template for HVPE growth.

2.3 Characterisation techniques

2.3.1 Scanning Electron Microscopy

For this work a FEI Nova 600 NanoLab dual beam system was used. It combines ultra-high resolution field emission scanning electron microscopy (SEM) and precise focused ion beam (FIB) ablation capabilities. In this configuration SEM is equipped with a secondary electron (SE) detector, electron backscatter diffraction (EBSD) system containing a phosphor screen, energy-dispersive X-ray (EDX) detector and some other devices, which are not of interest for this work and will not be discussed here.

In SEM a focused electron beam is scanning the sample. The source of electrons is a Schottky thermal field emitter, based on the thermo-emission effect. The electron beam is shaped and focused on the sample by electro-magnetic lenses. The image observed in SEM is not real. It is a virtual image - composed of the detected signal from each point from scanning -line by line area. The scanning area corresponds to the image observed on the screen. The signal depth depends on acceleration voltage and sample material.

Resolution of the microscope used for this work could reach 1.1 nm at 15 keV and 2.5 nm at 1 keV [61]. For samples measured in this work 5 and 10 keV were used.

Registered images are formed not only from the surface of the sample. Different signals could come from different depth of the sample. Depending on used detector different signals could be collected and different information could be taken out of the measurement.

SE imaging is one of the most often used device modes for characterization of the sample surface in this work. SE are generated by non elastic collisions between atoms and primary electron beam. Their energy does not exceed usually 15 eV and therefore they could escape only from a very limited thickness - up to 10 nm depth. Due to this fact the information is mostly about the surface of investigated sample and also high resolution image could be achieved. The contrast of the image gives information about the surface topology, more electrons could escape from the top of e.g. a hillock, than from some depression on the surface, and therefore the brighter points are from areas

with more convex topology than the dark ones.

Electron Backscattering Diffraction

The EBSD measurements were used to investigate the grown islands mutual orientation, as well as the homogeneity of the surface in terms of relative crystal perfection. During the EBSD measurement sample must be inclined to form a very small angle to the primary beam and detector. The electrons from the primary electron beam are mostly scattered away, but a part of them elastically scattered with the atoms of sample according to the Bragg law. A strongly magnified beam is displayed on phosphor screen and captured by charge coupled device (CCD) chip. The result of the EBSD are Kikuchi pattern. Diffractograms with Kikuchi lines consist of pairs of parallel bended lines. Each of the pairs corresponds to a given crystallographic plane [62]. Interpretation of the pattern gives the information about crystal structure of measured sample such as: orientation map with a local resolution up to 100 nm, crystal defects and grain boundaries [63].

2.3.2 Transmission Electron Microscopy

For sample characterization in this work a FEI Titan $80-300$ transmission electron microscope (TEM) operating at 300 keV and equipped with spherical aberration corrector for the objective lens was used.

Electron-matter interaction

In TEM the signal comes from an electron beam transmitted through the sample. This is possible because: 1st - the energy of primary electron beam is high ($100-300$ keV), 2nd - the sample must be very thin - usually below 100 nm. The second point limits the TEM applications, due to difficulties with sample preparation. The electrons could interact with the sample in few ways, as it is schematically shown in Fig. 2.10. They could be scattered into different diffraction cones. The aperture allows to chose the desired type of signal.

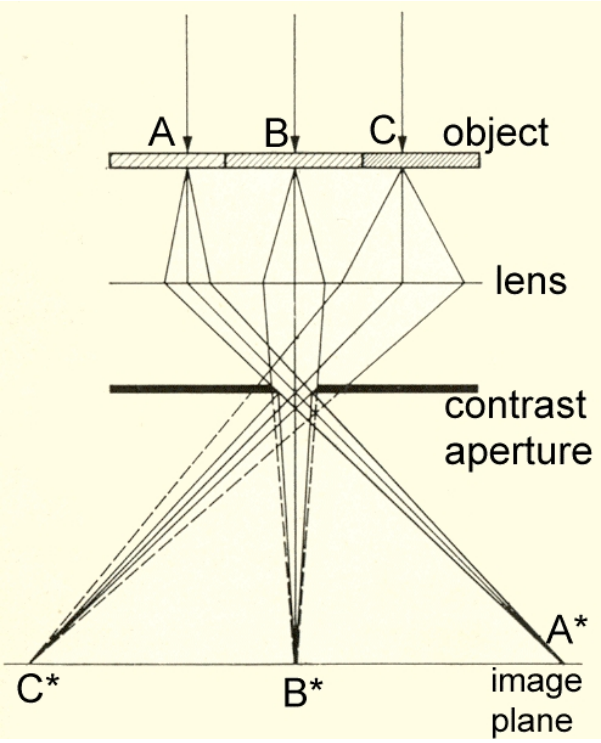

Figure 2.10: Illustration of scattering in TEM

The electrons are scattered by the atoms of the measured sample due to the Coulomb interactions between the transmitted electrons and atomic nuclei or atomic electrons. In case of the first interactions there is almost no energy transfer (approx. ~ 0.2 % of kinetic energy of the electrons is transferred to the nucleus [64]) - it is elastic scattering. On the other hand fast electrons lose a significant amount of energy while interacting with atoms' electrons - this is inelastic scattering. The part of transmitted electrons does not interact with atomic electrons neither nucleus. This part of source electrons remains unscattered.

Bright field TEM

Bright field imaging is the most common mode used for a TEM. Low magnification images were used for this work to determine the interface between GaN and $\beta - Ga_2O_3$ and the dislocations in GaN. The image contrast formation is based on electron absorption in the

sample. The aperture is placed in the back focal plane of the objective lens which allows only the direct beam to pass. Thick areas, areas in which heavy atoms are enriched, and crystalline areas appear darker.

High resolution TEM

High resolution TEM (HRTEM) is a mode in TEM that allows imaging the atomic structures of the measured samples. Image formation in HRTEM relies on phase contrast.

Phase contrast originates from shifts in the relative phases of the parts of the beam which contribute to the image. It occurs whenever more than one beam contribute to the image. In this case characteristic fringes are visible. They arise from the interference of electron waves with a difference in phase that could be found when they are scattered while passing through a thin sample. Ideally, all other scattered electrons are focused by the lens at the corresponding image points, at which they arrive in phase. The contrast is sensitive to many factors such as: sample thickness, orientation, scattering factor, changes with the astigmatism and focus of the objective lens. In HRTEM imaging, a large diameter objective aperture is used to select multiple beams to form an image containing lattice fringes that can reveal information about the atomic structure of the sample. The lattice fringes are not direct images of the atomic structure but can give information on the lattice spacing and atomic structure of the crystal. Full interpretation of the images, e.g., of the atomic structure of defects and interfaces, requires extensive computer simulation, because when an experimental image is recorded one loses phase information, and this means one cannot directly infer the atomic structure from the image.

Selected area diffraction

An important possibility of TEM is to choose the area of diffraction. In selective area diffraction (SAED) technique the aperture is placed in the desired position. In this mode the electron beam should be considered as a wave of fraction of nanometer wavelength rather than particle-like. As the distances between the atoms in crystal structure are

significantly larger the atom behaves like an obstacle that diffract the electrons. Part of the electrons is scattered to the particular angles, determined by the sample crystal structure. The other part passes the sample unscattered. With the contrast aperture shown in Fig. 2.10 it is possible to chose which part of electrons should be detected. In case of the single crystals the characteristics for crystal structure diffraction patterns are visible [65, 66].

By tilting the samples it is possible to observe diffraction patterns from different crystal orientations. Moreover, shifting the sample allows to chose exactly the area of measurement. It is possible to set it on the grown layer, substrate or on the interface. The size of detected areas is defined by the beam size, which can be changed using selected area aperture.

An advantage of this technique over x-ray diffraction (XRD) is the nanometers size of examined area while in XRD typical size is in the range of several square millimeters.

2.3.3 Fourier Transform Infrared Spectroscopy

For this work a Vector22 Bruker Fourier Transform Infrared (FTIR) spectroscope was used for developing an in-situ characterization of exhaust gases. In FTIR spectroscopy the infrared (IR) light is passed through the measured sample. The part of the light absorbed by molecules gives rise to the characteristic lines in the spectra. The received spectrum is characteristic for a defined substance. It is like a fingerprint - no two different molecules will give the same IR spectrum. This property makes FTIR interesting for this work.

Physical principles

For FTIR important is infrared region where electromagnetic radiation cause the oscillation of the molecules and more specifically the nuclei of the molecules. In Fig. 2.11, two types of oscillations - stretching and bending are presented. The stretching oscillations are characterized by reducing and increasing the distance between atoms that are chemically bounded. As shown in Fig. 2.11a, this oscillations could be further divided into

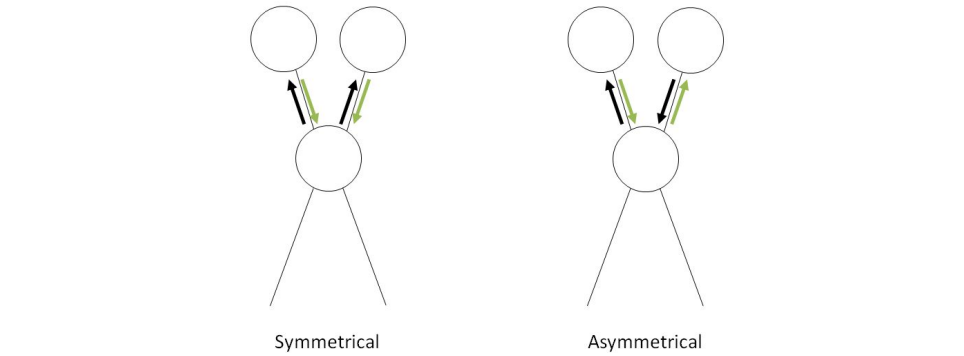

(a) stretching oscillation

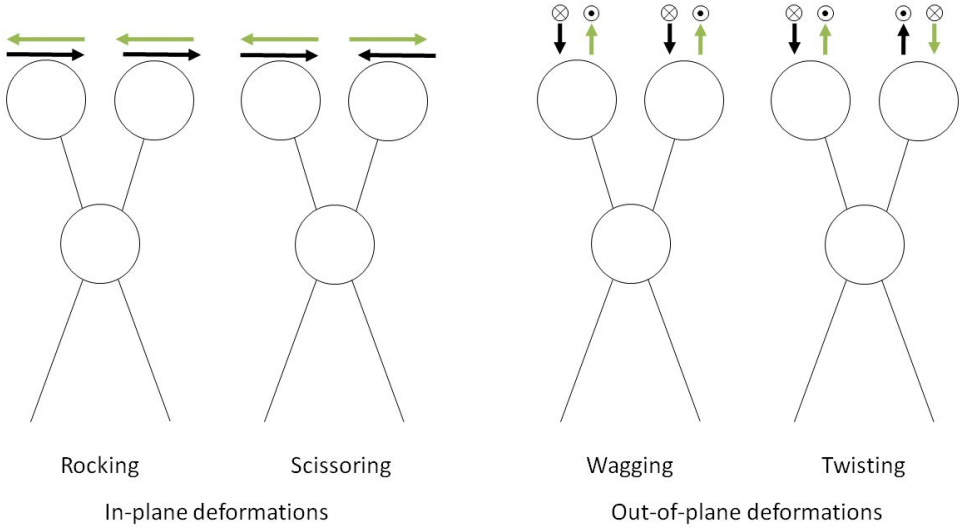

(b) bending oscillation

Figure 2.11: Classification of the oscillation caused by infrared light

symmetrical and asymmetrical dependent on whether the corresponding atoms of the molecules decrease and increase their bounding distance simultaneously or not. Second family of oscillation is bending. In this case the bonds do not stretch, but just bend. In Fig. 2.11b, two types of deformation are presented: in-plane deformation - rocking or scissoring, and out-of-plane deformation - wagging or twisting.

The oscillation of a diatomic molecule caused by infrared radiation could be considered as the classical model of the harmonic oscillator. According to Hooke's law, the restoring force of a spring (molecule bonding) is proportional to the displacement of its endpoints

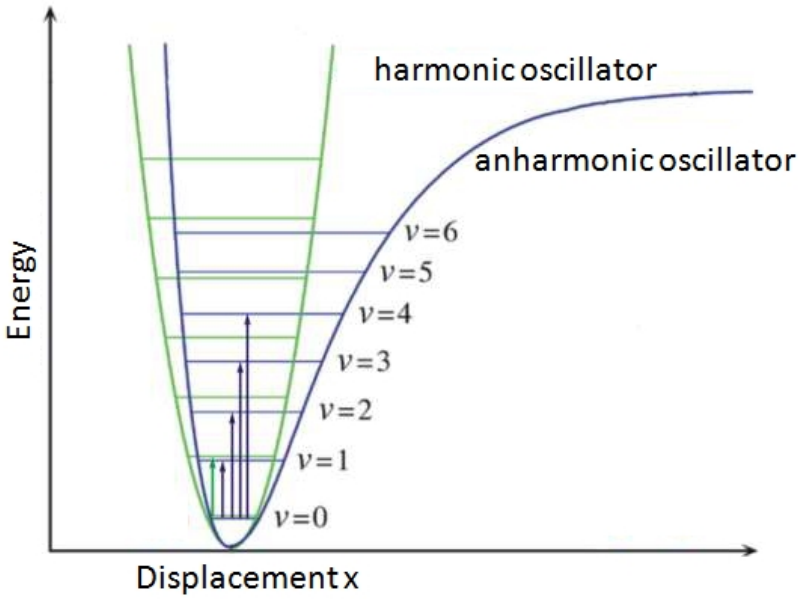

Figure 2.12: Type of vibrations in mid-IR range

(atoms).

The frequencies of vibrations in molecules are proportional to the mass of the objects and their binding energy. It is independent of the energy intensity imparted to the bond.

The modified Hooke's law (eq.5) allows to calculate the frequency/energy (in terms of wavenumbers) of absorption of radiation

$$\bar{v} = \frac{1}{2\pi c}\left(\frac{k}{\mu}\right)^{\frac{1}{2}} \tag{5}$$

where:

$\bar{v}$ is wavenumber of the absorbed peak

c is speed of light

k is force constant

μ is reduced mass of the atoms: $\mu = \frac{m_1 m_2}{m_1 + m_2}$

Due to the fact, that atoms repeal each other as they get close, bonds act as anharmonic oscillators. The differences are presented schematically in Fig. 2.12

Absorption and absorbance

According to the light absorption presented above, IR light passing the sample changes its intensity due to absorption by vibration of the molecules. Probing this absorption the intensity of primary beam - I_0 is always larger or equal the transmitted beam - I. The fraction of light that has been transmitted through the sample is called transmittance (Tr).

$$Tr = \frac{I}{I_0} \tag{6}$$

Absorbance (A), expressed as the logarithm of the reciprocal transmittance, is defined as in eq.7.

$$A = log\frac{1}{Tr} = log\frac{I_0}{I} \tag{7}$$

According to Lambert-Beer's law (eq.8) absorbance is a linear function of molecules concentration and the effective light path length in a sample. Technically, the assumption of linearity is valid only up to a certain level of concentration or sample thickness. At higher concentrations, the shadowing effect of the molecules plays an important role.

$$A = \varepsilon \cdot d \cdot x \tag{8}$$

where:
ε is molar absorbtivity
x is molar concentration
l is optical path length (thickness) of sample

The additivity of extinction (eq.9) is the basis for quantified analysis of molecule concentrations in gases (or liquids), which will be used in this work.

$$A = \sum_{i=1}^{n} A_i \tag{9}$$

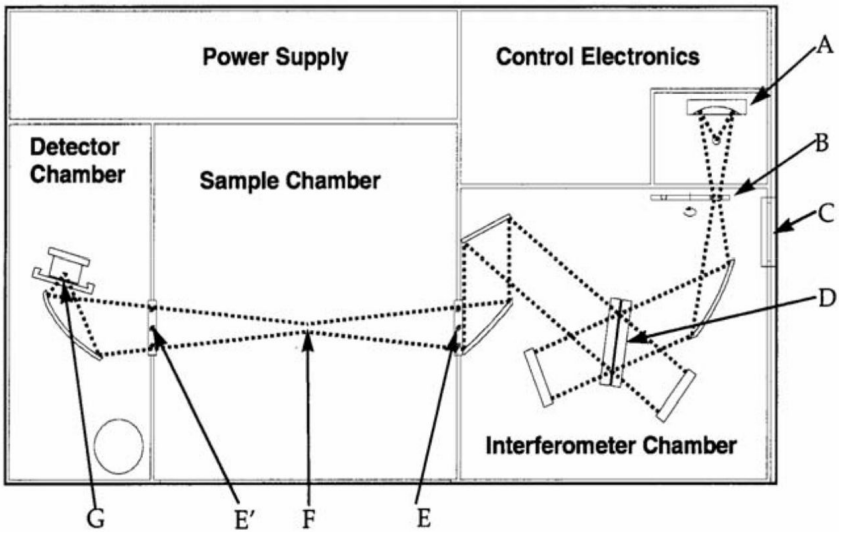

Figure 2.13: Scheme of FTIR Bruker spectrometer. A - light source, B - entrance slit, C - exit port (used for microscope), D - beamsplitter, E, E' - optional windows, F - sample holder, cell, G - detector [67]

Spectrometer construction

Simple sketch of spectrometer is shown in Fig. 2.13. The key part of our FT spectrometer is the Michelson interferometer as shown in the right bottom corner in Fig. 2.13. It consists of four mirrors and a beamsplitter (D in Fig. 2.13); one of the mirrors is movable. The beamsplitter divides the light beam into two separate beams. Each beam is reflected on only one mirror: one on the fixed mirror and the other on the movable mirror. After reflection of the beams on the mirrors, the beams interfere at the beamsplitter and the beam leaves the interferometer, interacts with the sample in the sample chamber shown in the middle of Fig. 2.13, and is eventually collected in the detector.

Constructive interference takes place when two beams are in phase with each other, and leads to an increase of the resulting beam intensity. The condition for the beams to be in phase is that their optical path will be a multiple of their wavelength as presented in eq.10. Destructive interference takes place when the paths of the beams differ by uneven multiples of the half value of the wavelength, as shown in eq.11.

$$\delta = n\lambda \tag{10}$$

$$\delta = (n + \frac{1}{2})\lambda \tag{11}$$

where:

δ is optical path difference

λ wavelength

n is an integer (-1, 0, 1, 2, 3,...)

Note that by reflecting the light beam, the movable mirror in the spectrometer is introducing an optical path difference which is twice the mirror displacement.

The relationship between light wave and the Fourier frequency of its corresponding interferogram is given by eq.12 [68]

$$F = \frac{2\nu v}{c} \tag{12}$$

where:

F is Fourier frequency of the interferogram $[Hz]$

ν is frequency of light $[Hz]$

v is moving mirror velocity $[cms^{-1}]$

c is speed of light $[cms^{-1}]$ and $c = \frac{\nu}{W}$

W is light wavenumber $[cm^{-1}]$

From above given equation it is possible to write relationship (13) between wavenumber and Fourier frequency. It proves that for each wavenumber a different frequency interferogram exists. Moreover those different waves do not have to be separated in time and space [69]

$$F = 2vW \tag{13}$$

In the real case it has to be considered, that the radiation source in FTIR spectrometer is not monochromatic and there are multiple wavelengths in the beam at the same time. For each wavenumber an interferogram exists with unique Fourier frequency. As it is shown in Fig. 2.14 for the standard interferogram of the evacuated cell, at zero path difference $\delta = 0$ total intensity of the infrared light is maximum. Its due to the fact that all waves are in-phase at this point. This peek is called centerburst and is proportional to the intensity of light striking the detector. The rapid intensity drop on both sides of the interferogram is caused by destructive interference of the light waves, when the mirror movement introduces a difference in the optical path length. These regions are called wings.

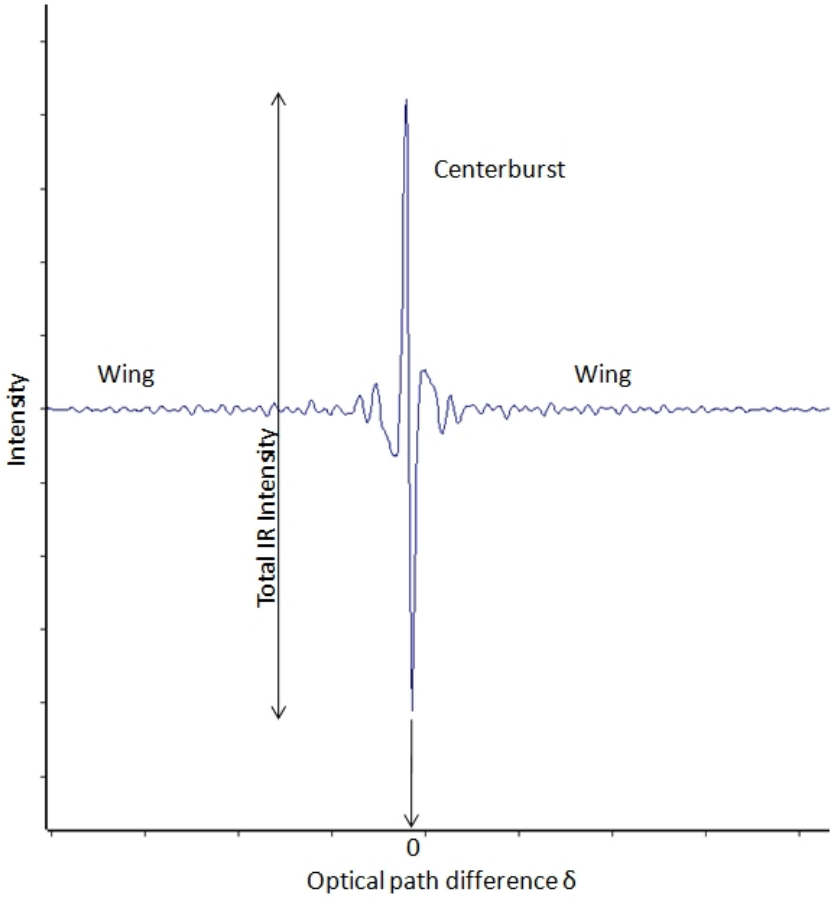

Figure 2.14: Interferogram of the evacuated cell

To get the spectrum of the measured sample, Fourier transformation (FT) has to be applied to its interferogram or more specifically to the mathematical function representing the interferogram. Results of the FT on the spectra is shown in Fig. 2.15a.

To increase the quality of the measurement, so called background spectrum without sample has to be measured. To calculate absorbance primary and transmitted beam intensity are important. The background spectrum has to be substracted from the sample spectrum as shown in Fig. 2.15

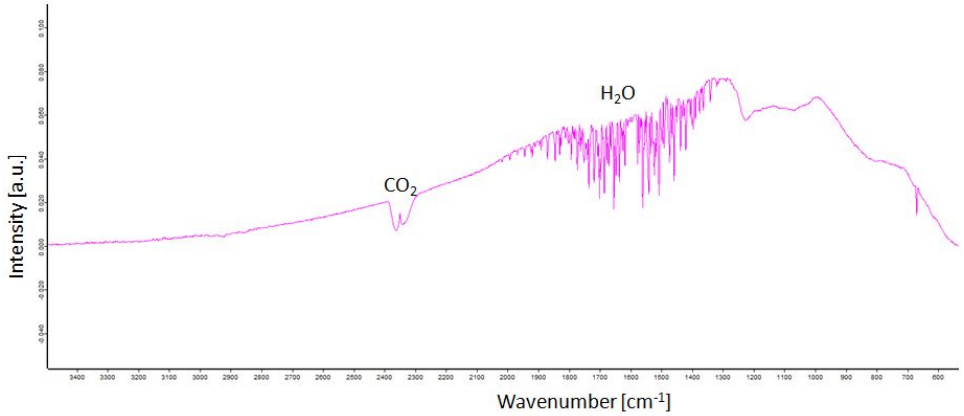

(a) background spectrum

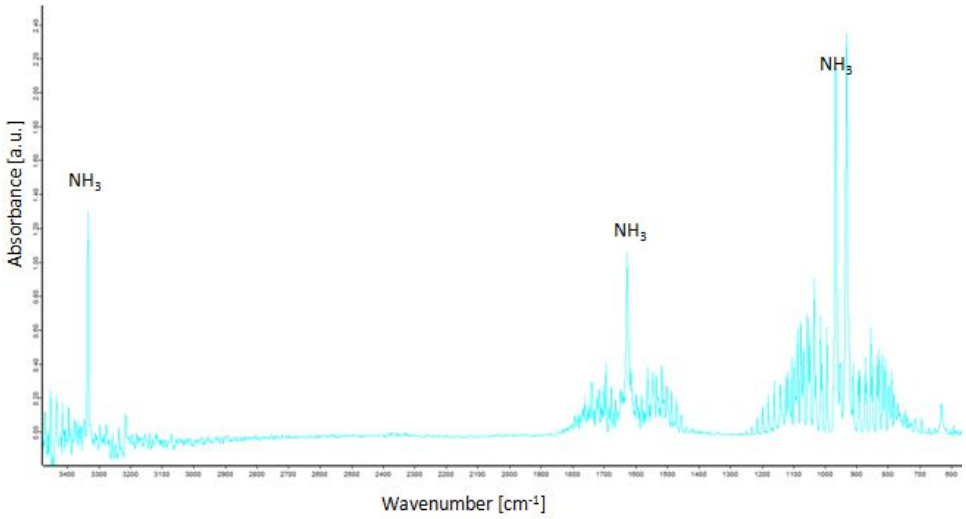

(b) example spectrum of the measured sample

Figure 2.15: Comparison between background and sample spectra

Quantitative analysis

The FTIR in this work was used to determine the gaseous components in the exhaust gas line of the reactor. Therefore, the author focus only on the determination of gaseous samples.

It is possible to quantify the FTIR measurements by measuring a few reference samples or by calculating their spectra according to the absorption coefficients given in tables for each band of the specified substances.

In principle the first method is the best one. It requires to measure few concentrations of the substances and according to the Lambert-Beer's law (eq.8) which says that absorbance is a linear function of concentration, it is easy to estimate it for any other concentration. This method is very accurate.

Nevertheless, for some substances there is a lack of reference samples and therefore this way is hard if not impossible. It is the same for highly toxic substances, which would be difficult to transfer into the measurement cell. As in case of HCN used in this work.

The calculation of the partial pressure according to given absorption coefficient (α) could be done with help of transferred Lambert-Beer's law:

$$\alpha = \frac{B}{x \cdot l} \tag{14}$$

where:

α is absorption coefficient: $[cm \cdot mol^{-1}]$

B is integral of the absorbance over the band: $[cm^{-1}]$

l is optical path length: $[cm]$

x is molar concentration: $[mol \cdot cm^{-3}]$, $x = \frac{n_i}{V}$

According to ideal gas law partial pressure P_i is given by following equation:

$$P_i = \frac{n_i}{V} RT \tag{15}$$

where:

n_i is amount of the substance: $[mol]$

V is volume: $[cm^3]$

R is universal gas constant: 6.236×10^4 $[Torr \cdot cm^3/mol \cdot K]$

T is temperature: $[K]$

Using eq.15 molar concentration could be written in following form:

$$x = \frac{P_i}{RT} \tag{16}$$

Then absorbtion coefficient α, according to above given equations, could be written in form as follows:

$$\alpha = \frac{B}{l\frac{P_i}{RT}} \tag{17}$$

finally the partial pressure P_i of the measured substance is given as:

$$P_i = \frac{BRT}{\alpha l} \tag{18}$$

According to the eq.18 concentration (C) of the substances might be calculated as it is shown in eq.19 basing on total (P_{TOT}) and partial pressure of the sample and measured component respectively:

$$C = \frac{P_i}{P_{TOT}} \times 100\% \tag{19}$$

Above presented equations for partial pressure P_i and concentration C, have been used for calculations of the gaseous components content in this work. To check the validity of the calculation, few were done using a known NH_3 content. The calculations show fair agreement with the set value. The error was in the range of approx. $\sim 15\%$ of the set value.

The values for absorption coefficients (α) for different substances were reported by Smith et al. and Pugh and Rao [70, 71].

Disadvantages and advantages of FTIR spectroscopy

Big disadvantage, that has to be taken into account while working with FTIR is that it suffers from artifact band formation, from the features that are not caused by the sample. Most irritating are CO_2 and H_2O bands, that are nearly impossible to remove from the measurement area. Nevertheless, the problem is known and if it is taken into account and the background spectra are collected under the same or at least as similar as possible conditions than the problem might be eliminated or at least reduced to a minimum as it was shown in Fig. 2.15.

Another difficulty is to interpret the spectra especially if samples with several components are measured. It is always necessary to know or at least to have some idea what the products to be determined could be. In this work, for components identification different website catalogs [72, 73] and spectral maps [74] were used.

The main advantage of FTIR spectroscopy is its suitability to measure gaseous, liquid or solid substances. Measurement of gaseous samples is of interest for this work. It is also easy to achieve signal-to-noise ratio (SNR) higher than 100 in routine measurement, that do not take more than two minutes. The high SNR is due to the throughput of FTIR, that is much higher than in standard IR measurement. Intensity depends on light that strikes the detector, it is higher for FTIR because there are no prisms, gratings or slits, that could decrease the intensity.

Other feature is that with increase in measurement time the SNR improves, because it is proportional to square root of measurement time. Measurement time could be increased by number of scans, therefore the SNR would be also proportional to square root of scan number (eq.20).

$$SNR \propto N^{\frac{1}{2}} \tag{20}$$

where:

SNR is signal to noise ratio

N is number of scans

Another advantage of FTIR over IR spectrometers is the wavenumber reproducibility, due laser light source acting as an internal wavenumber standard.

Considering problems and advantages of FTIR it is a good choice to analyze the sample especially if there are some presumptions regarding what the sample might consist of. And as shown in chapter 3.3.4 it is possible to conduct fast in-situ gas measurement using a Fourier spectrometer.

3 Experimental - pseudo halide vapour phase epitaxy

First growth experiments were conducted in an inductively heated vertical reactor (see Fig. 3.1). It is separated by a diaphragm into an upper growth zone at lower temperature and a lower source zone at higher temperature. The crucible was made of graphite. In this approach, hot ammonia in contact with carbon forms HCN gas. The HCN reacts with gallium in the crucible to form $GaCN$, which is transported by N_2 carrier gas flow to the substrate holder, where the reaction with NH_3 occurs and GaN is formed. The gallium source temperature was kept in the range of $1100 - 1300°C$, the substrate temperature at about $900 - 1200°C$. The heating up and cooling rate both were $4 - 5$ K/min in an ammonia-containing atmosphere.

The temperature control system is based on two pyrometers. One measured the temperature on the bottom of the Ga crucible, the second one on top of the sample holder. The lower temperature limitations of the pyrometers were $800°C$ and $1000°C$ respectively. Below $850°C$ the reactor was controlled by the power of the heater. Therefore, the lowest temperature, where it was possible to achieve stable parameters was approximately $900°C$.

The pseudo halide vapor phase epitaxy (PHVPE) has a similar working principle as conventional HVPE. The main difference between these two techniques is the transport agent of gallium. As described in chapter 2.2.2 classical HVPE is based on chloride transport of Ga. In case of PHVPE the transport agent is so-called pseudo halide CN^-. It means that gallium is transported in form of gallium-monocyanide $GaCN$. The rest

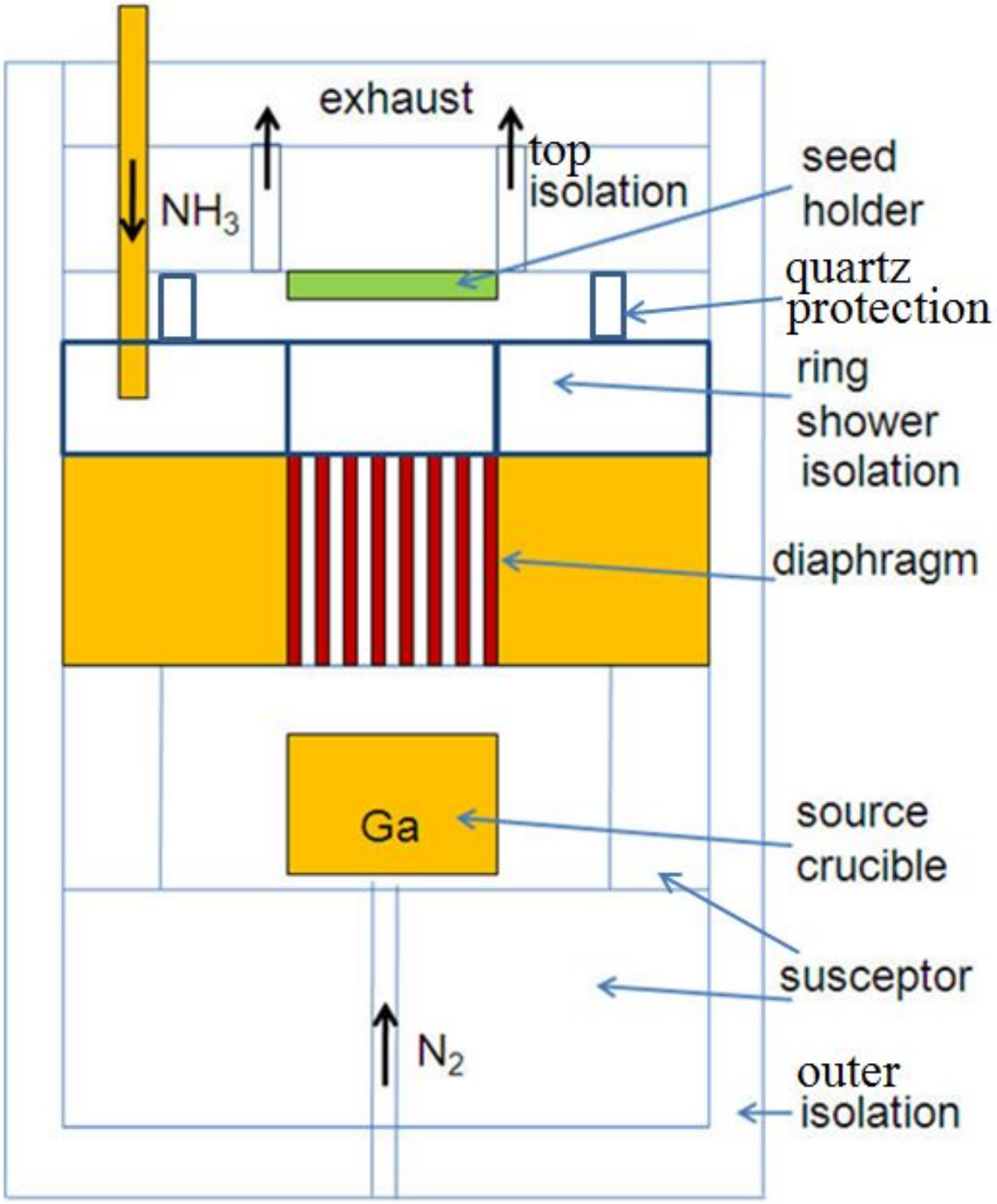

Figure 3.1: Sketch of setup used for experiment with C-limited environment

of the process is similar to classical HVPE.

Excluding aggressive HCl implies that no NH_4Cl is formed and filtering of exhaust gas is unnecessary. All byproducts could be burned in the exhaust gas burning oven in reductive atmosphere to CO_2, water and nitrogen. Additionally, lower reactivity of cyanide compound, gives the possibility for easier doping.

3.1 Graphite rich growth setup

In carbon containing setup there were two approaches to grow GaN. First one, described in this chapter is the version where parts were made of uncovered carbon parts. Experimental results of GaN growth under graphite rich conditions were presented by Rost et al. [75]. The growth experiments were carried out in a reactor as shown in Fig. 3.1.

In the original experiments gallium evaporated from a heated melt in a crucible at elevated temperatures ($1350 - 1450°C$) and was transported through the diaphragm to the substrate holder by additional N_2 carrier gas flow from the bottom where gallium reacted with ammonia, to form GaN as presented in eq.21

$$Ga(l) + NH_3(g) \rightarrow GaN(s) + \frac{3}{2}H_2(g) \tag{21}$$

3.1.1 Grown layers

First experiments showed the promising result of relatively high growth rate - up to 60 $\mu m/h$. The main issue was that the graphite parts were attacked by NH_3, as presented in Fig. 3.2a

Despite the high growth rate the layer quality of the grown crystals was bad. The grown crystal was full of 'V' shaped holes ($V - pits$) as shown in Fig. 3.2b. By using EDX, at the bottom of the $V - pits$ carbon particles were found.

To avoid the $V - pits$ formation graphite parts were covered by pyrolytical boron nitride (pBN). This change in the growth setup decreased the growth rate down to $5 - 10$ $\mu m/h$. Due to these observations, it was concluded that carbon was involved in

(a)

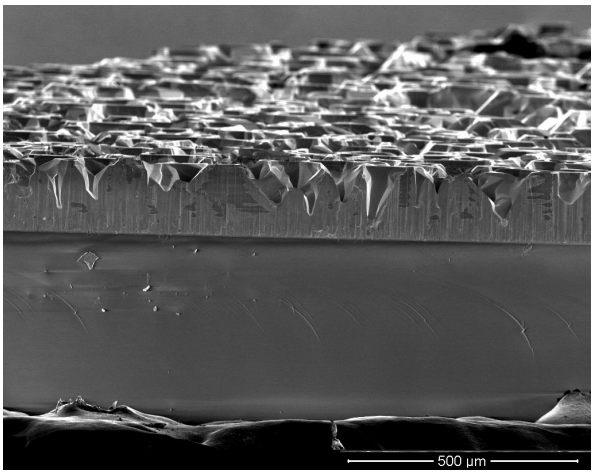

(b)

Figure 3.2: (a) Graphite part of the reactor attacked by NH_3 [76], (b) The GaN layer grown in C-rich growth setup on 2 μm MOCVD grown GaN/Al_2O_3 template [75]

Ga transport.

3.1.2 Proposed growth model

A first proposal of the growth model, based on the experimental observation and thermodynamical calculations, was given by Jacobs et al. [76]. According to the experimental results four relevant observations have been made:

1. Any graphite part close to the ammonia inlet in the deposition region undergoes a severe chemical attack (3.2a) under process conditions. It becomes porous and solid material was lost.

2. In the presence of graphite parts relatively high growth rates (up to 60 $\mu m/h$) were observed. Furthermore, the growth rate decreased with time due to the formation of a GaN crust on the liquid Ga source

3. Carbon inclusions were found in the GaN layers grown in a pure graphite environment, which were visible even under the optical light microscope. Carbon was also detected by EDX. These inclusions are probably responsible for the yellowishgrayish appearance of the layers and appearance of $V - pits$.

4. Replacement of inner graphite parts of the reactor by pBN coated ones leads to lower growth rates ($5 - 10\ \mu m/h$) in general. The pBN -coated parts turned out to be of higher chemical and mechanical stability.

On the basis of thermodynamic computations and the observed attack of graphite, it was suggested that the formation of hydrogen cyanide is the dominant process in the interaction between graphite and ammonia at high temperatures according to eq.22

$$C(s) + NH_3(g) \rightarrow HCN(g) + H_2(g) \tag{22}$$

Hydrogen cyanide shows a close similarity to hydrogen chloride, HCl. In chemistry, the cyanide anion is known as a so-called pseudo halogenide. Its chemical behavior is very similar to that of a halogen anion. Consequently, a reaction analogous to the reaction in the HVPE process, the formation of a volatile gallium(I) compound, can be expected to take place (eq.23)

$$Ga(l, g) + HCN(g) \rightarrow GaCN(g) + \frac{1}{2}H_2(g) \tag{23}$$

$Ga(CN)(g)$ as monovalent Ga compound is volatile and can easily be transported by a nitrogen carrier gas into the deposition region [77]. At the substrate holder three possibilities for GaN formation exist. The reaction 24 may run if enough ammonia is present in the growth zone

$$Ga(CN)(g) + NH_3(g) \rightarrow GaN(s) + HCN(g) + H_2(g), \tag{24}$$

The second option is the decomposition of $Ga(CN)(g)$:

$$Ga(CN)(g) \rightarrow GaN(s) + C(s) \tag{25}$$

and the third option under excess of $NH_3(g)$ in the crystallization zone is:

$$Ga(CN)(g) + NH_3(g) \rightarrow GaN(s) + C(s) + \frac{1}{2}N_2(g) + \frac{3}{2}H_2(g). \tag{26}$$

Concluding from the carbon inclusions in the crystals ($V - pits$), the reactions eq.25 and eq.26 should be significant. Nevertheless, originating from the thermal dissociation of ammonia still more chemical species and side reactions may occur, but the reactions from 24 to 26, are considered to be the main route for the formation of GaN crystals.

Thermochemical data of the most components involved in reactions 24 - 26 are available in the FactSage database. Data for $GaCN$ however, are missing. They were simulated in the 'compound mixer' mode of the FactSage software basing on the reaction between $GaCl$ and KCN to form $GaCN$. The temperature dependency of equilibrium constant (K_{eq}) shown in Fig. 3.3 was calculated according to eq.28, derived from eq.27:

$$\Delta G = \Delta H - T \times \Delta S = -RT \times lnK_{eq} \tag{27}$$

$$K_{eq} = e^{-\frac{\Delta G}{RT}} \tag{28}$$

where:

ΔG is change of Gibbs free energy

ΔH is change of enthalpy

ΔS is change of entropy

R is gas constant

T is temperature

K_{eq} for reaction $a \cdot A + b \cdot B + ... \rightleftharpoons y \cdot C + z \cdot D + ...$ can be also expressed by eq.29:

$$K_{eq} = \frac{[C]^y \cdot [D]^z \cdot ...}{[A]^a \cdot [B]^b \cdot ...} \tag{29}$$

where:

$[A]$ and $[B]$ are active mass of the reaction educts

$[C]$ and $[D]$ are active mass of the reaction products

a, b, y, z are stoichiometric coefficients of the reaction

If $K_{eq} = 1$ the educts and products are in equal concentrations. For $K_{eq} < 1$ the concentration of educts is greater than concentration of reaction products. Reactions

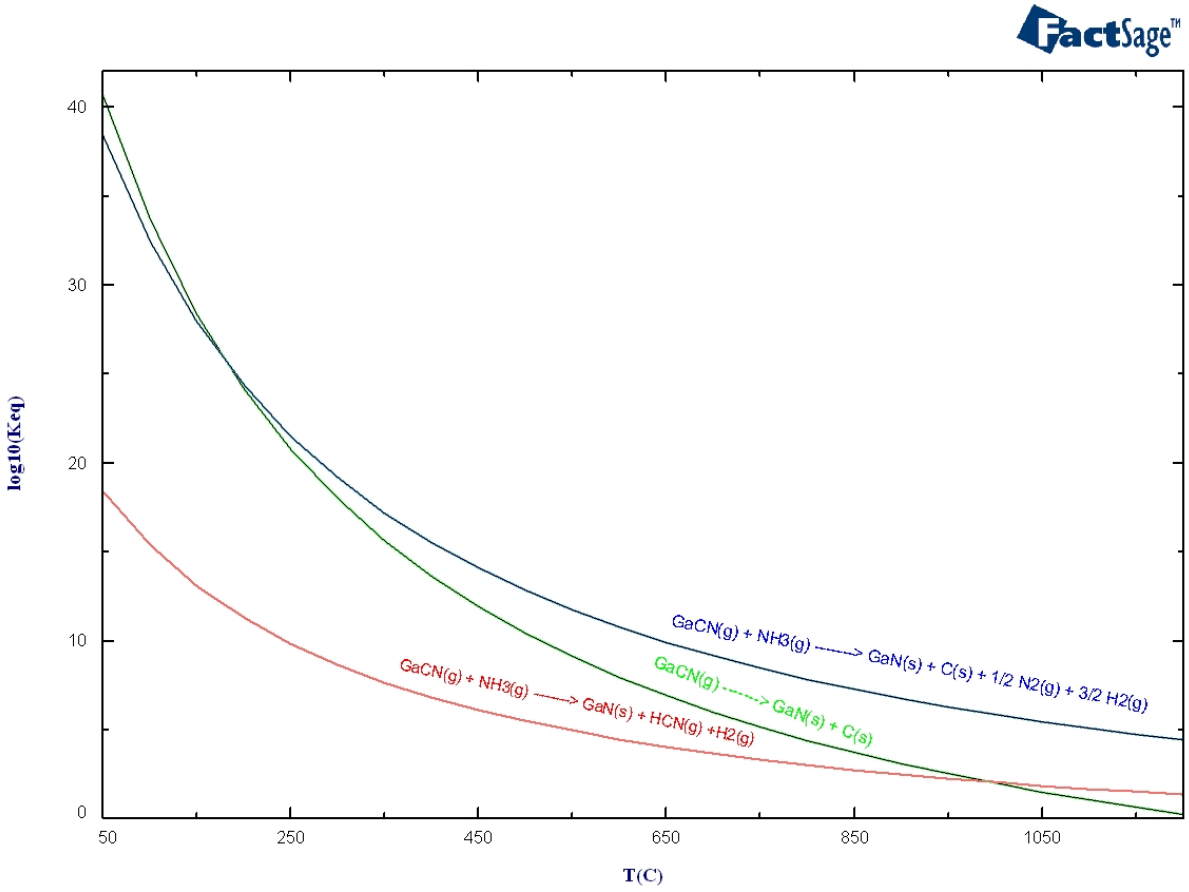

Figure 3.3: FactSage calculation of the reaction constants for eq.24 - 26 at 1 *bar*

that barely occurs have equilibrium constant in the order of the small fraction. If $K_{eq} > 1$ the concentration of reaction products is greater than concentration of educts. Almost completed reactions have equilibrium constant $K_{eq} \sim 10^5$ [78, 79].

At process temperature $\sim 1050°C$ values of $lgK_{eq} = 5.39; 1.79; 1.45;$ were derived for reactions 24 - 26 respectively (see Fig. 3.3). Therefore, all reaction paths are probable, however, from the calculation point of view reaction 26 is most likely to be dominant. The author is aware that the thermodynamic calculations are of limited value and provide a rough guidance only, due to kinetic barriers of the process.

3.1.3 Ex-situ characterization of exhaust gases

As a part of this work a measurement setup to confirm the theoretical predictions explained in the previous chapter was designed. It is based on a FTIR spectrometer. The aim of the measurements, was to repeat previously described experiments, where the growth rate of GaN was on the level of 60 $\mu m/h$, and measuring the gas composition by FTIR method for gas samples collected from the waste gas line at different process temperatures from $950°C$ up to $1250°C$, measured by pyrometer on top of the seed holder.

The second important aim of the measurements was to gain experimental data to support the construction of a new, graphite free reactor. It allowed to investigate reaction products and byproducts, and therefore to explain how growth was achieved in terms of chemical reactions inside the growth cell. Finally, these measurements should confirm the theory of pseudo halide transport or simply disprove it.

Setup and sampling procedure

The Fig. 3.4a shows the gas cell with $ZnSe$ windows, valves and gas inlet/outlet mounted on the stage. It fits into the measurement chamber of the FTIR spectrometer, as it is shown in Fig. 3.4b. Fig. 3.4c shows the connection between gas cell and the reactor exhaust gas line.

To explain in detail the sampling procedure, Fig. 3.5 shows the schematic connection

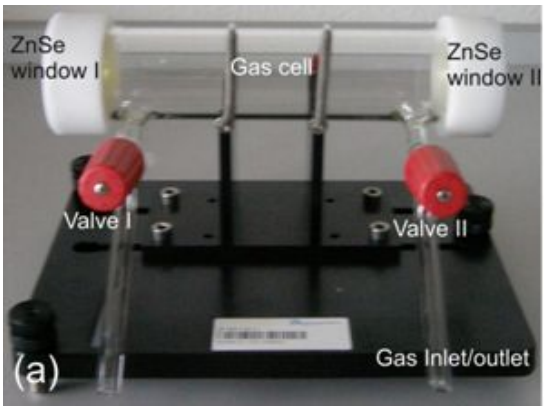

(a) gas cell used for exhaust gas collection and measurement

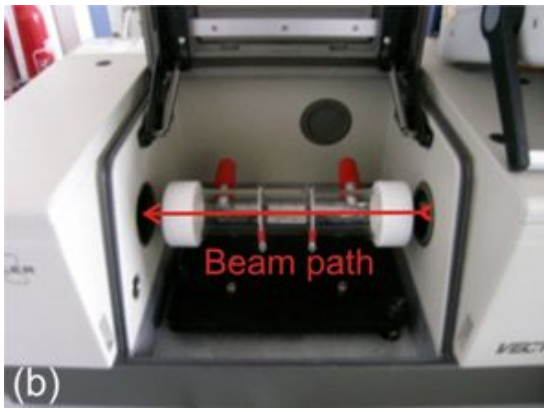

(b) chamber of the spectrometer with gas cell inside with indicated beam path

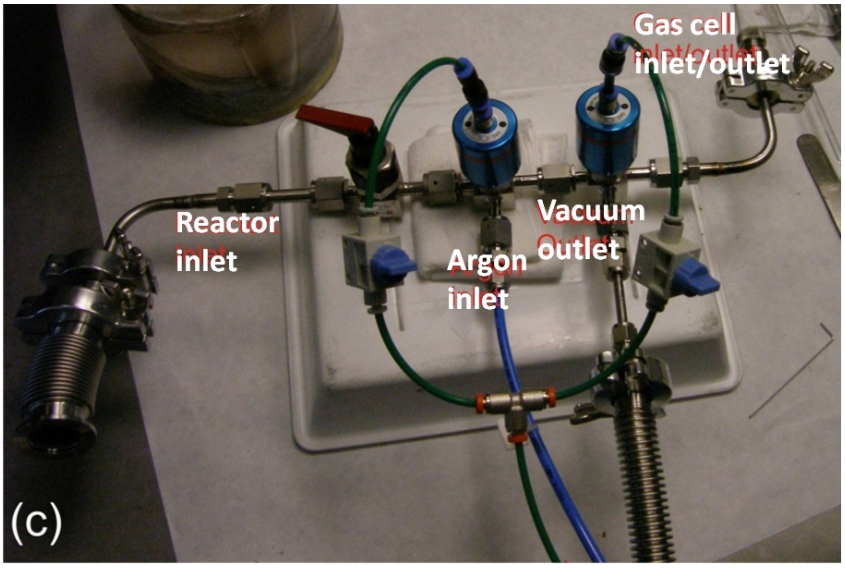

(c) Valve system for gas cell, Ar/vacuum purging system and exhaust gases filling

Figure 3.4: Elements of the ex-situ measurement setup

between the lines. The most important parts such as: vacuum outlet, argon inlet, reactor inlet (exhaust-gas) and gas cell inlet/outlet are shown.

The sampling procedure was as follows:

1. Purging the line ($V1$, $V4$ stay closed - green only) - 5 times

   Pumping down ($V2$ opened, $V3$ closed) 5 sec

Filling with argon ($V3$ opened, $V2$ closed) 5 sec

2. Purging the gas cell ($V4$ stay closed, $V1$ stay opened green and pink) 10 times

   Pumping down ($V2$ opened, $V3$ closed) 7 sec

   Filling with argon ($V3$ opened, $V2$ closed) 7 sec

3. Final pumping ($V4$ closed; $V1$, $V2$ opened) 20 sec

4. Collecting exhaust sample ($V1$, $V4$ opened; $V2$, $V3$ closed) 20 sec

5. Cleaning the line ($V4$, $V1$ closed green only) 5 times

   Pumping down ($V2$ opened, $V3$ closed) 5 sec

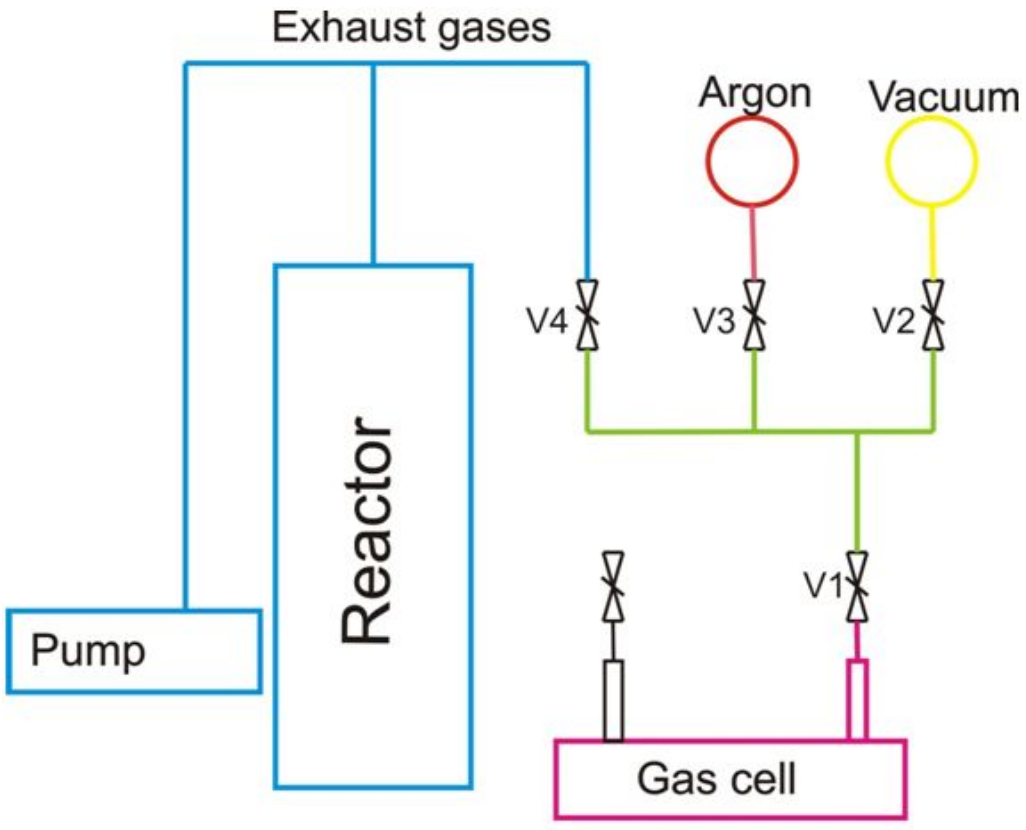

Figure 3.5: Schematic draft of the connection between reactor and gas cell. Each color corresponds to the lines which are normally connected. The connection between different colors might be managed by switching the valves.

Filling with argon ($V3$ opened, $V2$ closed) 5 sec

Measurement results

In Fig. 3.6 the most intensive band of NH_3 at wavenumber range from 1200 cm^{-1} up to 780 cm^{-1} and the most intensive HCN band from 800 cm^{-1} up to 625 cm^{-1} are compared at 900°C - red curve and 1250°C - black curve. The intensity and width of the lines depends strongly on the process temperature. Moreover, the mutual relation of the peaks changes significantly. At 900°C NH_3 dominates, and only a small band of HCN is present. At 1250°C the HCN band is dominant and achieves the intensity level of NH_3 band at 900°C.

The calculations of the composition at different temperatures for both - HCN and NH_3 are presented in Fig. 3.7. At 900°C the measured part of HCN is on the level of 0.2%. This value results from partly overlap of NH_3 and HCN bands at 900°C. The correctly measured value appears at 1000°C and is approx. $\sim$ 0.3%. Nevertheless, the increasing trend can be easily seen. The constant concentration for NH_3 in the temperature range from 1000°C up to 1150°C is due to an overlap with a part of the strongly increased HCN band.

The FTIR measurement showed also a very weak signal of methane. Due to the overlapping with NH_3 and H_2O vapor bands and very small peak height of approx. 0.04 $a.u.$ (in comparison HCN peak height was approx. $\sim$ 3.1 $a.u$ and NH_3 approx. $\sim$ 2.2 $a.u.$ at the same temperature) it was not possible to calculate it properly. Nevertheless, knowing that the CH_4 absorption coefficient α (see eq. 17) is 15% higher than that of NH_3 bands, it was possible to estimate its concentration to be approx. $\sim$ 99% lower than the concentration of NH_3. It means that it was approx. $\sim$ 0.02%. Therefore it might be neglected for the consideration of the growth model. Although, appearance of methane at such a low volume would not participate significantly in the growth of GaN, it might be helpful to explain increased NH_3 decomposition. At least two molecules of NH_3 in the simplest model would be required to form one CH_4 molecule, according to eq.30:

$$2NH_3(g) + C(s) \rightarrow CH_4(g) + N_2(g) + H_2(g) \tag{30}$$

The other possibility would be that part of HCN is synthesized due to the reaction of CH_4 and NH_3. This reaction will be discussed in more detail in chapter 3.3.3.

3.1.4 Discussion

The measurements presented above confirm the prediction about the growth model made by Jacobs et al. [76]. They prove that HCN is the main component responsible for

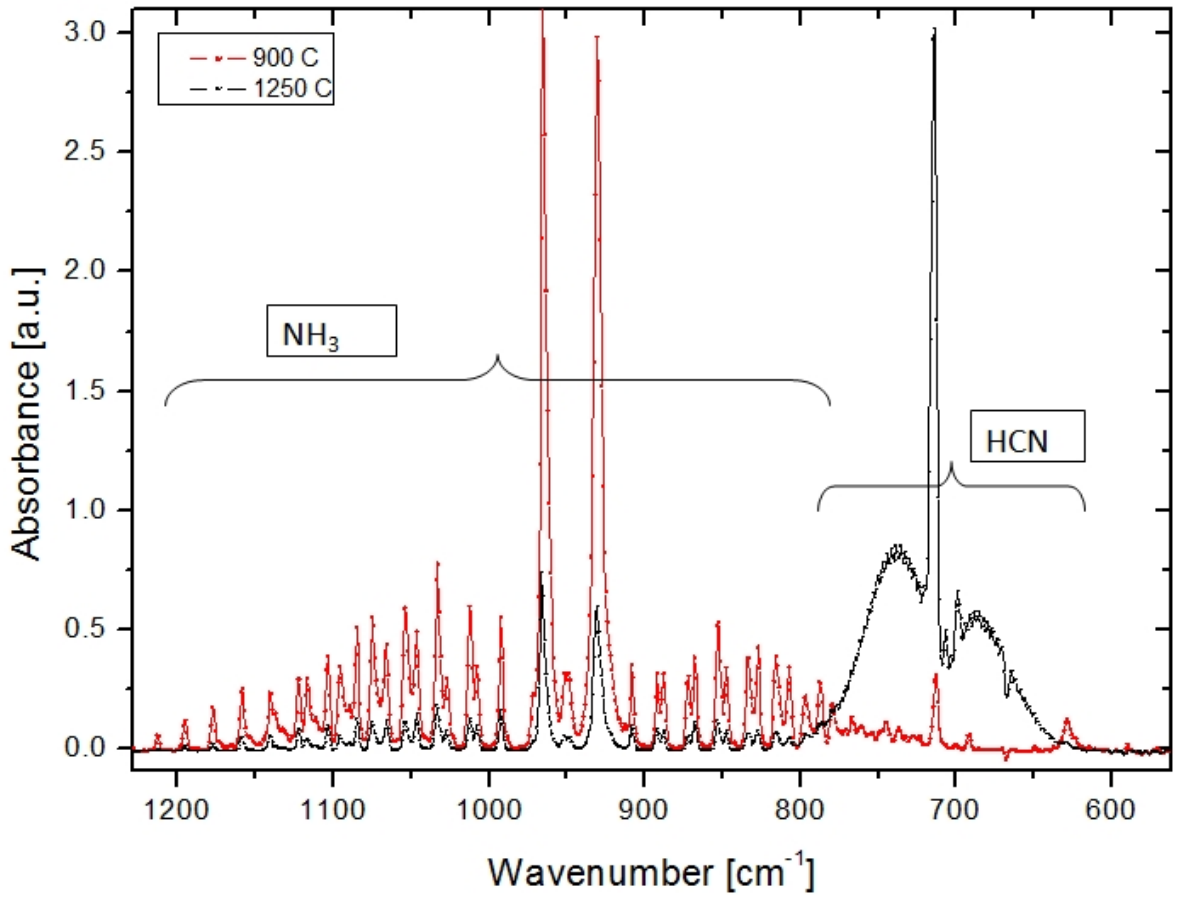

Figure 3.6: Comparison between strongest NH_3 (left) and HCN (right) peaks at 900°C (red) and 1250°C (black)

the chemical transport of Ga, while the vapor pressure of Ga at process temperature i.e. below $1150°C$ is lower than 7×10^{-2} $mbar$ which makes a physical transport not effective. One detail that is in contradiction to the thermodynamic calculations is the volume of measured CH_4, which is much lower than expected (see Fig. 3.8). This behavior remains unexplained. However, there is a possibility that significant part of CH_4 is used to produce HCN.

Nevertheless, these measurements are in good agreement with the calculated values presented in Fig. 3.8, showing that ammonia is almost completely decomposed into N_2 and H_2 at temperatures $> 1000K$. Moreover, at temperatures $> 1250K$ HCN is already

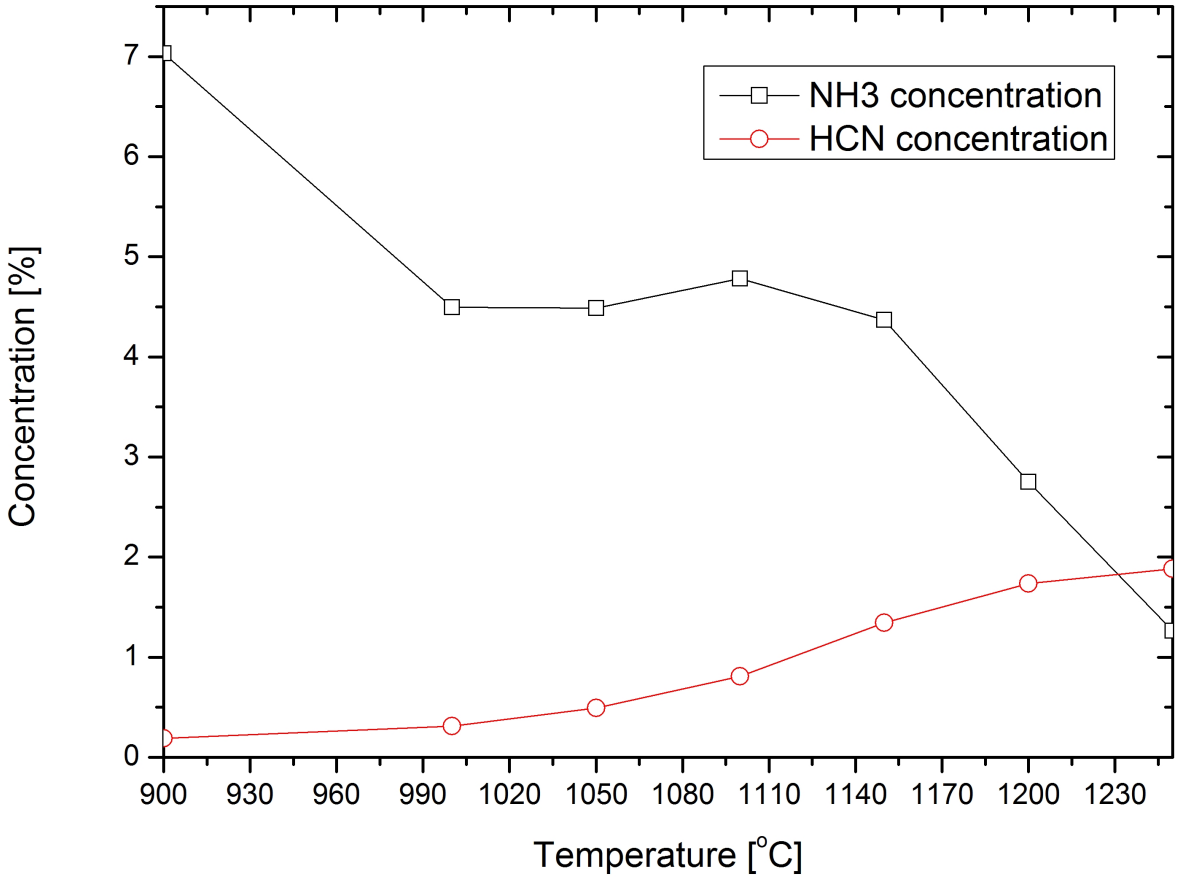

Figure 3.7: Calculated concentration of HCN (red) and NH_3 (black) versus temperature

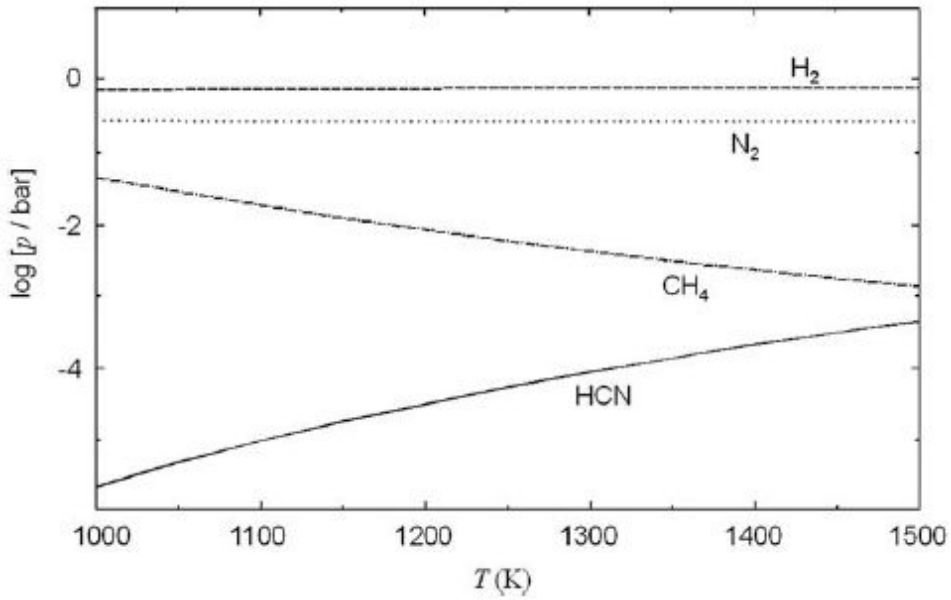

Figure 3.8: Concentration of vapor phase species formed by the reaction between graphite and ammonia as a function of temperature (calculated with 'FactSage' software) [76]

most abundant with the exeption of methane with concentrations $> 4 \times 10^{-4}$. The concentration of HCN increases with increasing temperature [76], what is in agreement with FTIR measurements of the growth experiments.

The second important information comes from undecomposed NH_3 in the reactor exhaust line. It was measured that at $900°C$ only approx. $\sim 7\%$ of NH_3 was undecomposed. At $1250°C$ this amount is below 1.5%. It is in contradiction with the mass spectroscopy measurement made by Ban [80], who showed that only 4% of NH_3 is decomposed. Also Liu and Stevenson [81] investigated the decomposition of ammonia in different environments experimentally. They found that $98 - 94\%$ of the incoming ammonia still left a pure quartz tube after passing the gas at temperatures between 900 and $1150°C$ through this tube, while only $95 - 90\%$ were still found at the outlet after passing a new graphite liner.

The contradiction between the measurement results and published data lead to the conclusion, that the main source of HCN is not the reaction with dense graphite, but with the thermal insulation felt, made of graphite fibers. It was observed, that thermal

insulation parts were strongly etched by hot NH_3. The outer cylindrical felt had an underetched ring on the level of ammonia supply line outlet. This part of the cylinder and also the isolation disc between the diaphragm and the substrate holder were most exposed to NH_3. The density of the isolation material, made of graphite fiber is much lower than the graphite and the surface is much higher. There are also data (discussed in chapter 3.3) indicating, that HCN formation depends mostly on the catalyst surface, which in our case will be the carbon.

3.2 Graphite limited growth setup

In the first practice a physical vapor transport of Ga was assumed and the setup that should avoid the reaction between carbon and ammonia was developed. The growth setup used for experiments described in this chapter is the same as in Fig. 3.1. Most of the parts were coated with pBN. Only the outer insulation cylinder was used without protective layer. Due to its oversize, it was impossible to deposit a continuous layer of pBN on the inner side wall of the cylinder. Therefore, in other procedures the material was exchanged.

3.2.1 Reactor materials

The material used for insulation in our reactor must fulfill four requirements. It must be chemically stable against hot NH_3 and H_2 at process temperatures exceeding $1000°C$. This limits the choice of materials to only a few. The second parameter, as the material is supposed to be thermal insulating, is its thermal conductivity which should be as low as possible. It has to be also transparent for the radio frequencies (RF) as the inner susceptor is heated by RF power. Last but not least an important property is its availability in reasonable time and cost and in desired shape.

The chosen material was Altraform KVS184/400 [82] containing 22% SiO_2 and 78% Al_2O_3. It has a density of 400 $kg \cdot m^{-3}$ and thermal conductivity of $\sim 0.3\ W \cdot m^{-1}K^{-1}$ at $1200°C$. Beside its perfect parameters and chemical resistance it has one huge drawback - porosity. As it was described by Zwierz [83] while using Altraform only Ga-oxide could be grown due to the high oxygen content in the pores of the Altraform. Even day-long pumping did not solve the problem of remaining oxygen, especially because the reactor has to be opened after each experiment. Due to the absence of a glove box the isolation was exposed to air and water vapor. The same problem was observed while using porous ZrO_2 as isolation disc between the diaphragm and the seed holder.

Therefore, graphite felt was used as isolation and the path between the outlet of NH_3 and the outer isolation was blocked with a quartz ring. In this way the reaction was

significantly limited.

In Fig. 3.9 photographs of reactor compounds covered with pBN are presented. In case of the parts made of dense graphite it was possible to polish the deposited pBN film. However, in case of the isolation any attempt of polishing caused cracks in the protection layer, due to the porosity and softness of material used for isolation. Therefore, the isolation parts had to be used as deposited. Such a layer without polishing and re-deposition of pBN was not homogeneous. There were still micro - channels, through which NH_3 could access the carbon and react to HCN. This was proved by weighing

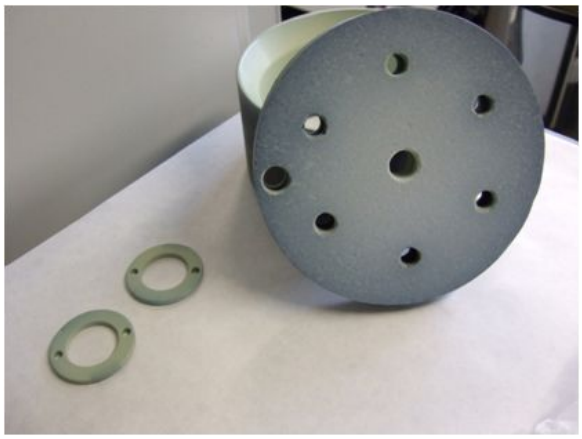

(a) graphite susceptor, diaphragm rings, top carbon felt isolation disc

(b) graphite substrate holder

(c) Ring shower isolation made of carbon felt with visible gaps in the cover layer on the inner side

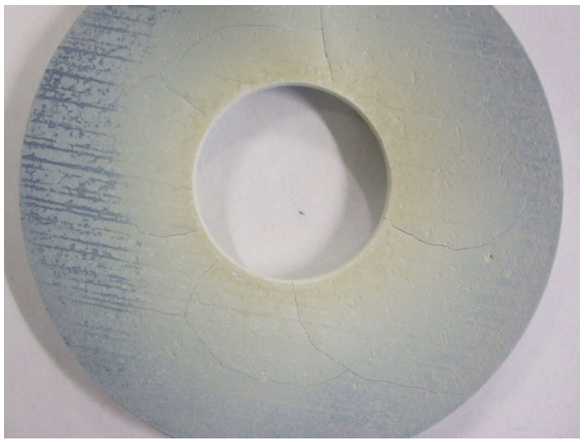

(d) Ring shower isolation made of carbon felt with cracks in the cover layer after the experiment

Figure 3.9: Elements of the experimental setup covered with pBN

the mass of the parts before and after each experiment. It was found that only isolation parts reduced their mass. Most significant mass reduction was observed on the ring shower isolation. There were two ways for NH_3 to get access to the carbon underneath. The most problematic one is presented in Fig. 3.9c. Due to high porosity the layer of pBN was not closed and there was a significant gap at the 'step' of the inner isolation side wall. Additionally it is easy to crack a layer on a soft material for isolation. Typical cracks are shown in Fig. 3.9d. They appear even after first use of the element.

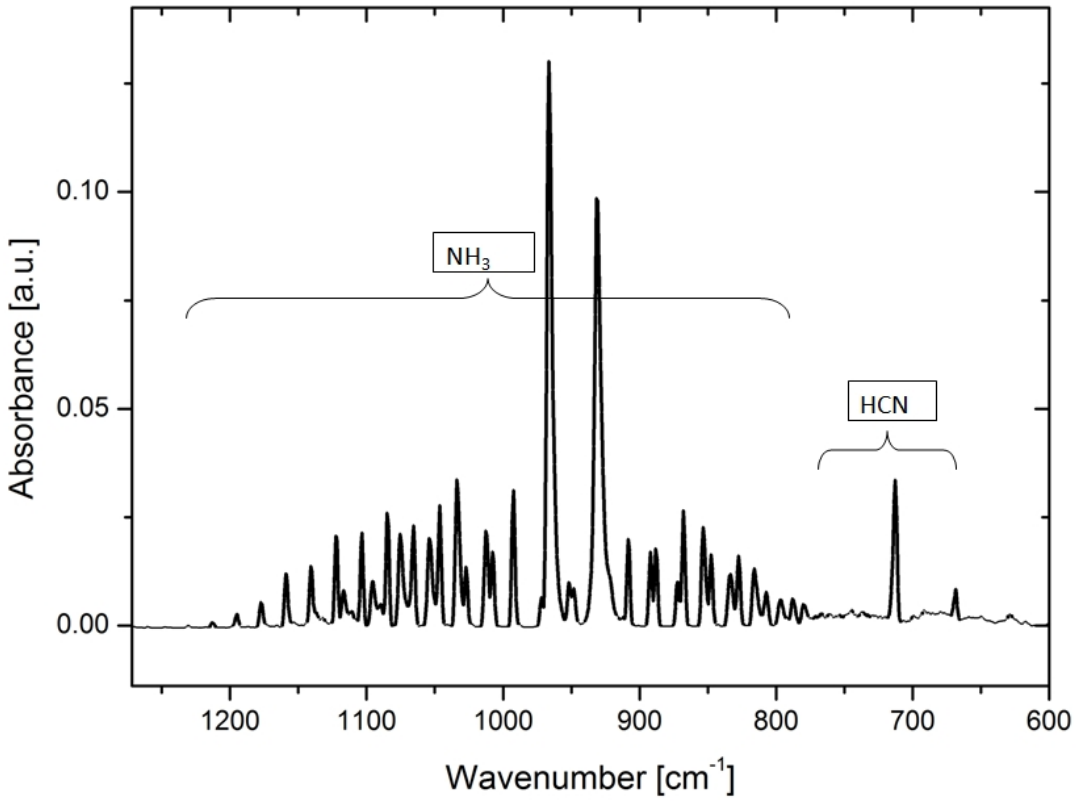

Figure 3.10: FTIR measurement of the exhaust gas at the process temperature $1200°C$ in C-limited reactor - bands of HCN and NH_3

3.2.2 Pre-experiments

For a standard experiment with NH_3 flow of 200 $sccm$ ring shower isolation mass could be reduced by up to 6% - that is approx. 1 - 3 g, depending on the quality of deposited pBN (which also varied between different deposition runs). Such an amount was also enough for chemical transport of Ga. The existence of HCN in the above mentioned setup is proved by FTIR measurement, although the intensity of the cyanide band in comparison to ammonia is low. The spectra for the sample collected at the process temperature of 1200°C and NH_3 flow of 600 $sccm$ are presented in Fig. 3.10.

Regarding the first FTIR measurements (as in this case) the sampling method was not reproducible, therefore it is possible only to confirm or deny the existence of gaseous species in the process. Nevertheless, an estimation shows, that the content of HCN is approx. $\sim 0.5\%$ in the exhaust gas line. This is four times less than in case of experiments in carbon rich environment and explains the dramatic decrease of the growth rate down to approx. $2-5$ $\mu m/h$, in comparison with data reported by Rost et al. [75] (60 $\mu m/h$) using uncovered carbon parts.

In comparison to the experiments under C- rich environment the layer quality improved. There were less $V-pits$ and they were also not as deep for the sample of similar

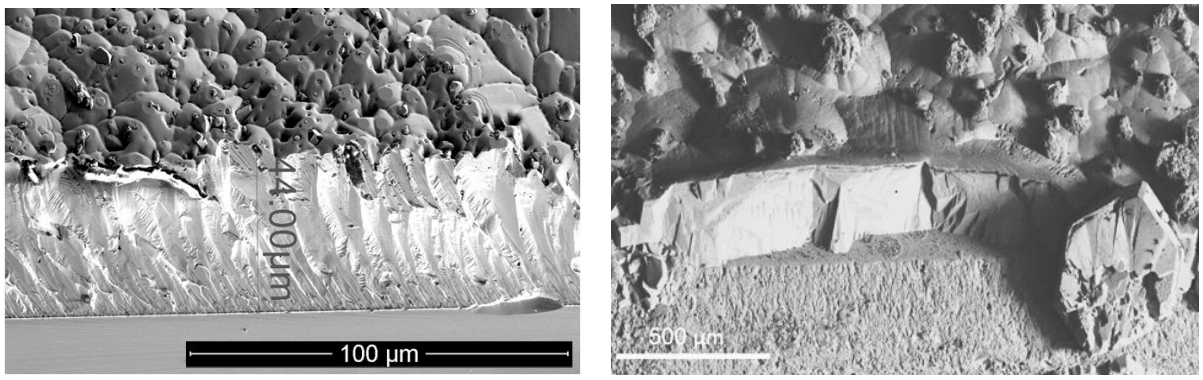

(a) Sample with grown ~ 44 μm of GaN during 24 hours process

(b) Sample with grown ~ 150 μm of GaN during 72 hours process

Figure 3.11: Layer of GaN grown in C-limited environment with different growth time both grown on the GaN/Al_2O_3 templates.

thickness (approx. $\sim 300\ \mu m$). Two layers grown in the reactor with pBN covered parts are presented in Fig. 3.11. The growth time was 24 h (Fig. 3.11a) and 72 h (Fig. 3.11b), at similar growth rate of about $\sim 2\ \mu m/h$.

An important issue and the bottle neck of this growth setup was the lack of reproducibility. Changes of growth parameters between the processes were caused by different access of NH_3 to carbon. It was due to differences between the quality of pBN covered parts from different deposition runs. Some of them have the gaps as presented in Fig. 3.9c already before first experiment and in some of them the gap did not appear at all. The cracking of the film was also unpredictable. An important factor already mentioned was the reduction of carbon volume after each experiment. For some of the parts the layer did not crack before the graphite felt was removed almost completely from underneath of pBN. In this case, only the hollow body isolation lasts. Unfortunately it was extremely mechanically unstable and therefore got destroyed after few experiments.

Therefore, with decreasing mass of the ring shower isolation the growth rate reduces as well. Only some poly-crystalline GaN powder or small - not coalesced islands were grown on the substrate as shown in Fig. 3.12

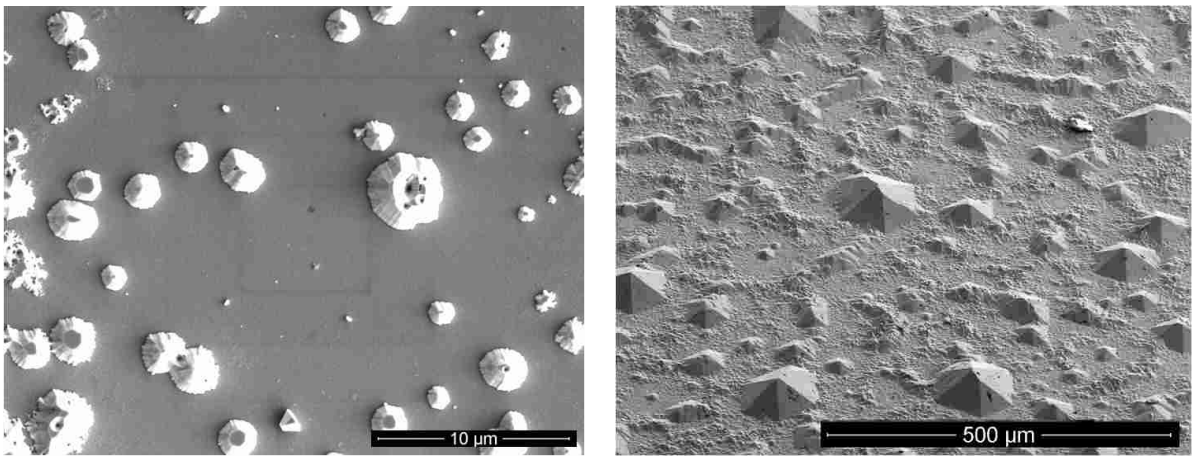

(a) Sample after 4 h process, grown on AlN/Al_2O_3 template

(b) Sample after 4 h process, grown on GaN/Al_2O_3 template

Figure 3.12: Samples grown during 4 h process on two different templates with low transport of gallium

3.2.3 Different substrates

The commonly used substrate for growth of thick GaN layers is sapphire (Al_2O_3) due to its relatively low price, thermal stability and hexagonal symmetry. However, approx. 16% [84] mismatch in lattice parameters and 19% [85] differences in thermal expansion coefficients between sapphire and GaN lead to high in-plane strain, strong bowing, and cracking of the grown layer even after separation from its substrate [86, 87].

Another better lattice-matched substrate is silicon carbide (SiC). It is advantageous in device applications, where good thermal or electrical conductivity is required, but it is more expensive. For power electronic and optoelectronic devices, including blue lasers, free-standing GaN substrates are needed. In this case the thick GaN layers that were originally grown on sacrificial Al_2O_3 or SiC wafers have to be separated by using the laser-lift off method [88] nano-lithography [89], as well as reactive ion etching for growth on SiC. All these approaches are expensive and time-consuming.

3.2.4 Growth on $\beta - Ga_2O_3$ substrate[1]

As an alternative $\beta - Ga_2O_3$ substrates were used for GaN crystal growth. Such substrates have attractive properties, e.g. high n-type conductivity and transparency from the deep ultraviolet to the infrared spectral range (optical band gap of about 4.9 eV) [91]. $\beta - Ga_2O_3$ has monoclinic ($C2/m$) crystal structure with lattice parameters $a = 12.214\mathring{A}$, $b = 3.0371\mathring{A}$, $c = 5.7981\mathring{A}$ and $\beta = 103.83°$. Therefore, growth of wurtzite GaN on it is in principle a great challenge. Nevertheless, few authors have already published results on growth of GaN on $\beta - Ga_2O_3$ bulk crystals or interlayers. Recently, Itho et al. [92] reported on the possibility to prepare III-nitride based vertical UV LEDs on $\beta - Ga_2O_3$ substrates. Ohira et al. [93] presented growth of GaN layers by radio frequency molecular beam epitaxy (RFMBE) on $\beta - Ga_2O_3$ grown by optical floating zone (FZ) method, Tsai et al. [94] showed GaN layers grown by MOCVD on sapphire using a $\beta - Ga_2O_3$ interlayer and Shimamura et al. [95] have grown GaN by HVPE on FZ $\beta - Ga_2O_3$. Additionally,

[1] Data presented in this chapter were used for publication [90]. Reproduction with permission from The Royal Society of Chemistry.

(a) $\beta - Ga_2O_3$ crystals grown by the Czochralski method

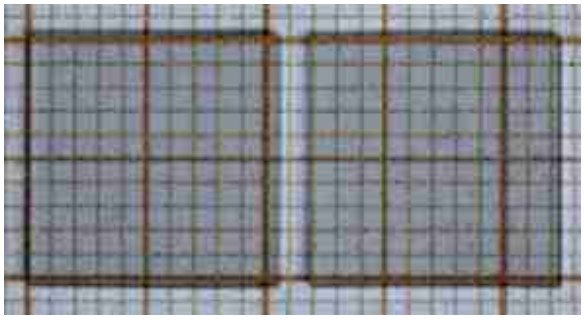

(b) (100) substrates from the Czochralski grown -$\beta - Ga_2O_3$ crystals for epitaxy purposes

Figure 3.13: $\beta - Ga_2O_3$ crystals used in this work [91]

a theoretical study of structural properties of the $GaN/\beta - Ga_2O_3$ heterojunction was reported by Liu et al. [96].

Below the $PHVPE$ growth of thick hexagonal GaN is reported. The layers were grown directly on Czochralski (Cz) grown single crystalline $\beta - Ga_2O_3$ (100) as presented in Fig. 3.24 [91]. The $5 \times 10\ mm^2$ substrates for growth experiments were obtained from crystals sliced, and epi-ready polished (Fig. 3.13b). A detailed description of the growth of $\beta - Ga_2O_3$ and its properties can be found elsewhere [91]. It is shown that bulk GaN self-separates from the substrate at room temperature, initiated by the easy cleavage of $\beta - Ga_2O_3$ along its a-plane. The GaN film properties and the properties of the $GaN/\beta - Ga_2O_3$ interface were studied. Additionally, a comparison with the properties of GaN grown on c-plane epi-ready polished sapphire is presented.

3.2.5 Results and discussion

Fig. 3.14 (a) and (b) show SEM micrographs of the surface morphology of an as-grown GaN on $\beta - Ga_2O_3$. The SEM inspection reveals hexagonal hillocks on the GaN layer, which come from the inversion domains. Fig. 3.14 (b) shows a cracked part of GaN layer that was self-separated and lifted from the substrate during the cooling down process.

In order to compare the structural properties of GaN grown on sapphire (sample S1) with those of GaN on $\beta - Ga_2O_3$ (sample S2), the GaN deposition was simul-

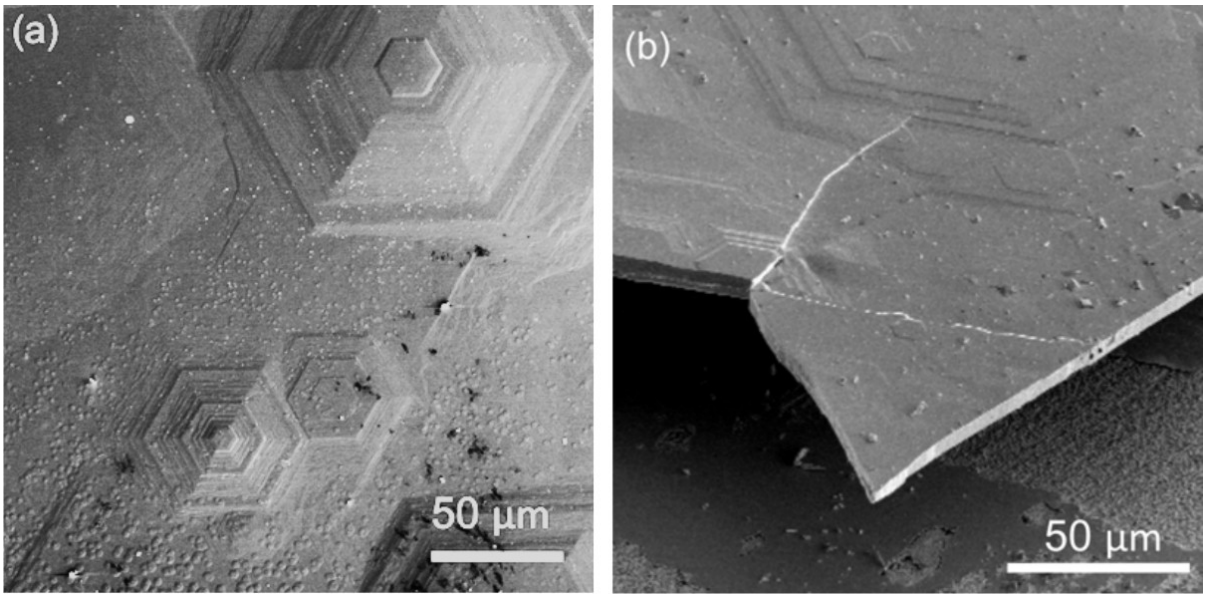

Figure 3.14: SEM image of 6 μm thick GaN grown for 4 h on $\beta - Ga_2O_3$; (a) continuous layer of GaN with hillock formation, (b) self-separated GaN layer, underneath is the $\beta - Ga_2O_3$ substrate

taneously carried out on both substrates. Both substrates were nitridized under the same conditions. Sapphire required higher temperature of nitridization than $\beta - Ga_2O_3$. Nevertheless, the purpose of this experiment was to prevent any changes in the growth conditions between both samples as they were not completely reproducible as described before (3.2.2). This procedure ensures a reasonable basis for comparison. The substrates were placed on the holder next to each other in order to exclude any differences in the relevant process parameters. Nevertheless, distinct differences in the surface morphology and in structural perfection of the grown layers were observed as shown in Fig. 3.15 (a) and (b). The layer grown on the $\beta - Ga_2O_3$ substrate exhibited a smooth surface, while its counterpart on sapphire was characterized by a rough and irregularly shaped surface. Atomic force microscopy (AFM) on the 10×10 μm^2 GaN surface showed that for S1 the surface roughness RMS amounts to $\sigma_{S1} = 75$ nm, while for S2 it is reduced to $\sigma_{S1} = 5$ nm.

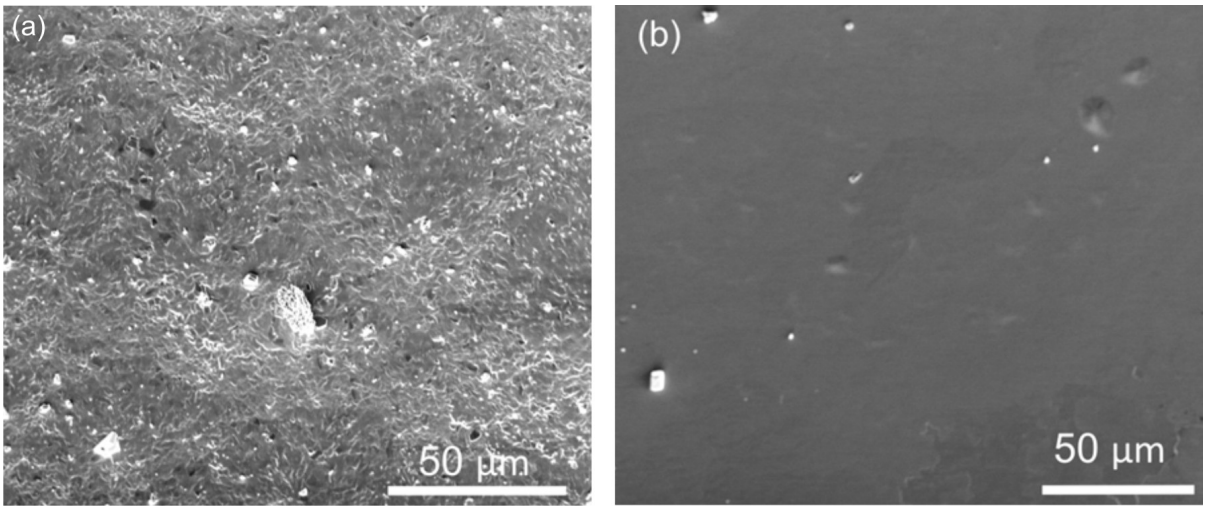

Figure 3.15: SEM image of GaN layer grown on (a) Al_2O_3 ($S1$) and (b) on $\beta - Ga_2O_3$ ($S2$) substrate

The high resolution x-ray diffraction (HR-XRD) rocking curves around the 0002 Bragg reflection of GaN reported in Fig. 3.16 confirmed the considerable difference of the crystalline quality between the two samples. The x-axis shift between the curves in Fig. 3.16 is due to different sample orientation on the holder. The full width at half maximum (FWHM) was about $\Delta\omega_{0002} = 2580$ $arcsec$ for GaN grown on sapphire, while for the layer grown on $\beta - Ga_2O_3$, the FWHM amounts to about $\Delta\omega_{0002} = 1020$ $arcsec$. A rough estimation of the threading dislocation density ρ, based on the eq.31 [97] was carried out:

$$\rho = \frac{\Delta\omega^2_{(0002)}}{4.35 b_c^2} \tag{31}$$

where:

ρ is dislocation density

$\Delta\omega_{0002}$ is measured FWHM

b_c is Burgers vector component along the c-axis (estimated to be equal to the c lattice parameter of GaN)

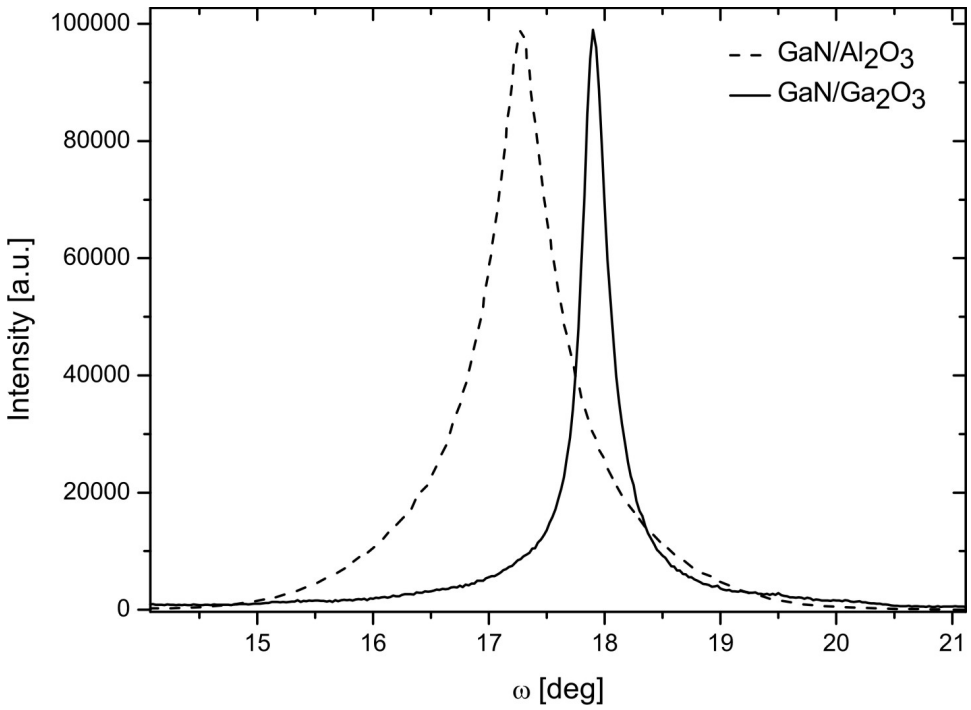

Figure 3.16: FWHM of HR-XRD rocking curves around the (0002) Bragg reflection for GaN grown on Al_2O_3 (2580 arcsec), and on $\beta - Ga_2O_3$ (1020 arcsec)

Using the experimentally determined FWHM, the dislocation density was estimated to be $1.3 \times 10^{10}\ cm^{-2}$ and $2.1 \times 10^{9}\ cm^{-2}$ in samples S1 and S2, respectively. This proves that, when using the same (non-optimized) deposition parameters, the use of $\beta - Ga_2O_3$ is advantageous in terms of dislocation density. In contrast to the publication of Tsai et al. [94], where a buffer layer of Ga_2O_3 was used and nearly no difference in FWHM between samples with and without gallium-oxide interlayer was observed, we obtained a significant decrease of the FWHM when using $\beta - Ga_2O_3$ substrates instead of sapphire. Moreover, Tsai et al. described also the influence of hydrogen to Ga_2O_3 interlayer. The authors claim that using H_2 as main gas flow makes the interlayer of Ga_2O_3 'bumpy', due to its decomposition promoted by H_2. On the other hand, Itho et al. [92] have grown GaN on $\beta - Ga_2O_3$ bulk substrates by MOVPE and could improve the FWHM of X-ray rocking curve from approx. 2000 *arcsec* down to about 500 *arcsec*.

In Fig. 3.17, a digital camera image of free-standing GaN is shown. As an effect of

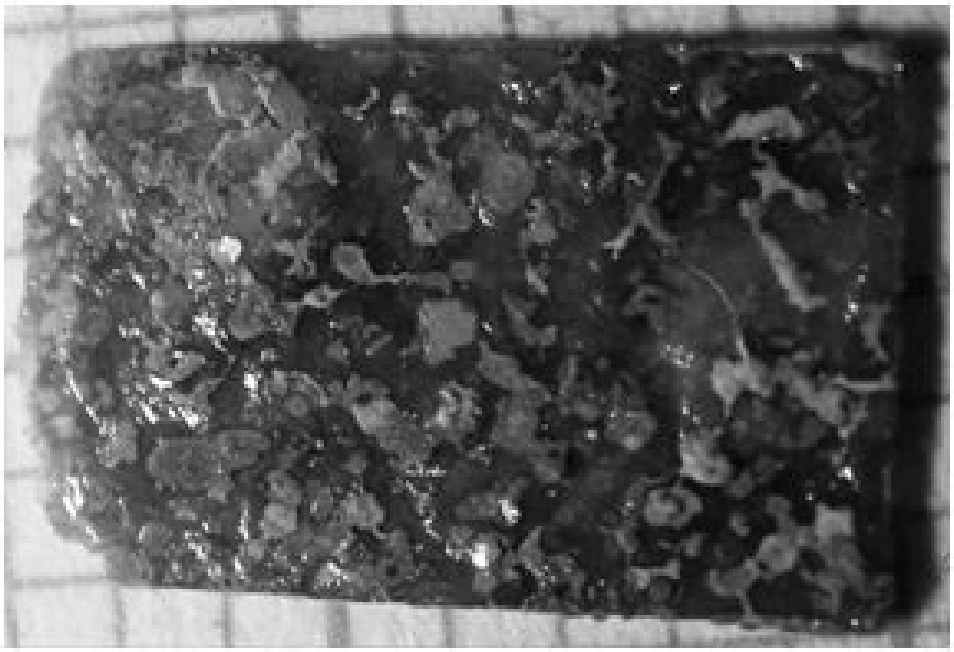

Figure 3.17: Free-standing GaN single crystal of thickness $> 150\ \mu m$, self separated from the $\beta - Ga_2O_3$ substrate

the cooling down step some GaN powder was formed and deposited on the surface of the grown single crystal. Free-standing GaN with a thickness of approx. $\sim 150\ \mu m$ was achieved when the growth time was extended to 72 h. The other parameters were kept as before. After the sample was removed from the seed holder, self-separation of the GaN with a thin, probably sub-micron thick layer of $\beta - Ga_2O_3$ occurred at room temperature. The easy separation of GaN layer at the interface can be explained by relatively weak bonding energy between monolayers along c- and b- axis of monoclinic $\beta - Ga_2O_3$ crystal. To get a more detailed analysis, the interface between $GaN/\beta - Ga_2O_3$ of a thin sample was studied by high resolution transmission electron microscopy (HRTEM).

Fig. 3.18 (a) shows a cross-sectional TEM image of a GaN layer grown on a-plane $\beta - Ga_2O_3$. With respect to growth and self-separation, four observations are important: (i) along extended parts of the interface an amorphous volume between the GaN layer and the substrate was observed, (ii) the GaN layer is linked only locally to the $\beta - Ga_2O_3$ substrate, (iii) the GaN layer itself is single crystalline and epitaxially grown with c-plane

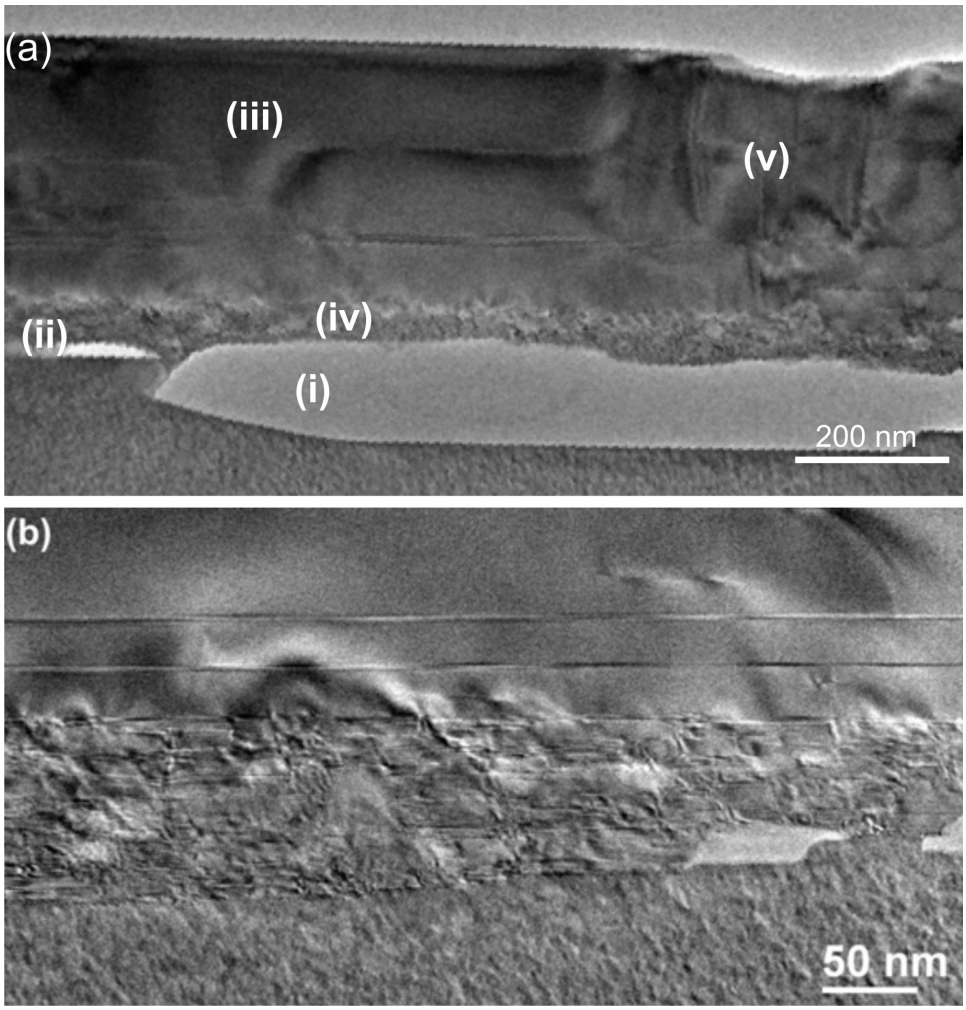

Figure 3.18: Low-magnification bright field TEM images of the interface area, (a) showing $\beta-Ga_2O_3$ substrate with areas of amorphous volume (i), connection between GaN and $\beta-Ga_2O_3$ substrate (ii), GaN film (iii), laterally overgrown GaN layer (iv), and high dislocation density at the islands boundary (v), (b) area (ii) GaN layer, containing lots of stacking faults

orientation on the a-cleavage plane of the substrate. In the GaN layer, two parts can be distinguished, Fig. 3.18 (b). First, a highly defective region (iv) is formed close to the interface between the layer and the substrate, which has a thickness of about $20-80\ nm$. This layer is characterized by a high density of stacking faults and dislocation loops. Then, the structure changes abruptly to wurtzite and only few stacking faults and dislocations are visible. The total density of threading dislocations (TDD) is roughly

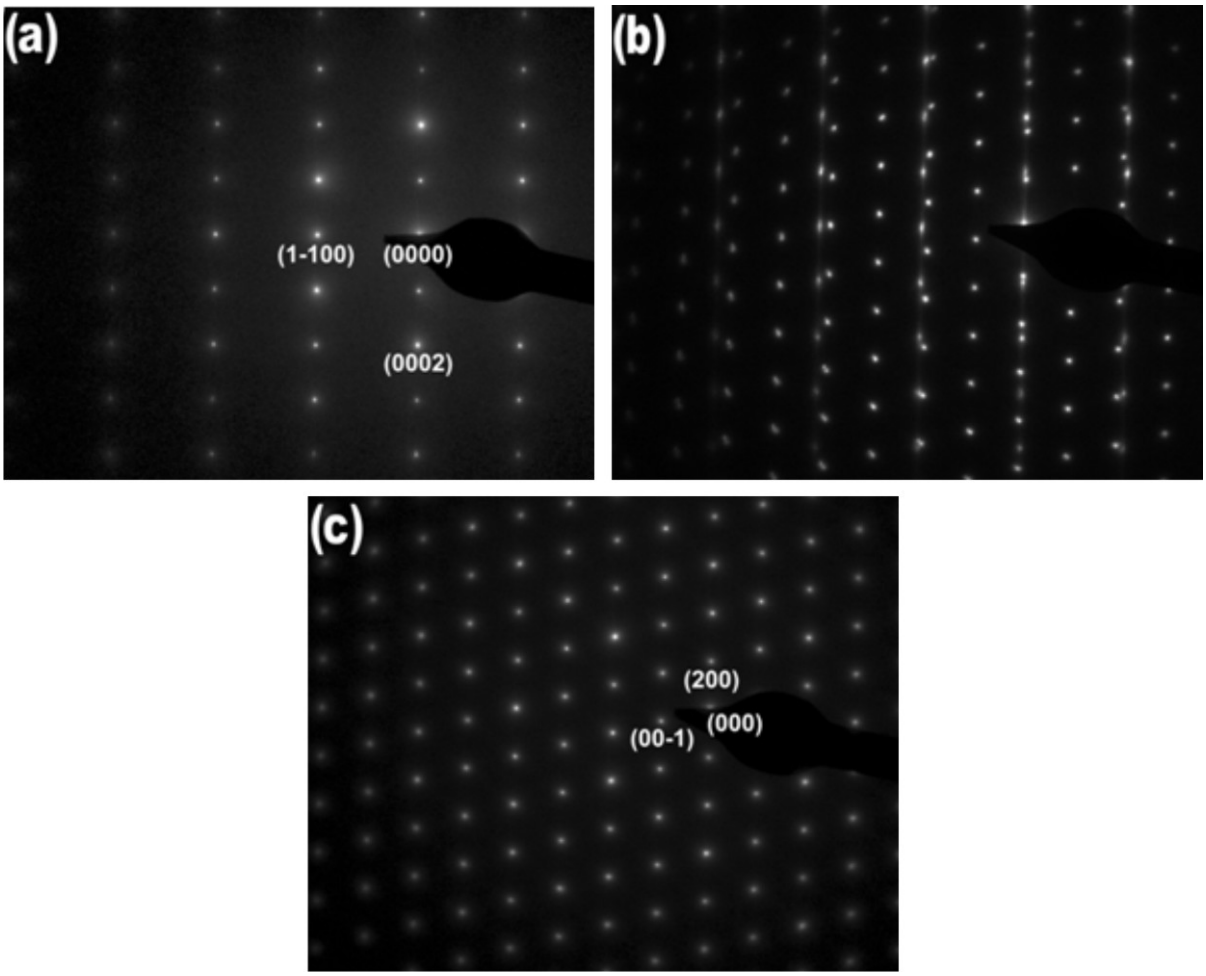

Figure 3.19: Selected area electron diffraction (SAED) patterns acquired (a) at the GaN film, (b) at the interface region and (c) at the $\beta - Ga_2O_3$ substrate

estimated from the cross-sectional TEM image to be 4×10^9 cm^{-2}, which stays in fair agreement with the XRD measurements.

The amorphous volume refers to under-etching before the GaN layer coalesced and filling the etched voids with amorphous material, which exact composition was impossible to identify. To determine the orientation relationship of the GaN film with respect to the (100) $\beta - Ga_2O_3$ substrate, selected area electron diffraction (SAED) was performed. Fig. 3.19 shows SAED pattern taken in the GaN film along the $[11\bar{2}0]$ zone axis (Fig. 3.19(a)), inside the $\beta - Ga_2O_3$ (Fig. 3.19 (c)) along the [010] zone axis; the SAED taken at the

interface region is a superposition of them (Fig. 3.19(b)). Thus, the observed orientation relationship corresponds to the previously reported one of (0001) GaN and (100) $\beta - Ga_2O_3$ [94] with the c-axis of GaN perpendicular to the (100) surface of $\beta - Ga_2O_3$ and the $[11\bar{2}0]$ axis of GaN parallel to the [010] axis of $\beta - Ga_2O_3$. The broadening of the GaN diffraction spots in Fig. 3.19(b) is due to the high defect density in the GaN layer close to the interface, while narrow spots in Fig. 3.19(a) represent considerable improvement of the crystalline quality with the distance from the interface, i.e., when the GaN film reaches a thickness of 100 nm.

For the given orientation relationship, the lattice mismatch between GaN and $\beta - Ga_2O_3$ is 4.7% along [010] direction and -5.0% along [001] direction. In Fig. 3.20 the sketch of GaN grown on $\beta - Ga_2O_3$ with indicated mutual orientation is shown. The values

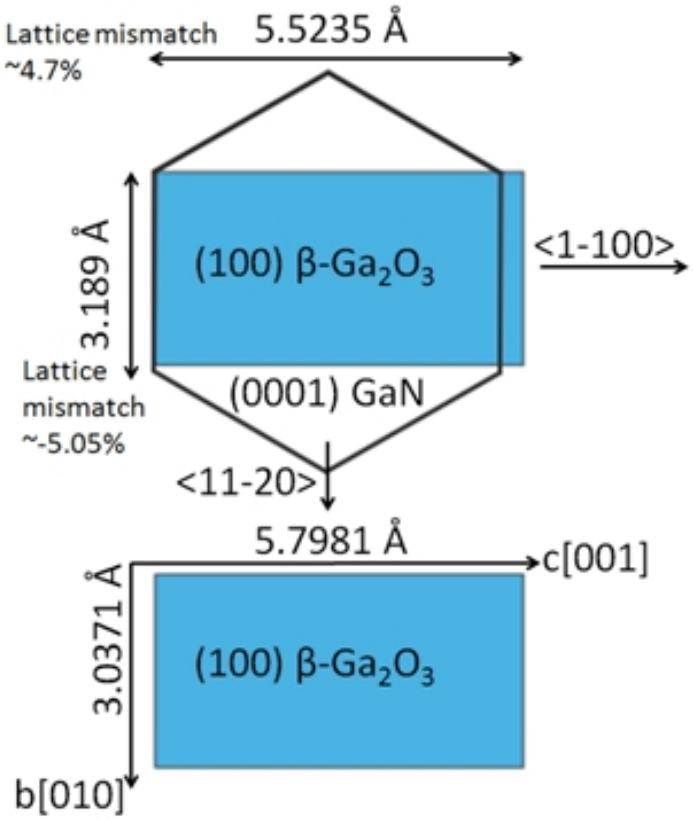

Figure 3.20: Mutual orientation and lattice mismatch of GaN grown on $\beta - Ga_2O_3$

obtained by the present study coincide with those reported by Ohira et al. [93]. Despite the difference of the crystalline structures, lattice mismatch and high defect density of the initially grown GaN layer, a sharp boundary with the $\beta - Ga_2O_3$ substrate is observed along the interface (Fig. 3.21 (a)).

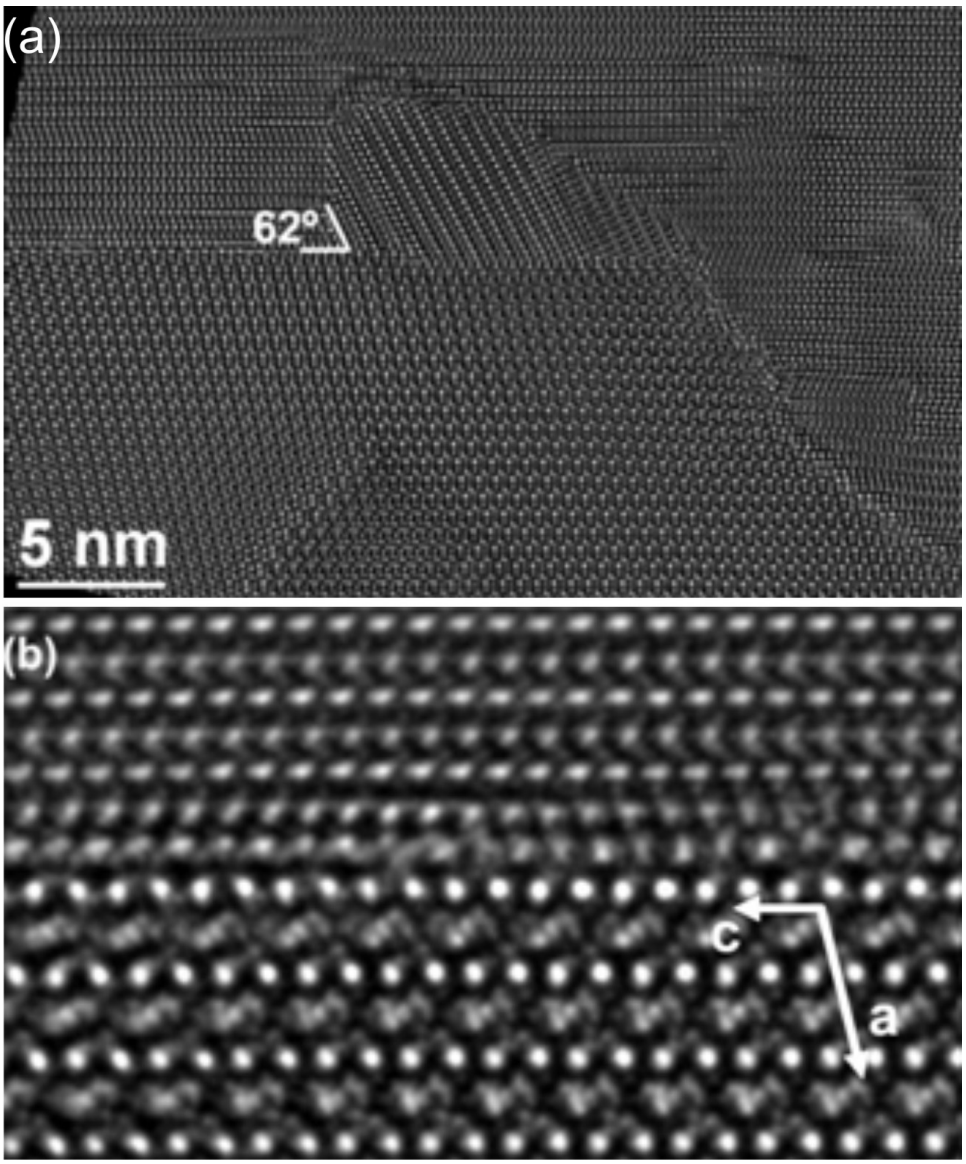

Figure 3.21: (a) High-resolution TEM image of the interface region taken along the [010] zone axis of $\beta - Ga_2O_3$ which shows GaN domain having semi-polar orientation, (b) is a magnification of the sharp regular interface of (a) showing basis vectors of the $\beta - Ga_2O_3$

At the same time, domains with inclination angle of about 62° from the c-plane of GaN are locally observed. This configuration corresponds to the $(1\bar{1}02)$ plane of GaN parallel to the (100) plane of $\beta - Ga_2O_3$ while the $[11\bar{2}0]$ axis of GaN remains parallel with the [010] axis of $\beta - Ga_2O_3$. For this orientation, the spacing between the Ga atoms along the $[1\bar{1}02]$ direction ($0.587nm$) is close to the length of the c basis vector of $\beta - Ga_2O_3$ ($0.579nm$), which lowers the lattice mismatch along [001] direction to 1.3%. The observed semi-polar portions better accommodate the lattice mismatch between GaN and $\beta - Ga_2O_3$. However, a higher growth rate along the [0001] direction results in predominant growth of GaN along the polar direction. Apparently, the highly defective structure of the polar GaN portions derives from lattice mismatch accommodation. While AFM measurements of the $\beta - Ga_2O_3$ substrate prior to growth reveal an atomically flat surface with an RMS of 0.47 nm, macroscopic steps with heights in the 10 nm range can be observed at the $GaN/\beta - Ga_2O_3$ interface. Local roughening of the interface forms during the initial stages of growth. To address this phenomenon in more detail, the following experiment was done: The gallium containing crucible was removed from the reactor to avoid intentional growth of GaN, and the reduction of the substrate by NH_3 was studied.

Fig. 3.22a shows an electron backscatter diffraction (EBSD) corresponding image quality map in grey scale, where areas of higher brightness correspond to higher crystal perfection. Sample of $\beta - Ga_2O_3$ was treated with NH_3 at $1080°C$ without a Ga source. It is proved that single crystal GaN layer and islands are formed as an effect of this process, which resembles the typical nitridation step carried out prior to MOVPE deposition of GaN on Al_2O_3 substrates. It is important to note that with this experiment we simulated the first stage of the standard growth process, where the Ga source temperature is still too low for effective gallium supply. Heating up the source to temperatures required for sufficient Ga transport stops the nitridation process and enables intentional growth of the GaN film by cyanide transport [76]. It can be clearly seen that the islands are characterized by a higher crystal perfection than the deposited layer. Layer and islands shown in Fig. 3.22a are grown in c-axis direction as evidenced by EBSD orientation maps

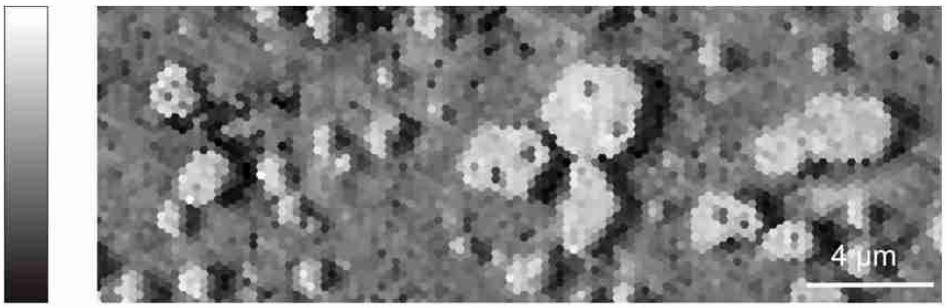

(a) EBSD corresponding image quality map; where areas of higher brightness correspond to higher crystal perfection

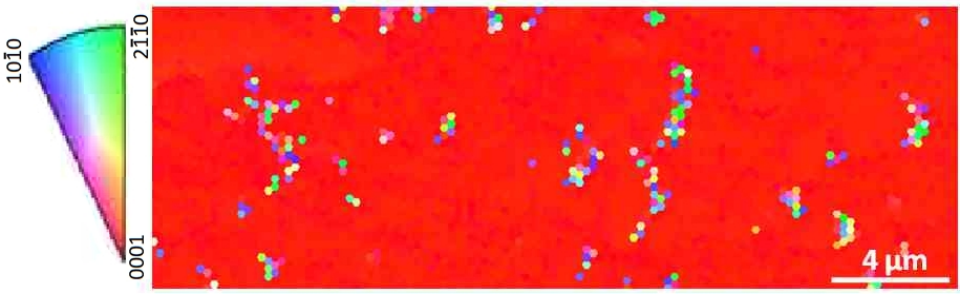

(b) EBSD corresponding crystallographic orientation map; where different colors correspond to different orientations

Figure 3.22: EBSD measurement of GaN on $\beta - Ga_2O_3$

in Fig. Fig. 3.22b. The sample is c-oriented. The different colors come from the electron shadowing effect and subsequent loss of information adjacent to the higher islands.

Formation of GaN islands could be explained by a two step reaction. First, NH_3 starts to decompose already at $400°C$ in thermodynamic equilibrium. Our waste-gas analyses proved that only a small part of ammonia stays undecomposed during the heating up process. Therefore, H_2 molecules are produced in the reactor from ammonia pyrolysis. Experiments with annealing of $\beta - Ga_2O_3$ substrates under H_2 atmosphere showed that decomposition of $\beta - Ga_2O_3$ substrates appears already at $800°C$. After annealing, Ga droplets were observed on the substrate surfaces. Moreover, Ga droplets formed in such reaction rapidly react with NH_3 to GaN and form islands. Such mechanism might be explained by equations 32 and 33:

$$Ga_2O_3(s) + 3H_2(g) \rightarrow 2Ga(liq) + 3H_2O(g) \tag{32}$$

$$2Ga(liq) + 2NH_3(g) \rightarrow 2GaN(s) + 3H_2(g) \tag{33}$$

The FactSage calculation presented in Fig. 3.23 shows that the probability of Ga_2O gas formation through reduction of $\beta - Ga_2O_3$ substrates by H_2 increases with rising temperature. Therefore, formation of GaN layer on $\beta - Ga_2O_3$ during the nitridation

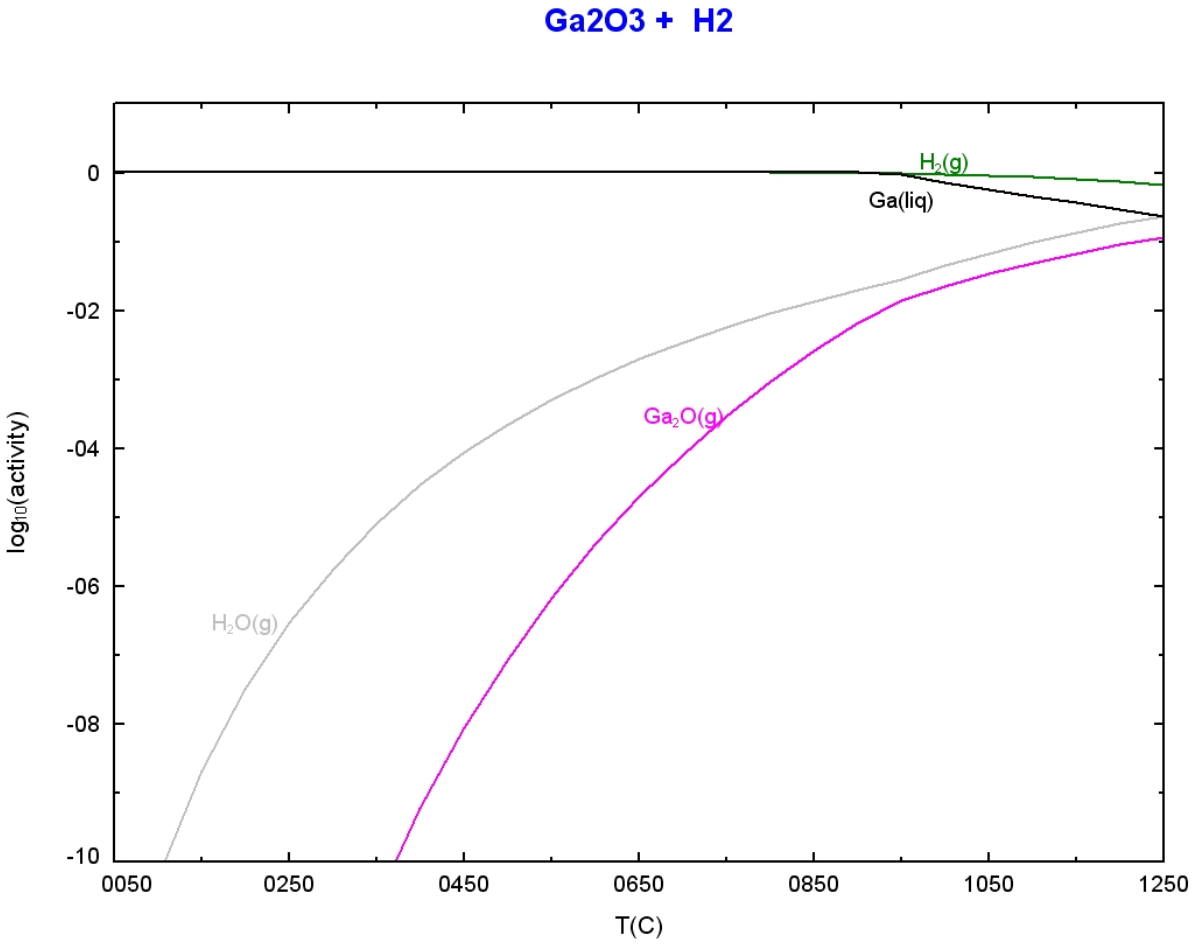

Figure 3.23: Reduction of $\beta - Ga_2O_3$ substrate by H_2 - 'FactSage' calculations (Inputs: $Ga_2O_3 + H_2$)

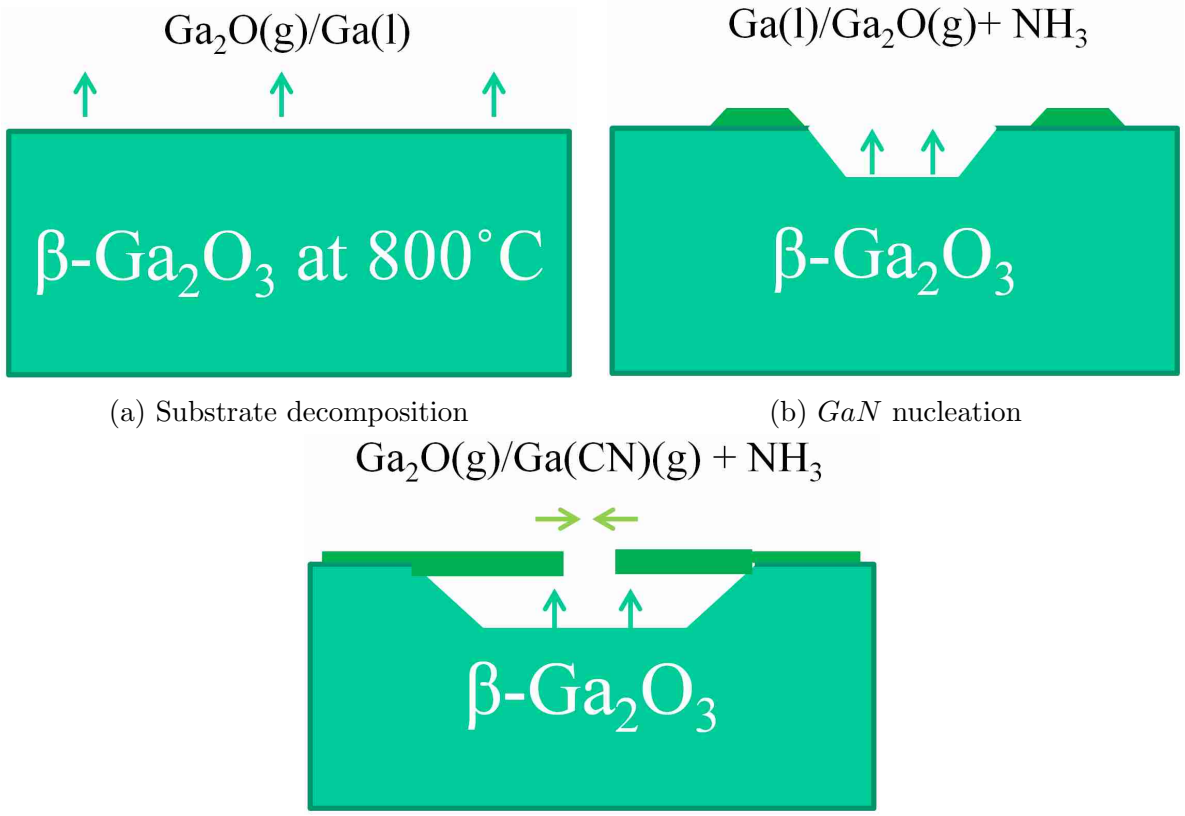

(a) Substrate decomposition

(b) GaN nucleation

(c) Lateral overgrowth

Figure 3.24: Schematic model of GaN on $\beta - Ga_2O_3$ formation

step at higher temperatures can be also explained by reactions 34 and 35. Hydrogen gas in contact with solid $\beta - Ga_2O_3$ substrates forms gaseous Ga_2O and water vapor, in this way etching and roughening the substrate surface. The model described above is schematically shown in Fig. 3.24a and 3.24b.

$$Ga_2O_3(s) + 2H_2(g) \rightarrow Ga_2O(g) + 2H_2O(g) \tag{34}$$

The Ga_2O vapour reacts with NH_3 to GaN which is deposited back on the substrate.

$$Ga_2O(g) + 2NH_3(g) \rightarrow 2GaN(s) + H_2O(g) + 2H_2(g) \tag{35}$$

Such mechanism was already proposed by Nam et al. [98]. Growth of GaN by using Ga_2O vapor transport is described by Imade et al. [99]. The proposed two-step mecha-

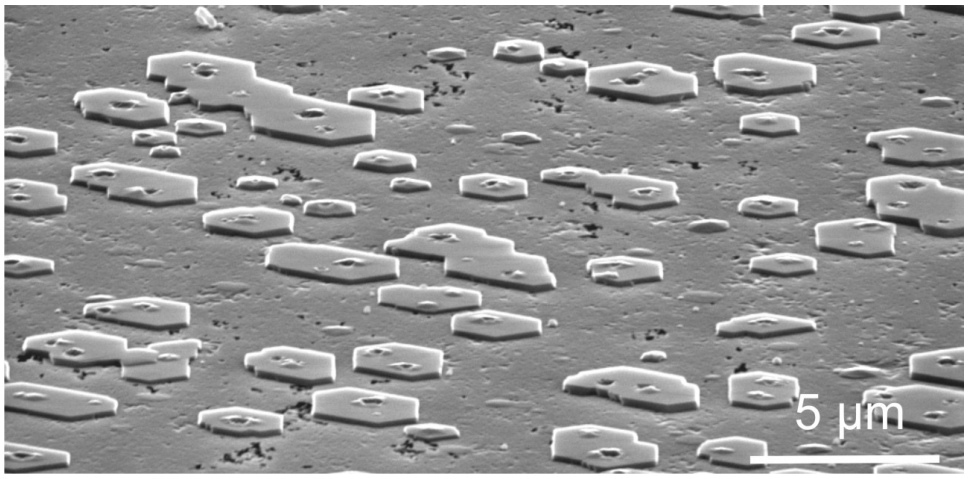

Figure 3.25: Birds view SEM image of GaN grown during high temperature NH_3 treatment of $\beta - Ga_2O_3$ substrate

nism accounts for the occurrence of highly defected GaN layer directly at the $\beta - Ga_2O_3$ surface.

With time, GaN islands increase in size and grow laterally over the low quality GaN layer (Fig. 3.24c). The same effect is used in pendeo-epitaxy [100] or in HVPE while masking of the sapphire is used [101, 102]. The SEM micrograph of Fig. 3.25 shows the same sample as in Fig. 3.22 (the $\beta - Ga_2O_3$ sample after treatment with NH_3 at $1080°C$ without presence of Ga source) tilted by 75°. Some of the islands shown in this figure already coalesce during nitridation step. Nevertheless, lateral overgrowth of the islands results in formation of numerous threading dislocations at their coalescence boundaries which is marked as area (v) in Fig. 3.18(a). On the other hand, the highly defective GaN layer formed at the nitridation step acts as a buffer layer for the subsequent growth of thick GaN films. During standard growth process with the presence of a Ga source, $GaCN$ is the main component for Ga transport. As shown in eq.24 and eq.26, GaN is formed by reaction of NH_3 with $GaCN$. In this step, the GaN islands increase their sizes and coalesce to form a continuous layer already after reaching 400 nm in thickness; this was proved by cross-sectional TEM measurements described previously.

3.3 Graphite-free reactor

Promising results presented in chapters 3.1 and 3.2 motivate to continue the development of PHVPE technique. However, it made no sense to proceed with a graphite containing setup. The growth experiments were not reproducible, runs differ between each other significantly in the mass transport (growth rates).

The prerequisite for controlled carbon doping is a carbon free reactor setup. The commercial HVPE reactors are made of quartz, due to its chemical stability, machinability and low price. Despite the limitation of upper process temperature, it was decided to use quartz for our reactor design as well. The main goal in comparison to the previous set-up was to remove all graphite/carbon parts, and supply the carbon with a gaseous precursor, in order to provide controlled carbon content for HCN synthesis.

3.3.1 Experimental set-up

The sketch of the reactor is shown in Fig. 3.26. Taking into account the HCN toxicity, the reactor was designed with an intermediate enclosure. In case of a leak, HCN can not escape to the reactors containment.

The sealings of the quartz cylinders (Fig. 3.26 (5) and (6)) to the top and bottom stainless steal flanges were made with ethylene propylene diene monomer (EPDM) rubber seals as this material can by used under hydrocarbon, ammonia and concentrated acid environment up to $150°C$. Other quartz parts such as gas lines were sealed also with EPDM seals.

The outer thermal isolation has been designed in form of two half-cylinders (Fig. 3.26 (57) and (56)) made of altraform as discussed previously in chapter 3.2.

Two resistive heaters are used in this construction (Fig. 3.26 (15) and (16)). The heating elements are made of 2 mm thick A-1 Kanthal wire. They are able to work under air (oxygen) up to $1400°C$ continuously and up to $1450°C$ for a short time. Alumina bars, cylinders and discs were used to support the stability of the heater (Fig. 3.26 (11), (12) and (13)). A photograph of the heaters is presented in Fig. 3.27.

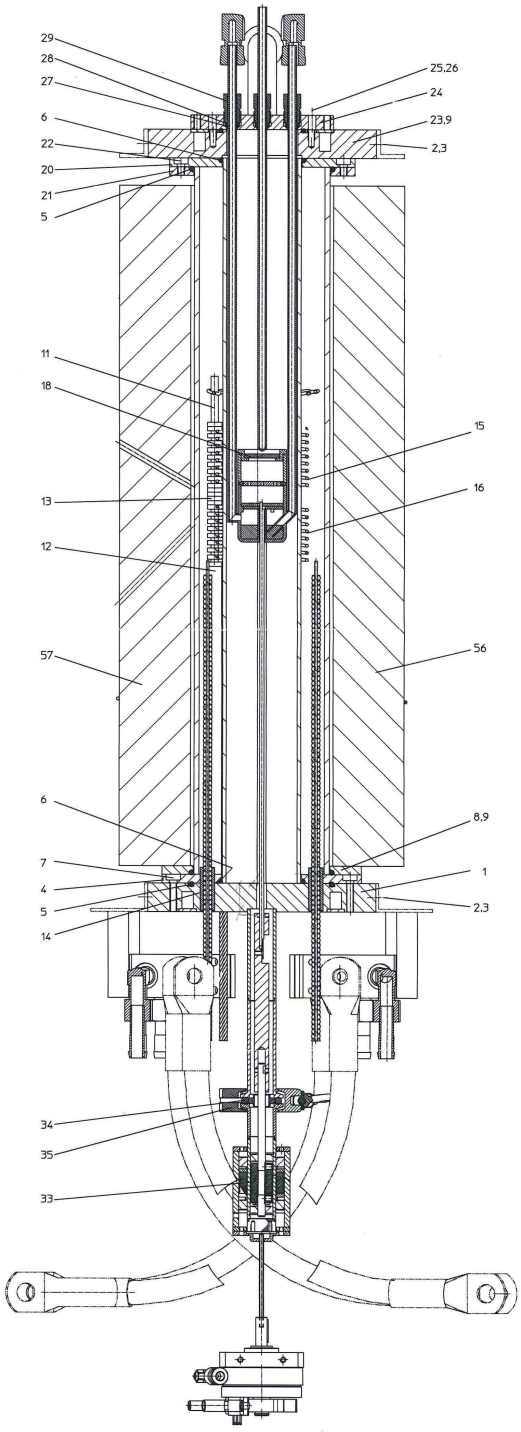

Figure 3.26: Sketch of the reactor: (1; 4; 5) outer tube sealing system, (6; 7) inner tube sealing system, (11; 12; 13) heaters stability support, (14) electrical throughputs, (15; 16) top and bottom heaters, (18) growth cell, (27; 28; 29) gas lines sealing systems, (56; 57) outer isolation cylinder

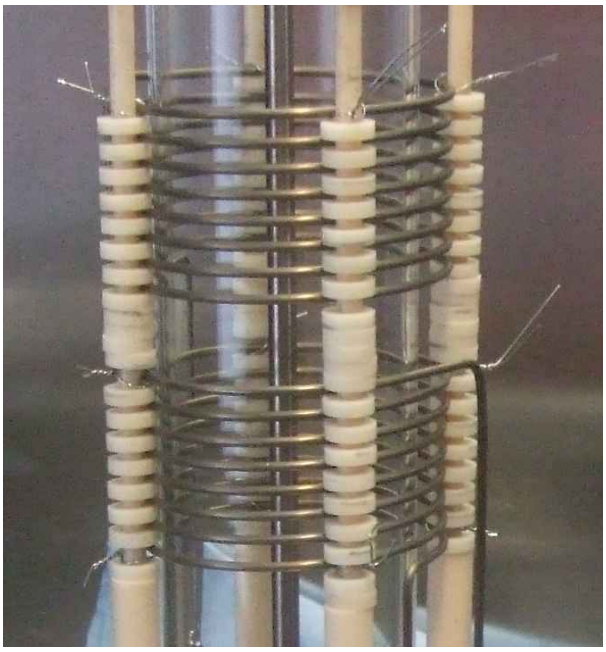

Figure 3.27: Camera picture of bottom and top heater mounted on the supporting bars and discs

Growth cell

The detailed $3D$ drawing of the growth cell is shown in Fig. 3.28a.

The growth cell consists of four main components, crucible, diaphragm, ring shower, and seed holder. The role of the diaphragm is to separate the NH_3 ring shower outlet from the liquid Ga surface in the crucible. According to the fact that NH_3 decomposes on hot surfaces more efficient than within the gas phase, it was shown by FTIR measurement, that nearly 100% of ammonia is decomposed after passing through the diaphragm at $1150°C$.

The outlet of the NH_3 shower line points to the seed. The distance between the outlet and the seed holder is approx 5 mm. Two exhaust gas holes are attached to the ring shower.

The crucible with two attached gas lines serves as bottom of the growth cell. The first one, the N_2 transport line, is responsible for increasing the flow against NH_3 from the ring shower and enhancing the transport of the $GaCN$ component to the seed holder.

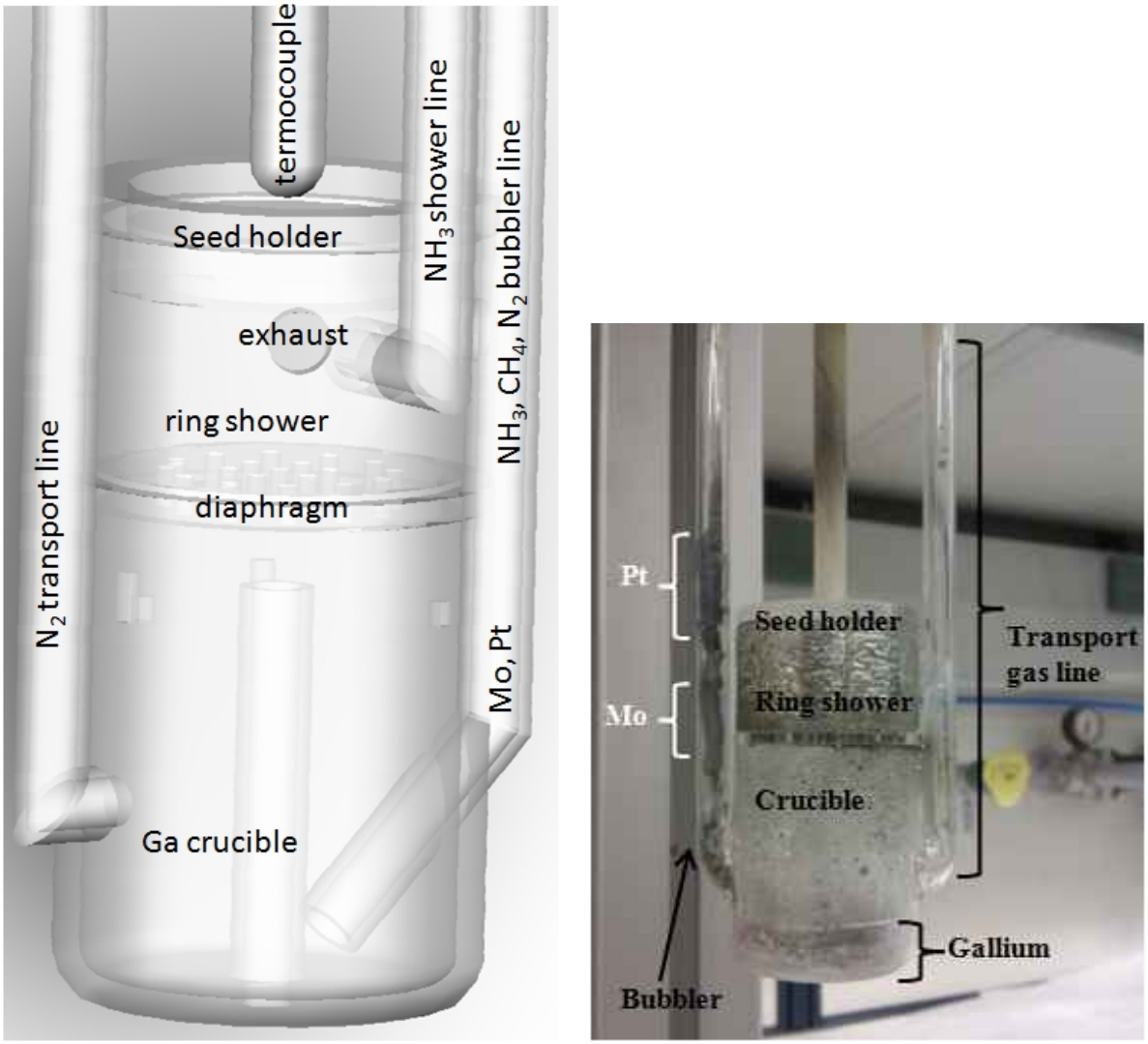

(a) 3D model of the growth cell with indicated parts and gas lines

(b) Real picture of the growth cell after the process

Figure 3.28: Growth cell

The second is the bubbler line. Its outlet ends below the liquid Ga surface. Therefore gas could be bubbled through the liquid Ga during the process, what prevents the crust formation and reduce the effective surface tension. The second role of the bubbler line is to form HCN from NH_3 and CH_4 over Pt catalyst. The bubbler line is crossing the hottest place in the reactor, since it passes the heater in a small distance. Therefore, the

temperature should be sufficiently high to form HCN preferentially in the line (especially with the catalyst present in the hot zone).

At the top of the growth cell a thermocouple in quartz cover is attached directly above the seed holder. Therefore, the temperature of the substrate during the process could be measured precisely and continuously. The second thermocouple measures the temperature from the bottom of the crucible, it is used to check the gradient between the top and the bottom of the growth cell. It is also possible to move the bottom thermocouple during the process from the reactor bottom along the whole cell up to approx. $\sim 30\ mm$ above it.

In Fig. 3.28b the real picture of the growth cell after the process is presented. Black color of the ring shower is due to carbon deposition which will be discussed later in chapter 3.3.5.

Gas lines and control panel settings

Schematic view of the reactor control panel is shown in Fig. 3.29. There are four gas lines on the left side attached to mass flow controllers (MFC). The first line from the top is the NH_3 line divided in two parts: ring shower (light blue) and bubbler (green). The second gas is either H_2 or O_2 connected to the ring shower. The third is CH_4 (indicated as CH_x) used only for the bubbler. The last is N_2 connected to both - bubbler and carrier (purple) gas lines.

Each gas line has its own pressure gauge to measure the pressure inside. The overpressure security system is connected to all pressure measurement devices. After reaching the pre-set security values it closes all valves on the left side of MFC's to avoid unintended pressure rises.

On the right side the control of the top and the bottom heater is shown, the calculation of the heater wire temperature is based on the changes in electric resistance. In the middle of the reactor part 3 thermocouples indicate the temperature of the seed holder - 'c' and the bottom of the crucible - 'a'. Thermocouple 'b' is movable and could be attached to various points during the process. All thermocouples are of type 'K' (NiCr-NiAl),

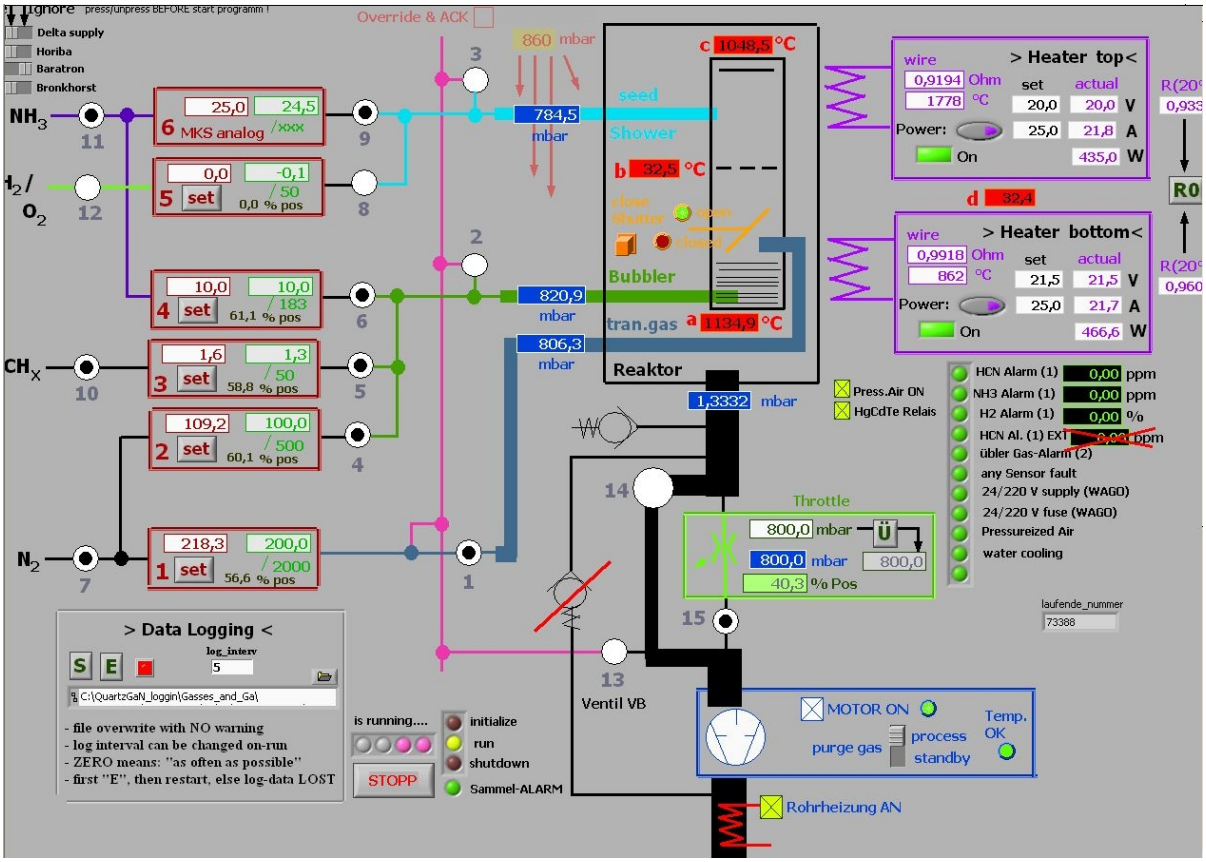

Figure 3.29: LabView programmed control interface used in carbon-free reactor

sensitive for the temperature range -200 up to $1200°C$.

On the bottom of the control interface the pumping and the exhaust system are attached. Two pressure sensors exist - first one with pressure measurement range below 1.2 $mbar$ and the second one attached to the throttle valve operating at $1 - 1200$ $mbar$.

At the right side below the heater control system, the gas sensors for NH_3, H_2 and HCN are shown. Additionally, at this place all other warning signals such as: cooling water flow, pressurized air status, etc, are placed.

The additional security 'drop line' marked in pink color connects directly all gas lines to the pumping system. In case of an emergency situation all gas lines can be pumped down to 10^{-3} $mbar$ in less than half a minute.

3.3.2 Reactor modeling

Numerical simulations of the temperature and flow distribution inside the reactor were done in Virtual Reactor VR-HVPE AlN/AlGaN/GaN (HEpiGaNS) version 6.4 from STR IP Holding, LLC. The simulations show the thermal gradients between crucible and seed holder and the gas flow velocities inside reactor, respectively. As the software assumes rotational symmetry ("2.5D modeling") it was necessary to provide data for an artificially simplified set-up and to make few adjustments i.e. removing the gas lines from the schema and keeping only gas outlets. The gas outlets crosscuts were recalculated to keep the same area when adjusted for rotational symmetry. Nevertheless, the temperatures measured during experiment with thermocouple are in good agreement with the calculations, with just few percent of the discrepancy.

In Fig. 3.30 the influence of the relative position between growth cell and heaters on the axial temperature gradient inside the growth cell is presented. In Fig. 3.30a the simulated seed temperature was 1019°C, the bottom of the growth cell 1083°C, the diaphragm 1079°C. For the other case presented in Fig. 3.30b the seed temperature was 1038°C, the bottom of the growth cell 1074°C, the diaphragm 1085°C.

The operation of setup with the growth cell in the middle (bottom of the growth cell 34 mm below the first spiral of the bottom heater) has been also studied. In this case changing the power of one heater changes significantly the temperature of the seed holder and crucible bottom simultaneously. It makes the process temperature hard to control and unpredictable. While positioning the growth cell in the way presented in Fig. 3.30a changing the temperature of the process is much easier and more predictable. In this case the bottom heater heats mostly the crucible (Fig. 3.31a). At high temperatures, when both heaters are turned on the bottom heater has just a weak influence on the seed holder. Therefore, it can be used to control and keep the gradient and source temperature. The top heater can be used to keep the temperature of the seed holder on the desired level. Additionally the top heater keeps the bottom of diaphragm at higher temperature than the liquid gallium surface to avoid condensation of Ga and to enhance the NH_3 decomposition (Fig. 3.31b).

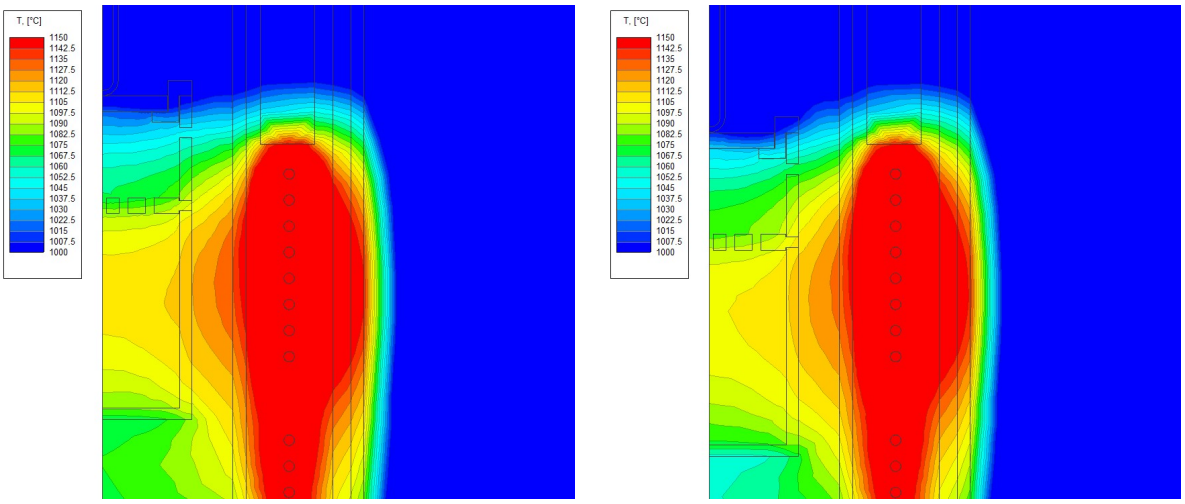

(a) Temperature gradient inside the growth cell aligned 4 *mm* above the first spiral of the bottom heater

(b) Temperature gradient inside the growth cell aligned 3 *mm* below the first spiral of the bottom heater

Figure 3.30: Influence of the growth cell position on temperature gradient inside the cell

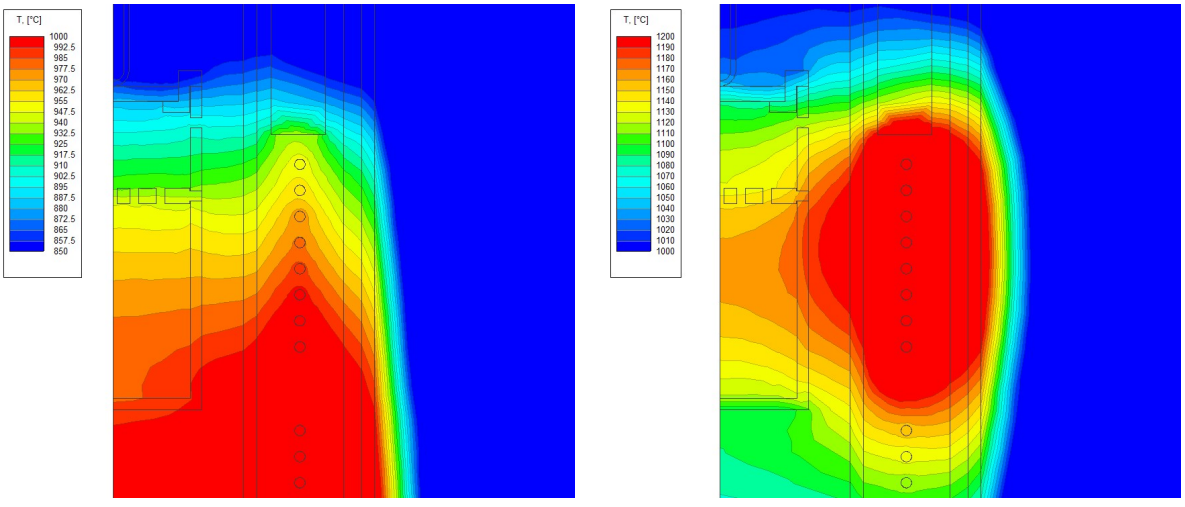

(a) Temperature gradient inside the growth cell with top heater off

(b) Temperature gradient inside the growth cell with bottom heater off

Figure 3.31: Influence of the heater power on the temperature inside the growth cell for the heater position as in Fig. 3.30a

Fig. 3.32 shows the influence of the flow rates below and above the diaphragm for the heater position as in Fig. 3.30b. The calculation shows, that the gas flow velocity is

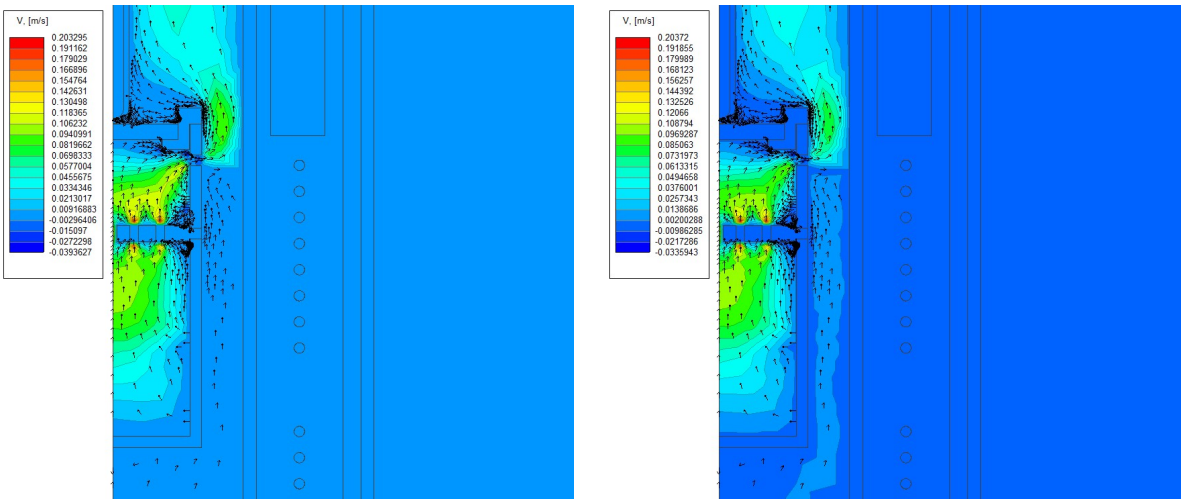

(a) Calculated gas flow velocity for given flow rates: 350 *sccm* below diaphragm and 200 *sccm* above diaphragm

(b) Calculated gas flow velocity for given flow rates: 350 *sccm* below diaphragm and 100 *sccm* above diaphragm

Figure 3.32: Influence of the flow rates on the flow velocities inside the growth cell for the heater position and power as in Fig. 3.30b

highest on the top side of the diaphragm. It also shows, that doubling the flow of NH_3 above the diaphragm did not influence significantly the velocity of gases coming through the diaphragm. It proved that the diaphragm works not only as decomposition center for NH_3 but also is blocking the ammonia from flowing against the stream of gas from the source crucible.

Presented above calculation data were helpful during the reactor development. Though the model needed to be significantly simplified, the simulated trends of temperatures, gradient etc. were confirmed in the first experiments.

3.3.3 Choice of carbon precursor

Despite the many process routes and precursors described in literature, there are two commercial processes - Andrussow (eq.36) and Degussa (eq.37) to produce HCN and both are based on the reaction of methane with ammonia [103, 104].

$$CH_4(g) + NH_3(g) + 3/2O_2(g) \rightarrow HCN(g) + 3H_2O(g) \tag{36}$$

$$CH_4(g) + NH_3(g) \rightarrow HCN(g) + 3H_2(g) \tag{37}$$

In case of the Andrussow method there is also O_2 used for the reaction. It decreases the required process temperature down to $1050°C$ - $1100°C$ while otherwise $1150°C$ - $1250°C$ is necessary [105, 106, 107]. Both reactions occur on a Pt catalyst. The advantages of the Degussa process are: higher HCN yield, higher NH_3 conversion, higher purity of the by-product H_2 [108]. Moreover, the biggest advantage is the absence of O_2 and therefore H_2O in the system. Since the goal of the new reactor is to grow semi insulating material,

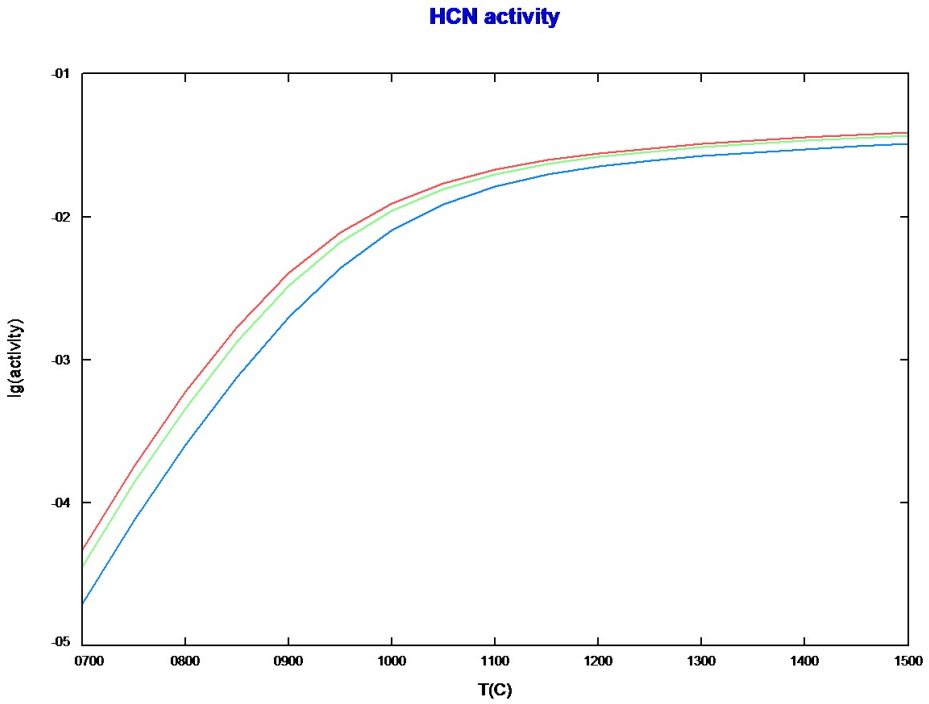

Figure 3.33: FactSage calculation of HCN activity vs. temperature for reactions: $CH_4 + NH_3$ (blue line), $C_2H_6 + 2NH_3$ (green line) and $C_3H_8 + 3NH_3$ (red line)

it is preferable not to include O_2, which is a donor in GaN, and would compensate the effect of carbon doping.

Different substances such as: C_2H_2, C_2H_6, C_3H_8, CH_3NH_2, etc. have been also considered as precursors for carbon doping. Nevertheless, the thermodynamic calculations presented in Fig. 3.33 indicated that increasing amount of carbon in the precursor molecules does not affect significantly the amount of produced HCN. There is 18% difference between HCN activity formed in reaction of NH_3 either with CH_4 or C_2H_6. The difference between HCN activity from reaction of NH_3 with C_2H_6 and C_3H_8 is only 7%. Nevertheless, using hydro-carbon gas with a higher content of carbon increases significantly the amount of pure solid carbon in the system - if there is a decomposition of molecules or reaction with only one molecule of NH_3. Additionally, there would be significantly more H_2 which could interact with the substrate and at process temperature decompose the grown layer. Therefore, it was decided to use the classical Degussa process for HCN synthesis according to eq.37.

In Fig. 3.34a FactSage calculation of activity vs. temperature shows that at 950°C the

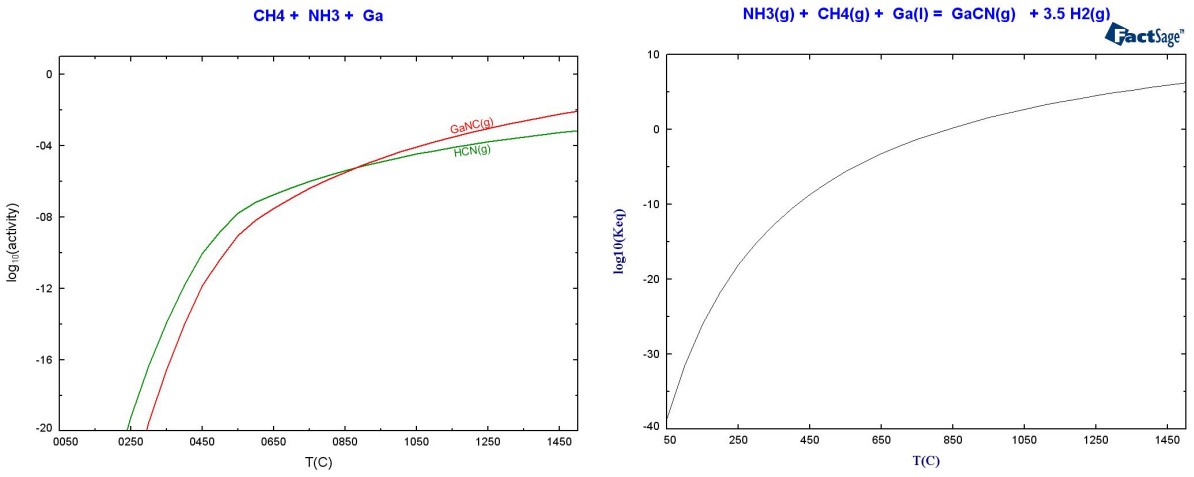

(a) Activity of HCN (green) and $GaCN$ (red) components vs. temperature - FactSage calculation

(b) Equilibrium constant vs. temperature for reaction of $CH_4(g) + NH_3(g) + Ga(l) \rightarrow GaCN(g) + H_2(g)$

Figure 3.34: FactSage calculation of equilibrium constant and activity vs temperature for $GaCN$ component

activity of $GaCN$ becomes higher than the activity of HCN. On the other hand, as seen in Fig. 3.34b - equilibrium constant vs. temperature indicates, that lgK_{eq} for reaction presented in eq.38 is higher than zero already at $850°C$ and for process temperatures of $\sim 1050°C$ reaches approx. the value $lg(K_{eq}) \approx 4$.

$$CH_4(g) + NH_3(g) + Ga(l) \rightarrow GaCN(g) + 7/2H_2(g) \tag{38}$$

The commercial Degussa process takes place at approx. $1200°C$ on Pt catalyst. As reported by Hasenberg and Schmidt [109, 110] the reaction between CH_4 and NH_3 does not occur in the gas phase. The authors observed a vanishing HCN formation rate, when the surface of either Pt or Rh catalyst was covered with carbon. Moreover, authors claimed that the highest reaction yield of 90% was obtained when the partial pressures of both reactants (NH_3 and CH_4) were in proportion $1:1$ [111].

3.3.4 In-situ characterization of exhaust gases

As presented in chapter 3.1.3 describing the carbon containing setup, FTIR is a useful tool to investigate the chemical nature of the reaction gases. In case of the carbon-free setup, presented in this chapter, an in-situ exhaust gas measurement system was developed.

In-situ FTIR setup

The sketch of the measurement system is shown in Fig. 3.35. The FTIR spectrometer is connected electrically and optically to the exhaust gas line of the reactor. Optical connections of the spectrometer were done by using $ZnSe$ windows at both ends of the exhaust gas cell. Using the optical fiber and the adapted optics, i.e. windows and mirrors, the light beam from the spectrometer is transmitted to the gas cell and travels 50 cm through the exhaust line. At the end of the exhaust line a mercury-cadmium-telluride (MCT) detector is adjusted to measure the light intensity. The detector is cooled with liquid nitrogen. The electrical detector signal is amplified by a low-noise

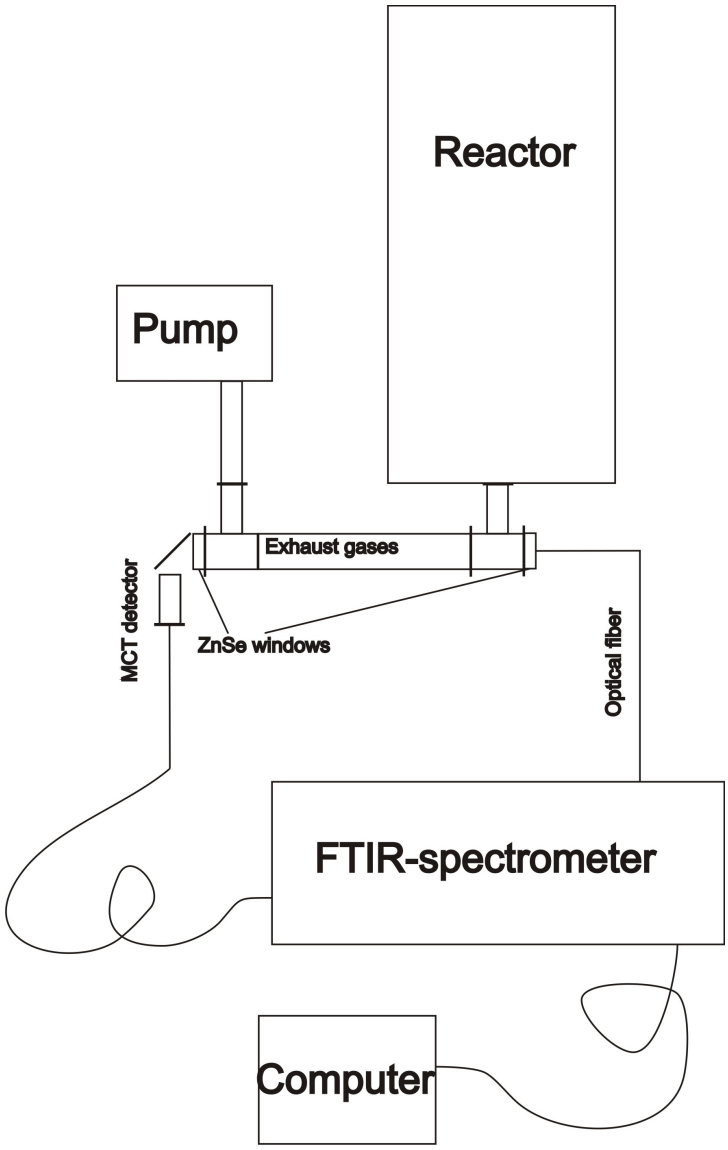

Figure 3.35: Sketch of the in-situ FTIR measurement setup

electrical amplifier and transferred back to the spectrometer. The gases flowing through the exhaust line are cooled down in respect to the growth cell atmosphere. Therefore, it is assumed that the measurements are carried out at room temperature.

Background sampling procedure

The measurement procedure was the same for all measured samples. The cold reactor was purged in minimum four times with 6N nitrogen. Then the whole volume of the reactor was pumped down to 3.3×10^{-3} $mbar$ and held closed under low pressure for approx. 15 minutes. During this time the leak rate was calculated according to the pressure rise. Typical leak rate was in the range of $2.5 - 4 \times 10^{-5}$ $mbar \times l/s$. Then the N_2 pressure was raised up to 800 $mbar$ and the background spectrum was collected. It was used as the background for all measurements during a single process. Before starting a new process the background spectrum collection was renewed.

Typical spectra

In Fig. 3.36 a typical FTIR spectrum collected during the experiment is presented. The upper wavenumber limit of 3500 cm^{-1} is given by the onset of absorption of the optical fiber. Nevertheless, absorption lines of all interesting components could be found in the range from $\sim 600 - 3500$ cm^{-1}. The important characteristic bands are marked in Fig. 3.36. Some of the absorption bands overlap with each other, making the quantitative calculation doubtful. Most problems arise from resolving the spectra of NH_3 and H_2O in the range of $1477 - 1775$ cm^{-1}. Nevertheless, if the NH_3 concentration is much higher than H_2O the presence of water vapor could be neglected. In case of low concentration of NH_3 the calculations of its content should be done using the bands in the range of $1200 - 800$ cm^{-1}, despite the fact that some overlap with the strongest HCN bands occurs. H_2O and CO_2 are extremely difficult to eliminate from the system, because of their presence in the ambient air. Due to the strong absorption of CO_2 and H_2O in this region the short path between the mirror and the optical fiber is enough for observing signals from these molecules in the background. All other parts of the FTIR measurement setup are constantly purged with $4.5N$ nitrogen. This procedure allowed to reduce the absorption of H_2O and CO_2 to a minimum and to decreased their influence on measurement results. Nevertheless it could not be completely excluded from the measurements and depending on the ambient air condition it could cause an error in the

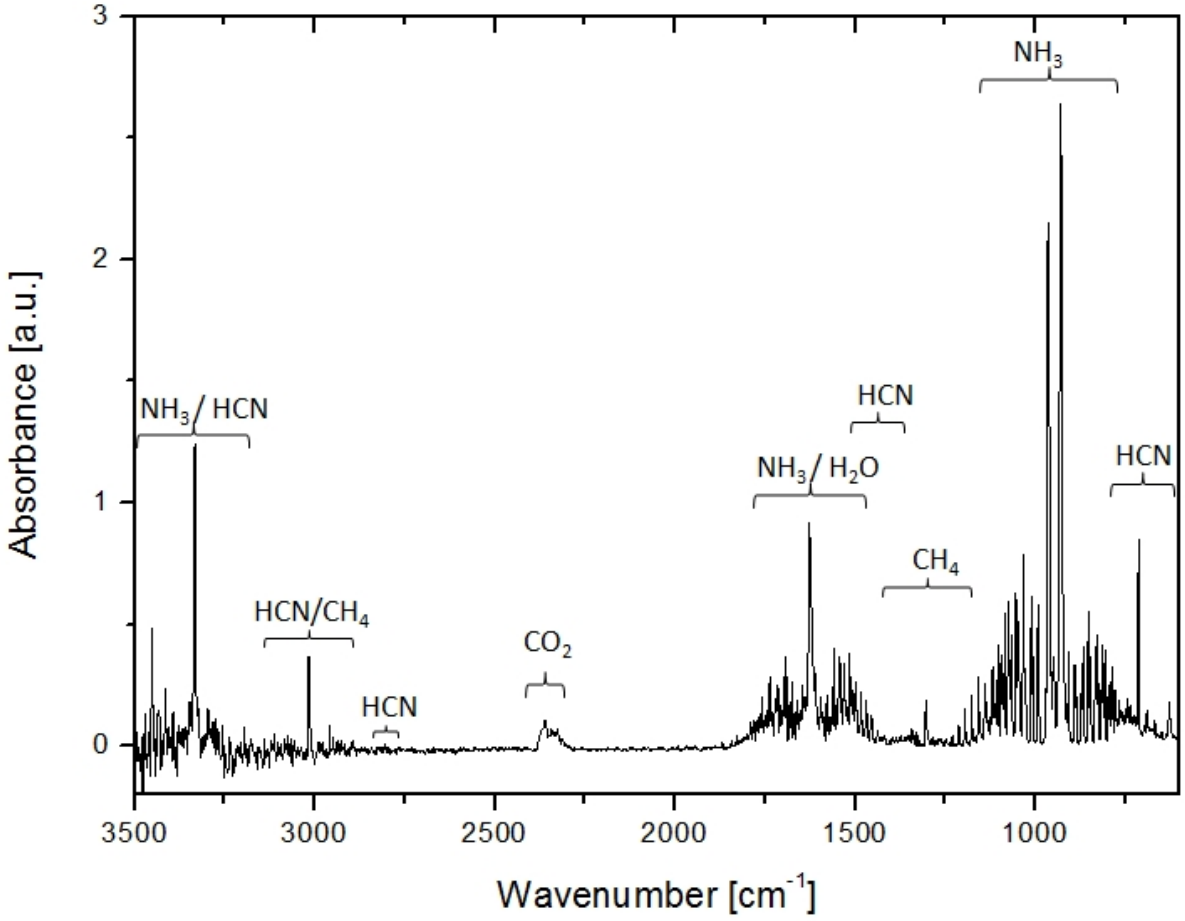

Figure 3.36: Typical FTIR spectra collected during the experiment

calculations up to approx. $\sim 5\%$.

3.3.5 Investigation of reaction path

The first experiments in the reactor were aimed to establish stable parameters of the HCN synthesis reaction. As described before it was decided to used the reaction between NH_3 and CH_4. It was observed, that a Pt catalyst shifts the reaction towards lower temperatures. Without Pt the first HCN signal in FTIR spectrum was recorded at $800°C$ while for experiments with Pt the first signal of HCN appeared already at $600°C$. Moreover, the yield of the reaction is increased significantly when Pt was present. In Fig. 3.37 the experimental results are presented. The flow of gases was the same in

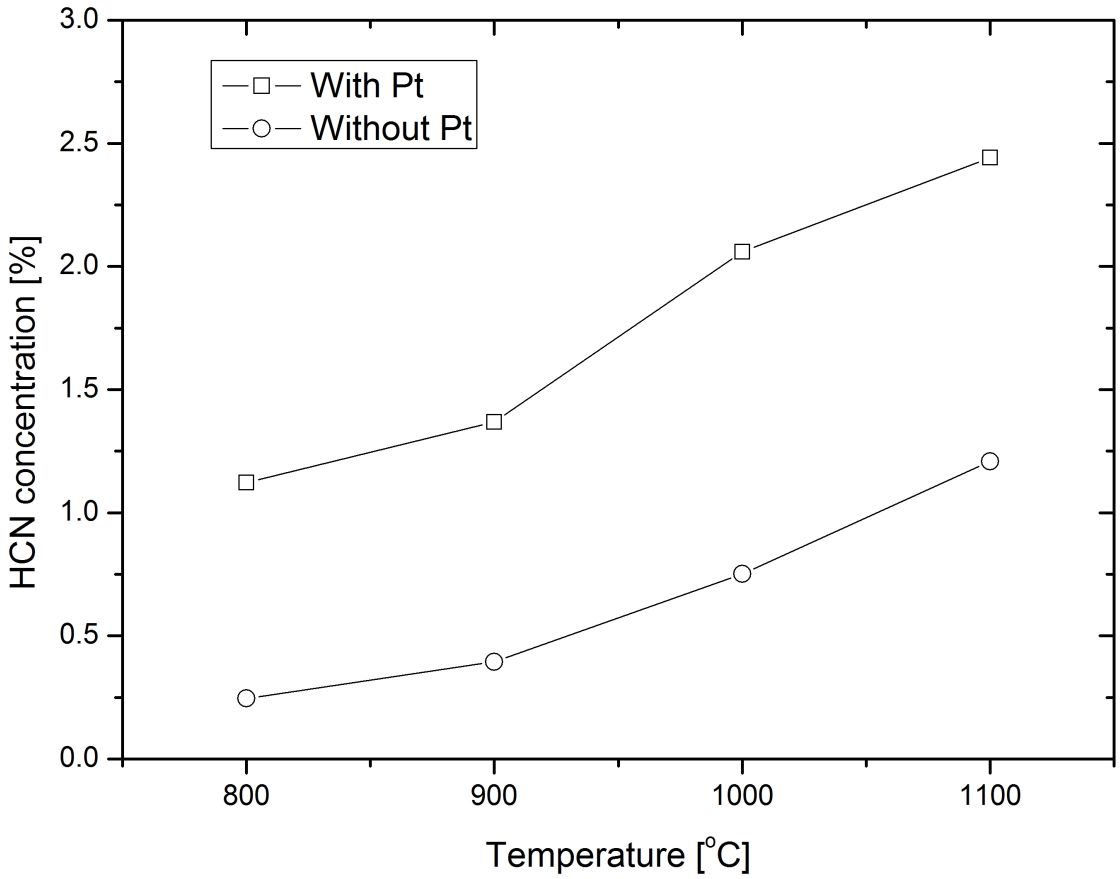

Figure 3.37: Concentration of the HCN in the exhaust gases for experiments with and without Pt catalyst

both cases; N_2, NH_3 and CH_4 were set for 10 *sccm* each. In case of experiment with Pt catalyst in place, strong NH_3 signal overlap with HCN occurred at temperatures below $800°C$. Therefore, the calculations were done in both cases starting from $800°C$. The shift in reaction onset of about $200 - 250°C$ is clearly visible. As the Degussa process does not take place in the gas phase [110, 109], the reaction occurred only on the quartz wall when no Pt was present.

In some experiments, very rapid carbon deposition on the reactor walls was found. As shown in Fig. 3.38 the layer was deposited allover the crucible, also on the outer side (as it was the hottest part due to the close distance to the heater). After removing the parts from the crucible the C-film started to peel off. FTIR experiments revealed

Figure 3.38: Part of the growth cell covered with C-film

that C-deposition was connected with C_2H_2 occurrence in the reactor at approx. $1000-1050°C$. Always when the unexpected acetylene band was observed in the spectra the carbon film was deposited. It was deposited also on the catalyst surface of the Pt and decreased significantly the yield of HCN synthesis. Similar behavior was also observed by Hasenberg and Schmidt [110]. The authors claimed that addition of 5% ethylene inhibited the reaction of HCN formation by one order of magnitude. The FactSage calculations showed, that the thermodynamics of decomposition of acetylene is fairly comparable to the decomposition of C_2H_4.

In the experiment whose results are presented in Fig. 3.39a, and lead to carbon film deposition as presented in Fig. 3.38, the flow of each gas: NH_3, CH_4 and N_2 inside the bubbler line was 10 $sccm$. The spectra were collected from $200-1000°C$. After reaching the final temperature spectra were collected also during cooling down.

At temperatures below $700°C$ the HCN band overlaps with the NH_3 band in the region $740-790cm^{-1}$. It is quantifiable only at temperatures at or above $700°C$. The C_2H_2 band overlaps completely with the HCN band at temperatures below $900°C$.

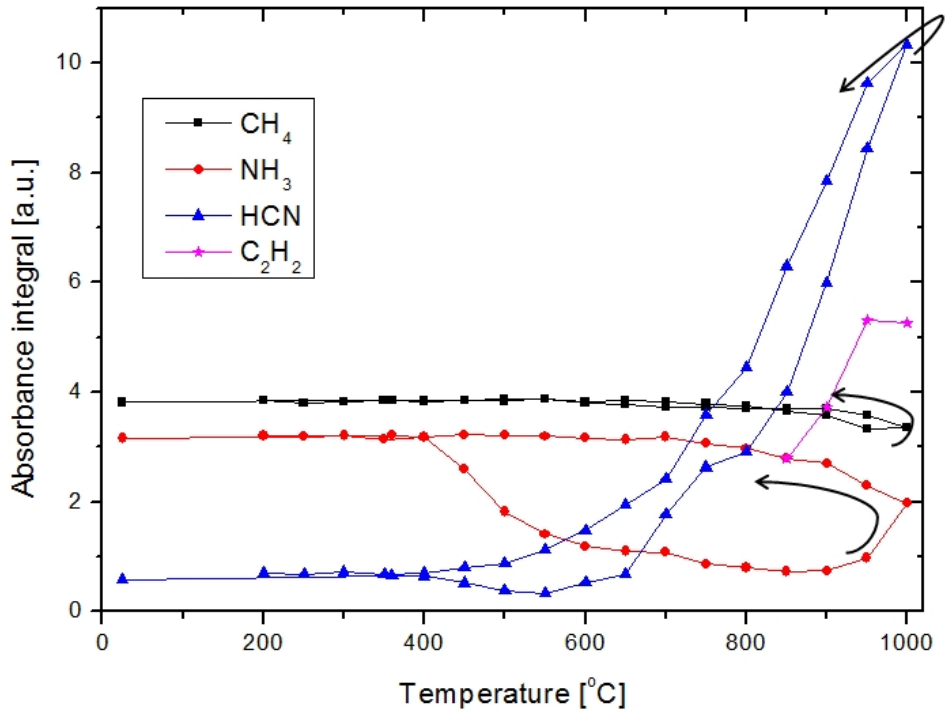

(a) Integrated intensity of spectra from process in which C_2H_2 bands were detected and the reactor was covered with C layer

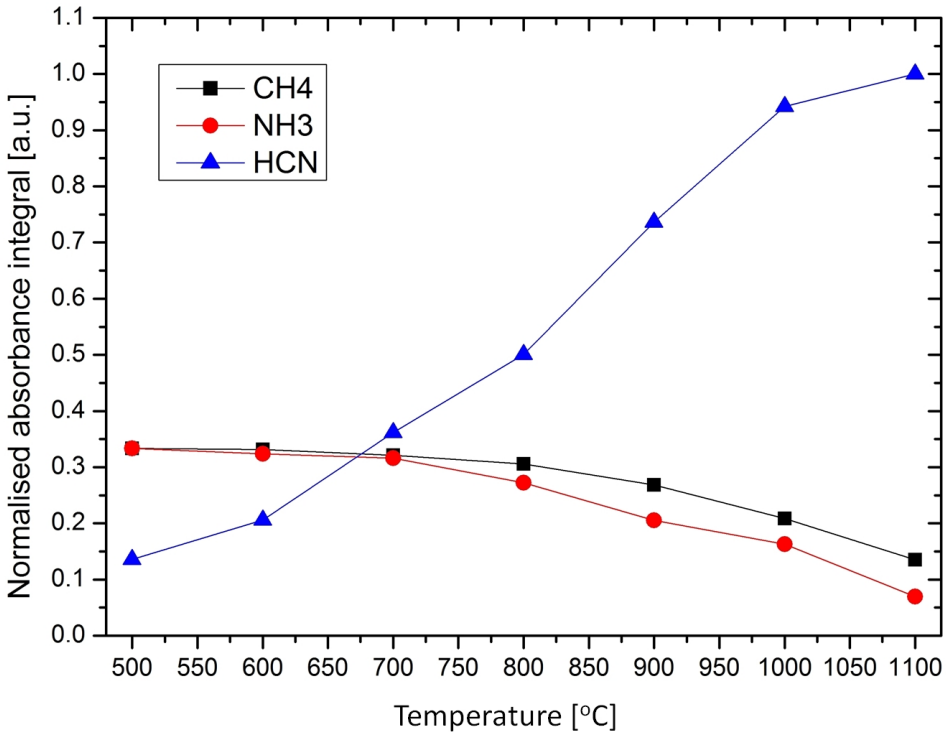

(b) Normalized integrated intensity of spectra from process in which C_2H_2 bands were not detected and the reactor remained clear after the process

Figure 3.39: Comparison of reactions with and without C film deposition

The ammonia concentration increases starting from 900°C due to the coverage of the Pt catalyst by a carbon film. At 900°C, and also after cooling down, the decomposition of NH_3 significantly decreases in comparison to heating up. A significant part of HCN band overlaps with C_2H_2 bands. Therefore, it does not indicate the real value. Due to complete band overlapping, quantitative measurements were not possible.

On the other hand, Fig. 3.39b shows the normalized absorbance integrals of spectra collected during a process where neither C_2H_2 band nor C film deposition was observed. Normalization for the NH_3 and CH_4 was done in such way, that the start concentrations were 30% each, and integrals were scaled according to the Beers-Lambert law. Therefore, with fair accuracy scale shows the fraction of NH_3 and CH_4 in the reactor exhaust gas line. Nevertheless, for HCN the values were normalized just to its maximum value and do not correspond to its concentration. The graph shows the typical and the predicted temperature dependency of all participants in the reaction of HCN synthesis: CH_4 and NH_3 concentrations decrease while the HCN concentration increases.

In an experiment with constant CH_4 and N_2 flows, temperature of 1050°C at the seed holder and with changing NH_3 flow, C_2H_2 in FTIR and carbon deposition were observed, when NH_3 excess over CH_4 was below $3:1$. Therefore, to avoid C_2H_2 formation, a strong NH_3 excess was applied. In the typical process the ratio of NH_3 to CH_4 was hold in the range of approx. $(7-10):1$ depending on the process.

The disadvantage of NH_3 excess is that any small amount of undecomposed NH_3 reacts rapidly with the Ga melt to form GaN. As shown in Fig. 3.40, all Ga from the crucible can be consumed for this reaction. Moreover, GaN formed by this reaction is extremely hard to remove from the crucible. It can be formed in the bubbler line, blocking this line and causing a pressure rise in the interior. Therefore, the processes with not sufficiently decomposed NH_3 were immediately interrupted, due to the lack of gas flow through the blocked gas lines.

Despite the problem described above it was necessary to keep an excess of the NH_3 in the bubbler line to avoid the C film deposition. Therefore, a metallic Mo mesh was added in the line below the Pt catalyst to decompose the unreacted NH_3 as it is shown

Figure 3.40: Picture of the crucible after two different processes where undecomposed NH_3 in the bubbler line accessed the liquid Ga reservoir

in Fig. 3.28b. Decomposition of ammonia on Mo surfaces at temperature above $600°C$ is known to be effective [112, 113]. Even approx 1 g of metallic Mo mesh in the bubbler line was enough to prevent formation of a GaN crust inside the crucible. Unfortunately, in the current set-up with limited space in the high temperature area of the bubbler line, the Mo mesh led to a $\sim 50\%$ decrease of the space for the Pt catalyst and therefore the yield of HCN synthesis decreased significantly.

3.3.6 Preliminary growth experiments

After establishing the stable HCN synthesis process, the first growth experiments were conducted. As a first step, the Ga transport was investigated. After 2.5 h at growth temperature with only bubbler gas flow (approx. $\sim$ 0.1 $sccm$ flow of HCN), the Ga mass loss in the reservoir was 0.03 g. Nevertheless, on the Al_2O_3 substrate some traces of Ga and GaN resulting from decomposition of $GaCN$ on the substrate, were detected. Thus, the Ga transport was small, but the principle was proved to work.

In the next experiment, NH_3 was additionally introduced through the ring shower. In this process 23.47 g of Ga were placed in the crucible so that the bubbler outlet was kept

underneath the melt surface. The Ga was bubbled with 200 $sccm$ N_2 flow. The reactive HCN was lead through the transport line. The flow of the gases through this line was set as:

NH_3 - 7 $sccm$ into the bubbler line and 25 $sccm$ into the ring shower line

CH_4 - 1 $sccm$ into the bubbler line

N_2 - 100 $sccm$ into the transport line

The measured temperature above the seed holder was $1030°C$ while on the level of the Ga melt it was $1115°C$.

Fig. 3.41 shows the result of deposition after 5 h process time under above described conditions. Approx. $\sim$ 0.16 g of Ga was transported from the reservoir. Many GaN islands were found on the Al_2O_3 substrate after the process. The main fraction of islands was c-oriented. Nevertheless, the islands did not coalesce and a significant number was grown in a random orientation. The size of the islands was up to $30-40$ μm, the height was up to 50 μm.

The FTIR measurement during this experiment (black curve in Fig. 3.42) shows that more than 95% of the CH_4 was consumed to form HCN. Only small traces of

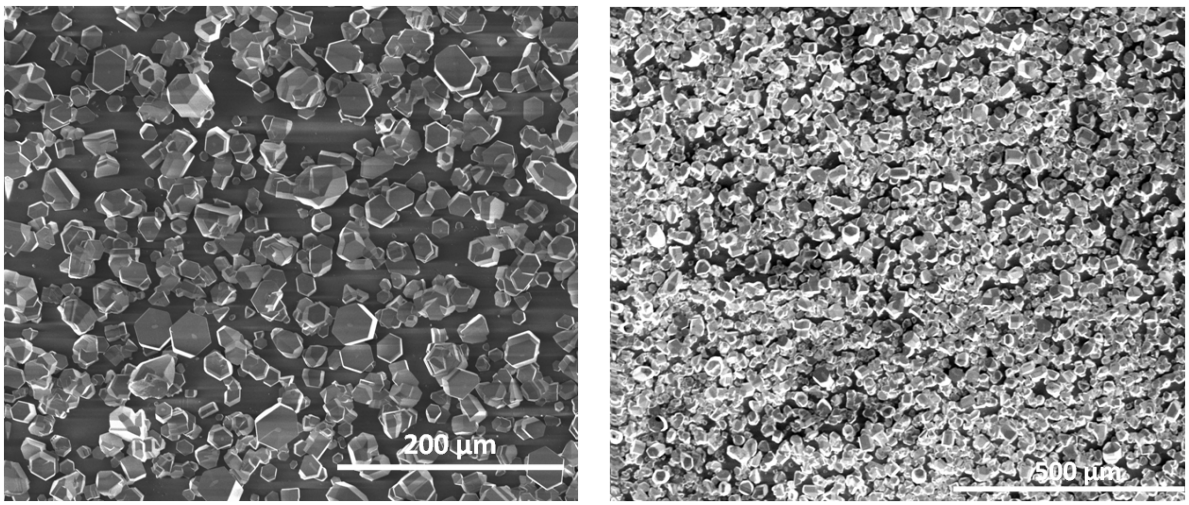

Figure 3.41: Bird eye's view SEM image of GaN islands grown on sapphire substrate at two different magnifications

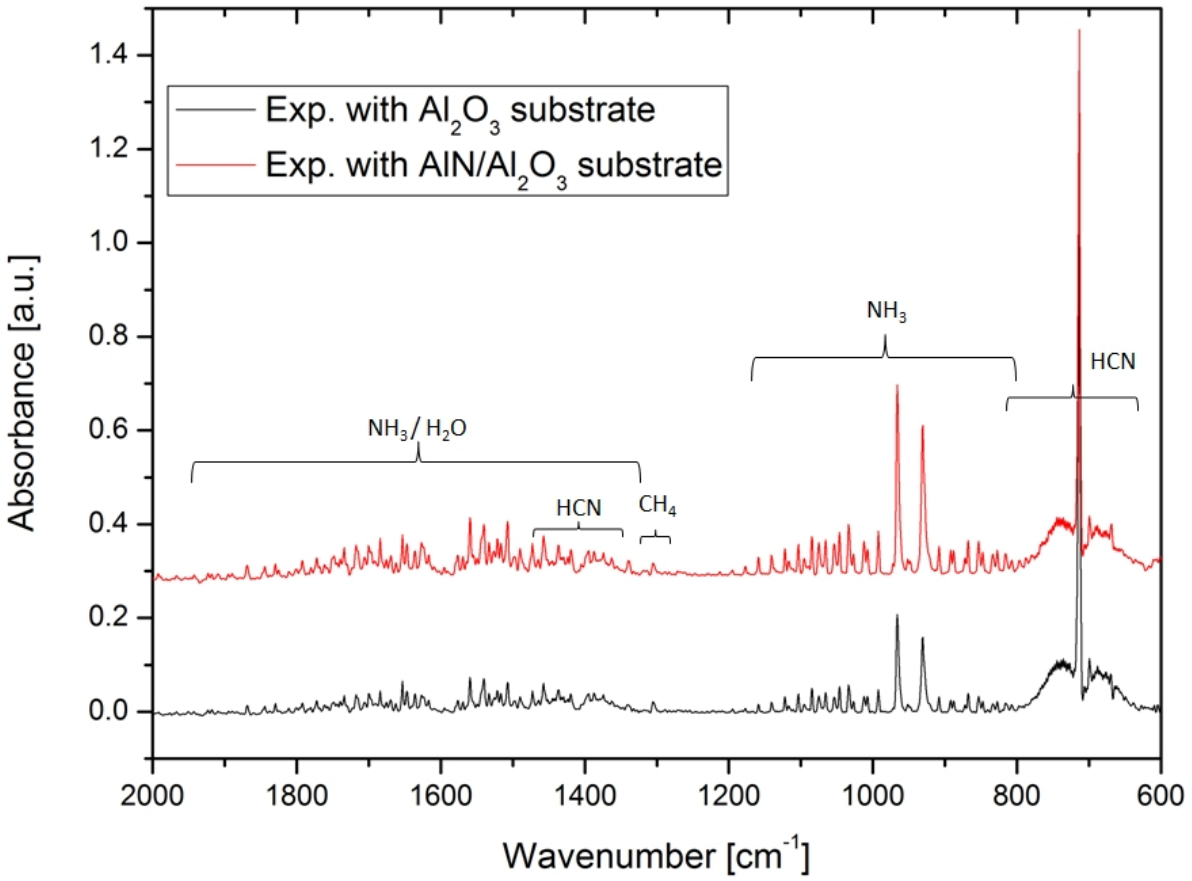

Figure 3.42: FTIR spectra collected during GaN growth on Al_2O_3 substrate(black) and on AlN/Al_2O_3 template (red)

methane were detected after growth temperature was applied. Due to strong overlap with NH_3, H_2O, and HCN bands and additionally very low signal (below 0.05 $a.u.$) it was impossible to estimate its content during the process. The dominant intensity was observed for HCN band. It can be estimated, that approx. $\sim 0.6\%$ of the gas flow inside the exhaust line consisted of HCN.

In Fig. 3.43 the substrate and a part of the growth cell after another experiment are shown. Different to the previous process, a 2 μm AlN/Al_2O_3 template was used as substrate. Also, the temperature difference between the crucible and seed holder was increased by $10K$ and the growth time was extended to 6 h.

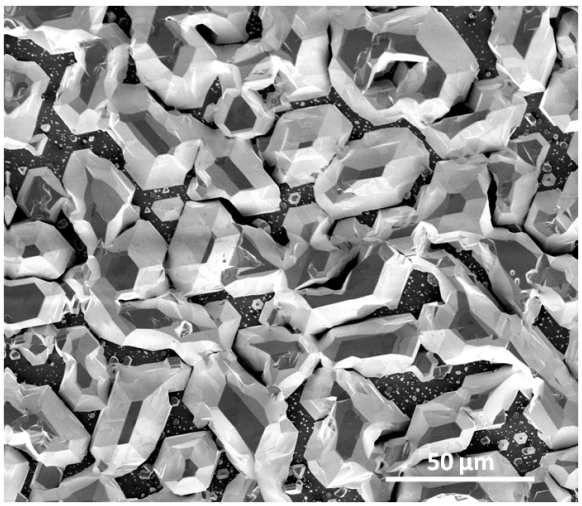

(a) SEM image of GaN islands grown on AlN/Al_2O_3 template

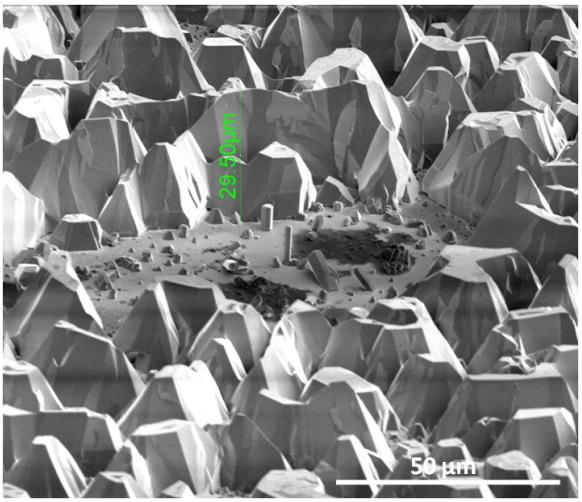

(b) SEM image of GaN islands grown on AlN/Al_2O_3 template (view tilted by 65°)

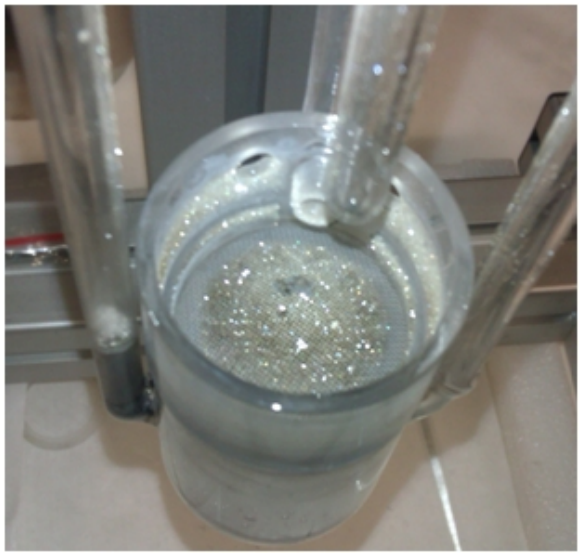

(c) Growth cell with Mo mesh with parasitic grown GaN crystals

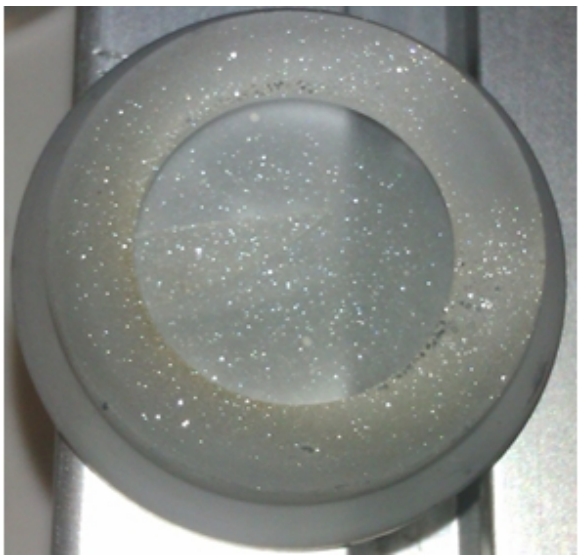

(d) Seed holder with parasitic grown GaN crystals

Figure 3.43: SEM and optical camera images of the sample and growth setup after experiment

The other parameters were the same as in the previously described experiment. The FTIR spectrum presented in Fig. 3.42 shows that the amount of HCN does not differ between both experiments. However, the NH_3 band changed its intensity. The calculations of the integrals for ammonia bands in both processes showed a 35% increase in its

concentration for the process where the AlN/Al_2O_3 template was used.

The SEM investigation showed that during this process also islands were grown, however, in this case most of the islands kept growing in the c-direction. Many islands coalesce, as it is shown in Fig. 3.43a. The height of the islands as indicated in Fig. 3.43b is approx. 29 μm. The size of the islands was not homogeneous and varied from 10 μm or below up to more than 50 μm.

In Fig. 3.43c, self nucleated GaN on quartz and the Mo-diaphragm mesh are shown. It is important to notice, that no deposition was observed on the Ga side (bottom) of diaphragm. It confirms, that the NH_3 from the ring shower is effectively decomposed on the diaphragm and diaphragm-Mo mesh. Therefore, the reactive nitrogen had no access to the bottom of the growth cell. The sizes of the self-nucleated crystals were highest on the Mo meshes and exceed 1 mm in height. On the seed holder (Fig. 3.43d) self-nucleated crystals were significantly smaller, which lead to the conclusion that significant amount of $GaCN$ reacted with NH_3 directly above the mesh and only a small fraction of $GaCN$ reached the seed holder.

Next, growth of GaN was performed on GaN/Al_2O_3 templates. In this experiment

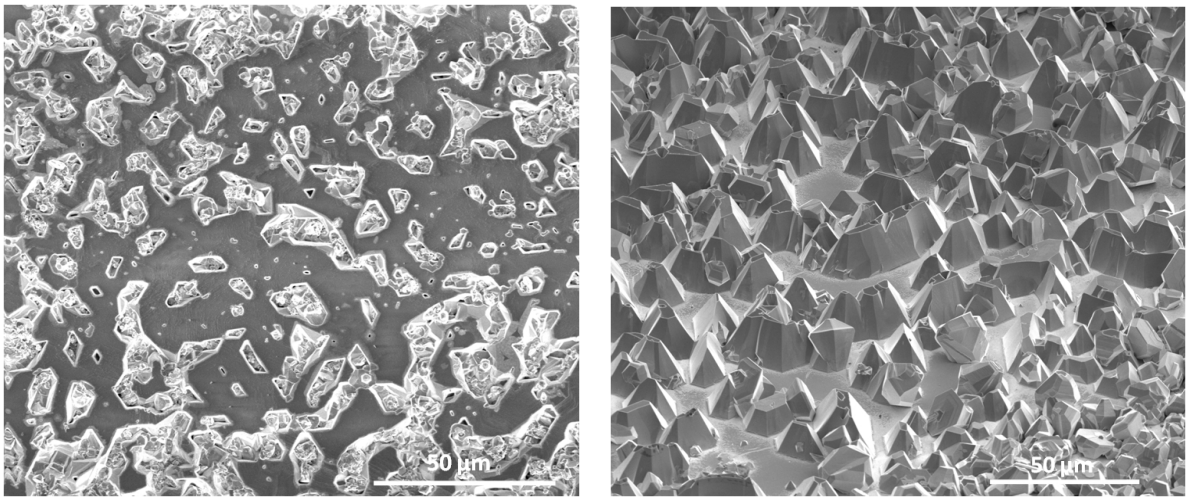

(a) SEM image of GaN islands grown on GaN/Al_2O_3 template

(b) SEM images of GaN islands grown on GaN/Al_2O_3 template (view tilted by 52°)

Figure 3.44: SEM image of GaN islands grown on GaN/Al_2O_3 template

HCN was synthesized in the bubbler line. Therefore, the Ga was bubbled with both the HCN and N_2. The Gas flows in lines were set as follows:

NH_3 - 10 $sccm$ into the bubbler and 20 $sccm$ into the ring shower
CH_4 - 0.7 $sccm$ into the bubbler
N_2 - 150 $sccm$ into the bubbler and 200 $sccm$ in the transport line

The growth time was 4 h. Also temperature was changed to 990°C on the seed holder and 1100°C on the Ga crucible.

The SEM images of the GaN grown on the GaN/Al_2O_3 template are presented in Fig. 3.44. Similar to previous experiments also islands grew. The height of islands is approx. 30 μm. The coalescence was even more advanced in comparison to previously presented results. The coalescence of few islands is shown in Fig. 3.44a. In some areas the coalesced area exceed 50 μm in length.

3.3.7 Discussion

Problems with coalescence in all cases presented above were caused by very low Ga transport, the substrate preparation and its structural quality.

The main limitation of the Ga transport is very low HCN flow, not exceeding 1 $sccm$. In the reactor presented above it was not possible to synthesize more HCN due to the limited Pt catalyst surface. The experiments with high constant flow of NH_3 - 50 $sccm$ were conducted to determine the yield of HCN synthesis. It was measured by FTIR that increasing CH_4 flow above 5 $sccm$ does not increase the concentration of HCN in the exhaust gas line. Moreover changing the flow of CH_4 from 2.8 to 5 $sccm$ increases the yield of HCN only by 25%. Therefore, there was not sufficient amount of $GaCN$ for switching to 2D growth mode (layer by layer). Additional problem with above described reactor construction is its sensitivity to any change in the process parameters such as: pressure, temperature, gradient, carrier gas flows. Any change between the processes influences the HCN synthesis rate, and therefore influences also the Ga transport.

To increase effectivity of the $GaCN$ formation the Ga was bubbled with HCN. The idea of bubbling gives three advantages. First is that more HCN is forced to interact with the liquid Ga. In comparison with supplying it above the surface, where significant part would flow immediately downstream, away from the Ga surface, without interacting with Ga. The second important aspect is to decrease the surface tension which is relatively high approx. 670 mJm^{-2} [114]. The third advantage of bubbling Ga is that a GaN crust commonly formed on the liquid surface is destroyed during bubbling. High Ga surface tension required high gas flow of approx. 100 $sccm$ for bubbling. Depending on the temperature different flow rates were required. Pre-experiments showed, that a gas flow of 500 $sccm$ (maximum flow of attached N_2 MFC) was not able to bubble cold ($\sim 30°C$) Ga, it rather form a path between melt and wall and allows the gas to escape around the melt. Starting at $\sim 700°C$ the bubbling was effective at 100 $sccm$ gas flows.

The substrates are the second issue. It is well known in the classical $HVPE$ that substrates are crucial for the GaN growth. Their quality determines that of the grown layers. This is also true for the surface preparation. There is a necessity of complicated substrate preparation for GaN growth. As it was not the subject of this study the substrate issue remains unstudied. The basic cleaning procedure of substrates used in this work was limited to a removal of organic impurities and bigger particles from the surface of templates, by cleaning in aceton, isopropanol at ultrasound washer and drying in the flow of $4.5N$ N_2. However, in frame of this work the author had no access to a clean room, the cleaning from the dust particles was not sufficient. Moreover, because the first approaches were to prove if the crystal could be grown in the newly designed reactor and to establish the growth conditions, there was no reason for using expensive epi-ready cleaned and polished GaN or AlN templates or even more expensive bulk GaN substrates.

Nevertheless, the principle of the growth was proved to work. It was possible to grow islands up to approx. ~ 30 μm height and up to 50×50 μm^2 in size.

The problem with amount of HCN and its sensitivity to changes between the processes motivated to redesign the concept of HCN synthesis. A new oven was constructed to

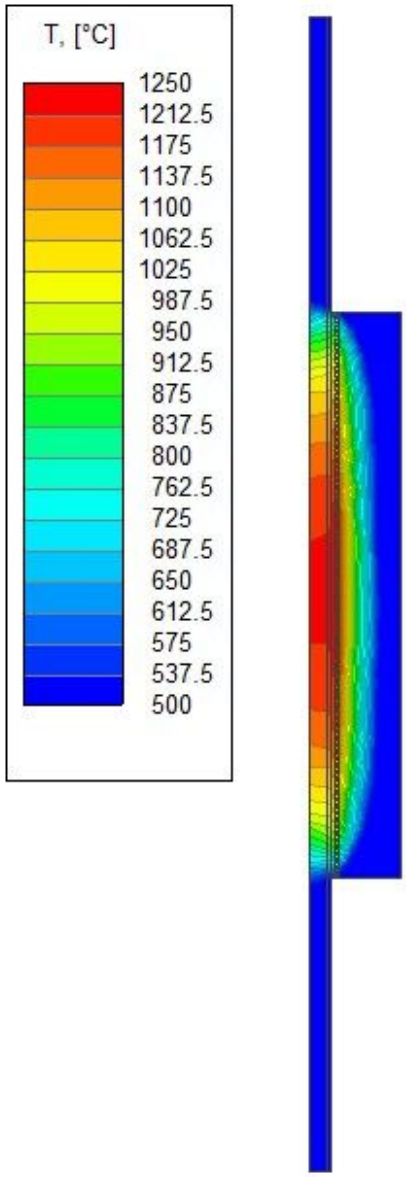

Figure 3.45: Temperature distribution inside the HCN synthesis furnace

improve the efficiency of HCN synthesis. It is based also on the Degussa process, but the Pt mesh was exchanged with Pt-coated Al_2O_3 pellets, whose surface is in the range of $150 - 200\ m^2/g$ which is two order of magnitude more than for the Pt mesh. The inner tube of the furnace was made of a non-porous alumina. The heat source is a resistive heater made of A-1 Kanthal wire. The reactor scheme together with temperature

distribution is presented in Fig. 3.45. The zone of temperature exceeding 1100°C is longer than 300 mm. The volume is 500 times larger than the bubbler line. It is filled with 200 g Pt-coated Al_2O_3 pellets. The operating temperature is up to 1300°C. Due to those parameters HCN flow through is increased by at least one order of magnitude. The outlet of the new HCN synthesis furnace can be connected directly to either the bubbler or transport line.

In this way the GaN growth process and the HCN synthesis are separated and do not influence each other anymore.

Due to significantly increased volume of toxic HCN the safety measures have to be improved to make this approach secure. Additional gas detectors were installed above the reactor and the exhaust gas burning furnace. A two level alarm was pre-set. First level - warning alarm activate at the HCN concentration of 5 ppm at any detector. The second level is activated at 10 ppm. The second level alarm is integrated with NH_3 bottle valve system. The flow of NH_3 is automatically switched off while the alarm goes on. Additionally, the safety measures required to ensure special first aid kit containing antidots like amyl nitrite and sodium nitrite in form of injections.

Due to significant delays concerning the start of operation associated with the complicated safety procedure no growth experiments were conducted so far with the newly designed HCN oven.

4 Summary and Outlook

Many aspects of GaN crystal growth by PHVPE have been elucidated. The PHVPE process has been developed towards improved control over reaction paths and growth rate, beginning with first experiments conducted in the reactor made of graphite, followed by one with pBN coated graphite and finished with the newly designed graphite free reactor.

The proposed growth model based on thermodynamical calculations was reviewed, and conclusions from the observed crystal and reactor parts after experiment were drawn. To support the theoretical consideration a gas analyzing system based on FTIR spectrometer has been developed. The waste gas measurements in the graphite-based reactor were done ex-situ. The results have proved that HCN is formed at high rate, due to the reaction of NH_3 with uncovered carbon parts, and confirmed the reaction path proposed by Jacobs et al.. In this reactor construction, high growth rates up to 60 $\mu m/h$ had been demonstrated. However, the crystals suffer from high V-pits concentration caused by carbon particles stemming from carbon parts attacked by hot NH_3.

Therefore in the next approach pBN-coated graphite parts were used in the reactor. It was measured, that the HCN concentration inside the reactor drops dramatically. As a consequence, the growth rate was one order of magnitude lower than for the previous setup. Nevertheless, the surface morphology of the layer improved and thick layers up to 300 μm have been grown on GaN/Al_2O_3 templates.

Apart from variations in growth parameters between the different experimental runs, the growth on $\beta - Ga_2O_3$ substrate has been studied. Hexagonal GaN was grown directly on $\beta - Ga_2O_3$ (100) substrate with employment of an in-situ low-temperature nitridation

step. Self separation of the bulk GaN from the $Ga-oxide$ substrate at room temperature was facilitated by growth on cleavage planes of $\beta - Ga_2O_3$ as well as by the limited connection of the grown layer to the substrate. The growth consisted of two modes of Ga transport, one by $Ga-oxide$ and the second one by $Ga-cyanide$. By using Ga_2O as a transport agent, a low quality GaN layer was grown. In the second step with $GaCN$ as transport agent, the quality of GaN crystal was significantly improved. Estimated by TEM and XRD dislocation density of GaN, grown on single crystalline Czochralski grown $\beta - Ga_2O_3$ substrates, was in the range of $4 \times 10^9\ cm^{-2}$. The lattice mismatch has been calculated based on the TEM measurements as 4.7% for $< 1\bar{1}00 >$ and -5.05% for $< 11\bar{2}0 >$.

In order to increase the reproducibility in the PHVPE process, a new graphite-free reactor made of quartz-glass has been developed. The construction is vertical with 2-zone resistive heating. The temperature gradient and gas flows have been simulated in HEpiGaNS software and compared to the measured values. Results of temperature simulations were in good agreement with experimental data.

The gaseous source of carbon has been used for synthesis of HCN in classical Degussa process on Pt catalyst. Liquid Ga source was bubbled with HCN gas at temperature range of $1000 - 1200°C$. It prevents surface crust formation on the liquid surface, and increases the yield of volatile HCN to $GaCN$ conversion.

To get insights into the reactions during the process, an in-situ measurement setup based on FTIR was developed. It was possible to measure the gas content inside the exhaust gas line without any process interruption. The established measurement allowed to identify the reaction products and to calculate their concentrations.

By using in-situ gas measurement it has been found, that HCN synthesis has to be conducted under excess of NH_3 ($NH_3 : CH_4$; $(7 - 10) : 1$). With lower NH_3 concentration C_2H_2 was formed, and the reactor inner parts and wall were covered with carbon film and the growth rate drastically decreased.

The preliminary experiments in the new setup showed promising results. GaN crystals have been grown on various substrates, starting with pure sapphire, where only randomly

oriented island have been grown, nevertheless the islands sizes were approx. 30 μm after 5 h growth process. The growth experiments on GaN/Al_2O_3 and AlN/Al_2O_3 templates showed c-oriented, partially coalesced islands with heights up to 30 μm and sizes up to 50 μm.

The insufficient in-situ production of HCN has been the crucial point in low growth rate. To increase it a new concept has been developed. The Pt mesh was exchanged with Pt covered Al_2O_3 pellets. This increased the catalyst surface dramatically, and ensures a sufficient HCN source for higher growth rate. Nevertheless, the concept has not been tried yet due to the complicated safety measures.

The goal of this work, to demonstrate that crystal growth with cyanide transport is possible, has been achieved. The next challenge is the process optimization to grow carbon doped semi-insulating layers for physical characterization by our project partner at TU Berlin.

The more general concept of the PHVPE is to facilitate the growth of GaN crystals, doped either by carbon contained in the transport agent or to facilitate the doping with other substances, which are hard to use in case of classical HVPE due to highly reactive HCl used for this process.

Bibliography

[1] E. F. Schubert, "Light-Emmiting Diodes," in *Cambridge University Press*, 2006.

[2] S. A. Eliza and A. K. Dutta, "Ultra-high sensitivity gas sensors based on GaN HEMT structures," in *Electrical and Computer Engineering (ICECE)*, 2010, p. 431.

[3] S. Koide, H. Takahashi, A. Abderrahmane, I. Shibasaki, and A. Sandhu, "High Temperature Hall sensors using AlGaN / GaN HEMT Structures," *Journal of Physics*, vol. 352, p. 012009, 2012.

[4] M. Bockowski and Z. Sitar, "Hybrid approach yields the best GaN crystals and wafers," *Compound Semiconductors*, no. June, p. 22, 2014.

[5] C. Skierbiszewski, P. Perlin, I. Grzegory, Z. R. Wasilewski, M. Siekacz, A. Feduniewicz, P. Wisniewski, J. Borysiuk, P. Prystawko, G. Kamler, T. Suski, and S. Porowski, "High power blue violet InGaN laser diodes grown on bulk GaN substrates by plasma-assisted molecular beam epitaxy," *Semicond. Sci. Technol.*, vol. 20, p. 809, 2005.

[6] C. Skierbiszewski, P. Winiewski, M. Siekacz, P. Perlin, A. Feduniewicz-Zmuda, G. Nowak, I. Grzegory, M. Leszczynski, and S. Porowski, "60 mW continuous-wave operation of InGaN laser diodes made by plasma-assisted molecular-beam epitaxy," *Appl. Phys. Lett.*, vol. 88, p. 221108, 2006.

[7] W. J. Moore, J. A. Freitas, G. C. B. Braga, R. J. Molnar, S. K. Lee, K. Y. Lee, and I. J. Song, "Identification of Si and O donors in hydride-vapor-phase epitaxial GaN," *Appl. Phys. Lett.*, vol. 79, p. 2570, 2001.

[8] H. Tang, J. B. Webb, J. A. Bardwell, S. Raymond, J. Salzman, and C. Uzan-Saguy, "Properties of carbon-doped GaN," *Appl. Phys. Lett.*, vol. 78, p. 757, 2001.

[9] M. R. Ramdani, M. Chmielowska, Y. Cordier, S. Chenot, and F. Semond, "Effect of carbon doping on crystal quality, electrical isolation and electron trapping in GaN based structures grown silicon substrates," *Solid State Electronics*, vol. 75, p. 86, 2012.

[10] A. Armstrong, C. Poblenz, D. Green, U. Mishra, J. Speck, and S. Ringel, "Impact of substrate temperature on the incorporation of carbon-related defects and mechanism for semi-insulating behavior in GaN grown by molecular beam epitaxy Impact of substrate temperature on the incorporation of carbon-related defects and mechanism f," *Appl. Phys. Lett.*, vol. 88, p. 86, 2006.

[11] O. Lopatiuk, A. Osinsky, A. Dabiran, K. Gartsman, I. Feldman, and L. Chernyak, "Electron trapping effects in C- and Fe-doped GaN and AlGaN," *Solid-State Electronics*, vol. 49, p. 1662, 2005.

[12] M. Rudzinski, V. Desmaris, P. A. V. Hal, J. L. Weyher, P. R. Hageman, K. Dynefors, T. C. Rodle, H. F. F. Jos, H. Zirath, and P. K. Larsen, "Growth of Fe doped semi-insulating GaN on sapphire and 4H-SiC by MOCVD," *Physica Status Solidi (C)*, vol. 3, p. 2231, 2006.

[13] S. Strite and H. Morko, "Critical review GaN, AIN, and InN: A review," vol. 10, p. 1237, 1992.

[14] I. Grzegory, "High pressure growth of bulk GaN from solutions in Gallium," *J. Phys.: Condens. Matter*, vol. 13, p. 6875, 2001.

[15] J. Karpinski, J. Jun, and S. Porowski, "Equlibrium pressure of N2 over GaN and high pressure solution growth of GaN," *Journal of Crystal Growth*, vol. 66, p. 1, 1984.

[16] W. Utsumi, H. Saitoh, H. Kaneko, T. Watanuki, K. Aoki, and O. Shimomura, "Congruent melting of gallium nitride at 6 GPa and its application to single-crystal growth," *Nature materials*, vol. 2, p. 735, Nov. 2003.

[17] Y. V. Melnik, A. E. Nikolaev, S. I. Stepanov, A. S. Zubrilov, I. P. Nikitina, K. V. Vassilevski, D. V. Tsvetkov, A. I. Babanin, Y. G. Musikhin, V. V. Tretyakov, and V. A. Dmitriev, "AIN/GaN and AIGaN/GaN Heterostructures Grown by HVPE on SiC Substrates," *MRS Online Proceedings Library*, vol. 482, p. 245, 1997.

[18] O. Voznyy and J. J. Dubowski, "Structure , Bonding Nature , and Binding Energy of Alkanethiolate on As-Rich GaAs (001) Surface: A Density Functional Theory Study," *The journal of physical chemistry B*, vol. 110, p. 23619, 2006.

[19] R. R. Reddy, T. V. R. Rao, and R. Viswanath, "Potential energy curves and dissociation energies of NbO, SiC, CP, PH+, SiF+, and NH+," *Astrophysics and Space Science*, vol. 198, p. 29, 1992.

[20] I. Barin, "Thermodynamic Functions and Relations," in *Thermochemical Data of Pure Substances*. Wiley-VCH Verlag GmbH, 2008.

[21] Bernard Gil, *III-Nitride Semiconductors and their Modern Devices*, 1st ed., B. Gil, Ed. Oxford: Oxford University Press, 2013.

[22] "Precision Micro-Optics sapphire datasheet." [Online]. Available: http://www.pmoptics.com/sapphire.html

[23] M. E. Lin, G. Xue, G. L. Zhou, J. E. Greene, and H. Morkoc, "p-type zincblende GaN on GaAs substrates," *Appl. Phys. Lett.*, vol. 63, p. 932, 1993.

[24] Y. Xie, Y. Qian, S. Zhang, W. Wang, X. Liu, and Y. Zhang, "Coexistence of wurtzite GaN with zinc blende and rocksalt studied by xray power diffraction and high resolution transmission electron microscopy," *Appl. Phys. Lett.*, vol. 69, p. 334, 1996.

[25] L. T. Romano and T. H. Myers, "The influence of inversion domains on surface morphology in GaN grown by molecular beam epitaxy," *Appl. Phys. Lett.*, vol. 71, p. 3486, 1997.

[26] H. Y. Shin, S. K. Kwon, Y. I. Chang, M. J. Cho, and K. H. Park, "Formation Characteristic of Inversion Domains in P-GaN and P-AlGaN Layers By Using TEM Observation," *Journal of Korean Physical Society*, vol. 53, p. 3399, 2008.

[27] J. E. Northrup and J. Neugebauer, "Strong affinity of hydrogen for the GaN (000-1) surface: Implications for molecular beam epitaxy and metalorganic chemical vapor deposition," *Appl. Phys. Lett.*, vol. 85, p. 3429, 2004.

[28] S. F. Li, S. Fuendling, X. Wang, S. Merzsch, M. A. M. Al-Suleiman, J. D. Wei, H. H. Wehmann, and A. Waag, "Polarity and Its Influence on Growth Mechanism during MOVPE Growth of GaN Sub-micrometer Rods," *Crystal Growth Design*, vol. 11, p. 1573, 2011.

[29] M. Bockowski, "Review : Bulk growth of gallium nitride : challenges and difficulties," *Cryst. Res.Technol.*, vol. 42, p. 1162, 2007.

[30] I. Grzegory and S. Porowski, "GaN substrates for molecular beam epitaxy growth of homoepitaxial structures," *Thin Solid Films*, vol. 367, p. 281, 2000.

[31] M. Bockowski, I. Grzegory, B. Lucznik, T. Sochacki, G. Nowak, B. Sadovyi, P. Strak, G. Kamler, E. Litwin-Staszewska, and S. Porowski, "Multi feed seed (MFS) high pressure crystallization of 1-2 in GaN," *Journal of Crystal Growth*, vol. 350, p. 5, 2012.

[32] M. Bockowski, I. Grzegory, B. Lucznik, T. Sochacki, M. Krysko, G. Kamler, and S. Porowski, "High nitrogen pressure solution (HNPS) growth of GaN on 2 inch free standing GaN substrates," *Science China Technological Sciences*, vol. 54, p. 42, Dec. 2011.

[33] F. Kawamura, M. Morishita, M. Tanpo, M. Imade, M. Yoshimura, Y. Kitaoka, Y. Mori, and T. Sasaki, "Effect of carbon additive on increases in the growth rate of 2in GaN single crystals in the Na flux method," *Journal of Crystal Growth*, vol. 310, p. 3946, Aug. 2008.

[34] F. Kawamura, M. Morishita, K. Omae, M. Yoshimura, Y. Mori, and T. Sasaki, "The effects of Na and some additives on nitrogen dissolution in the Ga-Na system : A growth mechanism of GaN in the Na flux method," *Journal of Material Science*, vol. 16, p. 29, 2005.

[35] Y. Mori, M. Imade, M. Maruyama, and M. Yoshimura, "Growth of GaN Crystals by Na Flux Method," *Journal of Solid State Science and Technology*, vol. 2, p. 3068, 2013.

[36] Y. Mori, M. Imade, K. Murakami, H. Takazawa, H. Imabayashi, Y. Todoroki, K. Kitamoto, M. Maruyama, M. Yoshimura, Y. Kitaoka, and T. Sasaki, "Growth of bulk GaN crystal by Na flux method under various conditions," *Journal of Crystal Growth*, vol. 350, p. 72, 2012.

[37] M. Imade, Y. Hirabayashi, N. Miyoshi, M. Yoshimura, Y. Kitaoka, T. Sasaki, and Y. Mori, "Control of Growth Facets and Dislocation Propagation Behavior in the Na-Flux Growth of GaN," *Crystal Growth Design*, vol. 11, p. 2346, 2011.

[38] S. Krukowski, P. Kempisty, and P. Strk, "Review : GaN growth by ammonia based methods density functional theory study," *Cryst. Res.Technol.*, vol. 44, p. 1038, 2009.

[39] D. Ehrentraut, Y. Kagamitani, C. Yokoyama, and T. Fukuda, "Physico-chemical features of the acid ammonothermal growth of GaN," *Journal of Crystal Growth*, vol. 310, p. 891, 2008.

[40] R. Dwilinski, R. Doradzinski, J. Garczynski, L. Sierzputowski, A. Puchalski, Y. Kanbara, K. Yagi, H. Minakuchi, and H. Hayashi, "Bulk ammonothermal GaN," *Journal of Crystal Growth*, vol. 311, p. 3015, May 2009.

[41] D. Ehrentraut, E. Meissner, and M. Bockowski, *Technology of Gallium Nitride Crystal Growth*. New York: Springer, 2010.

[42] R. Dwilinski, R. Doradzinski, J. Garczynski, L. Sierzputowski, R. Kucharski, M. Zajac, M. Rudzinski, R. Kudrawiec, W. Strupinski, and J. Misiewicz, "Ammonothermal GaN substrates: Growth accomplishments and applications," *physica status solidi (a)*, vol. 208, p. 1489, 2011.

[43] S. W. Kaun, M. H. Wong, U. K. Mishra, and J. S. Speck, "Molecular beam epitaxy for high-performance Ga-face GaN electron devices," *Semicond. Sci. Technol.*, vol. 28, p. 1, 2013.

[44] "HVPE growth Setup." [Online]. Available: http://www.str-soft.com/products/cvdsim/HVPE/

[45] M. Amilusik, T. Sochacki, B. Lucznik, M. Bockowski, B. Sadovyi, A. Presz, I. Dziecielewski, and I. Grzegory, "Analysis of self-lift-off process during HVPE growth of GaN on MOCVD-GaN/sapphire substrates with photolitographically patterned Ti mask," *Journal of Crystal Growth*, vol. 380, p. 99, 2013.

[46] T. Sochacki, Z. Bryan, M. Amilusik, R. Collazo, B. Lucznik, J. L. Weyher, G. Nowak, B. Sadovyi, G. Kamler, R. Kucharski, M. Zajac, R. Doradzinski, R. Dwilinski, I. Grzegory, M. Bockowski, and Z. Sitar, "Preparation of Free-Standing GaN Substrates from Thick GaN Layers Crystallized by Hydride Vapor Phase Epitaxy on Ammonothermally Grown GaN Seeds," *Appl. Phys. Express*, vol. 6, p. 075504, 2013.

[47] E. Richter, T. Stoica, U. Zeimer, C. Netzel, M. Weyers, and G. Traenkle, "Si Doping of GaN in Hydride Vapor-Phase Epitaxy," *Journal of Electronic Materials*, vol. 42, p. 8, 2013.

[48] E. Richter, M. Grunder, C. Netzel, M. Weyers, and G. Traenkle, "Growth of GaN boules via vertical HVPE," *Journal of Crystal Growth*, vol. 350, p. 89, Jul. 2012.

[49] T. Sochacki, Z. Bryan, M. Amilusik, M. Bobea, M. Fijalkowski, I. Bryan, B. Lucznik, R. Collazo, J. L. Weyher, R. Kucharski, I. Grzegory, M. Bockowski, and Z. Sitar, "HVPE-GaN grown on MOCVD-GaN/sapphire template and ammonothermal GaN seeds: Comparison of structural, optical, and electrical properties," *Journal of Crystal Growth*, vol. 394, p. 55, 2014.

[50] N. Liu, J. Wu, W. Li, R. Luo, Y. Tong, and G. Zhang, "Highly uniform growth of 2-inch GaN wafers with a multi-wafer HVPE system," *Journal of Crystal Growth*, vol. 388, p. 132, 2014.

[51] L. Hui, "Mass transport analysis of a showerhead MOCVD reactor," *Journal of Semiconductors*, vol. 32, p. 033006, Mar. 2011.

[52] M. Sumiya and S. Fuke, "Review of polarity determination and control of GaN," *J. Nitride Semicond. Res.*, vol. 9, p. 1, 2004.

[53] C. Y. Huang, P. J. Hsieh, I. C. Chen, W. C. K. Ke, P. F. Yang, and S. R. Jian, "Nanoindentation of Mg-doped AlGaN thin films," *Journal of alloys and compounds*, vol. 593, p. 220, 2014.

[54] D. D. Koleske, S. R. Lee, M. H. Crawford, K. C. Cross, M. E. Coltrin, and J. M. Kempisty, "Connection between GaN and InGaN growth mechanisms and surface morphology," *Journal of Crystal Growth*, vol. 391, p. 85, 2014.

[55] A. Sztein, J. E. Bowers, S. P. Denbaars, and S. Nakamura, "Thermoelectric properties of lattice matched InAlN on semi-insulating GaN templates," *Journal of Applied Physics*, vol. 112, p. 083716, 2012.

[56] B. Fu, N. Liu, N. Zhang, Z. Si, X. Wei, X. Wang, H. Lu, Z. Liu, T. Wei, X. Yi, J. Li, and J. Wang, "The Effect of Growth Pressure and Growth Rate on the Properties of Mg-Doped GaN," *Journal of Electronic Materials*, vol. 43, p. 1244, 2014.

[57] J. Zhang, W. Tian, F. Wu, Q. Wan, Z. Wang, J. Zhang, Y. Li, J. Dai, Y. Fang, Z. Wu, C. Chen, J. Xu, and X. Li, "The effects of substrate nitridation on the growth of nonpolar a-plane GaN on r-plane sapphire by metalorganic chemical vapor deposition," *Applied Surface Science*, vol. 307, p. 525, 2014.

[58] L. Liu and J. H. Edgar, "Substrates for gallium nitride epitaxy," *Materials Science and Engineering: R: Reports*, vol. 37, p. 61, 2002.

[59] Z. Lin, J. Zhang, R. Cao, W. Ha, S. Zhang, X. Chen, J. Yan, S. Xu, Y. Zhao, L. Li, and Y. Hao, "Effect of growth temperature on the impurity incorporation and material properties of N-polar GaN fi lms grown by metal-organic chemical vapor deposition," *Journal of Crystal Growth*, vol. 384, p. 96, 2013.

[60] I. Akasaki, H. Amano, Y. Koide, K. Hiramatsu, and N. Sawaki, "Effects of AlN buffer layer on crystallographic structure and electrical and optical properties of GaN and Ga(1-x)Al(x)N (0¡x¡0.4) films grown on sapphire substrate by MOVPE," *Journal of Crystal Growth*, vol. 98, p. 209, 1989.

[61] "FEI Company product Data." [Online]. Available: http://www.nanolab.ucla.edu/pdf/Nova600spec.pdf

[62] K. Muszka, "Wplyw rozdrobnienia struktury na mechanizmy umocnienia stali niskowglowych odksztacanych plastycznie," Ph.D. dissertation, AGH Krakow, 2008.

[63] R. W. Kelsall, I. W. Hamley, and M. Geoghegan, *Nanotechnologie*. Wydawnictwo Naukowe PWN, 2012.

[64] R. F. Egerton, *Physical Principles of Electron Microscopy. An Introduction to TEM, SEM, and AEM.* Springer, 2008.

[65] G. Thomas and M. J. Gorgine, *Transmission Electron Microscopy of Materials.* John Wiley and Sons, 1979.

[66] B. Fultz and J. M. Howe, *Transmission Electron Microscopy and Difractometry of Materials*, iii ed. Springer, 2008.

[67] "Bruker Vector 22 FT-IR Spectrometer manual."

[68] P. Griffiths and J. Haseth, *Fourier Transform Infrared Spectrometry.* A JOHN WILEY & SONS, INC, 2007.

[69] B. C. Smith, *Fundamentals of Fourier Transform Infrared Spectroscopy*, CRC Press, Boca Raton, 2010.

[70] L. Pugh and K. Rao, "Intensities from Infrared Spectra," in *Molecular Spectroscopy Modern Research v. II.* New York: Academic press, inc., 1976, ch. 4.

[71] M. Smith, C. Rinsland, B. Fridovich, and K. Rao, "Intensities and Collision Broadening Parameters from Infrared Spectra," in *Molecular Spectroscopy Modern Research v. III.* Orlando: Academic press, inc., 1985.

[72] "Ansyco." [Online]. Available: http://www.ansyco.de/CMS/frontend/index.php?idcatside=124

[73] "HITRAN2008." [Online]. Available: http://www.cfa.harvard.edu/hitran/facts.html

[74] G. Guelachvili and N. Rao, *Handbook of infrared Standards.* Orlando: Academic press, inc., 1986.

[75] H.-J. Rost, D. Siche, D. Gogova, M. Albrecht, K. Jacobs, and R. Fornari, "The role of carbon in transport processes during PVT growth of bulk GaN," *Physica Status Solidi (C)*, vol. 6, p. 1484, Jun. 2009.

[76] K. Jacobs, D. Siche, D. Klimm, H.-J. Rost, and D. Gogova, "Pseudohalide vapour growth of thick GaN layers," *Journal of Crystal Growth*, vol. 312, p. 750, Mar. 2010.

[77] M. Guido and G. Gigli, "Mass spectrometric study of the gaseous gallium monocyanide," *The Journal of Chemical Physics*, vol. 60, p. 721, 1974.

[78] D. Flottmann, D. Forst, and H. Rosswag, *Chemie fuer Ingenieure.* Berlin: Springer, 2004.

[79] P. W. Atkins, *Physikalische Chemie.* Weinheim: VCH Verlagsgesellschaft mbH, 1990.

[80] V. Ban, "Mass Spectrometric Studies of Vapor-Phase Crystal Growth," *J. Electrochem. Soc.*, vol. 119, p. 761, 1972.

[81] S. S. Liu and D. A. Stevenson, "Growth Kinetics and Catalytic Effects in the Vapor Phase Epitaxy of Gallium Nitride," *J. Electrochem. Soc.*, vol. 125, p. 1161, 1978.

[82] Rath, "www.rath-group.com/produkte/vakuumformteile/altraform/."

[83] R. Zwierz, "Plasma Enhanced Growth of GaN Single Crystalline Layers from Vapour Phase," Ph.D. dissertation, BTU Cottbus, 2014.

[84] M. Junaid, P. Sandstrom, J. Palisaitis, V. Darakchieva, C. L. Hsiao, P. O. A. Persson, L. Hultman, and J. Birch, "Stress evolution during growth of GaN (0001)/Al2O3(0001) by reactive dc magnetron sputter epitaxy," *Journal of Physics D: Appl. Phys.*, vol. 47, p. 1, 2014.

[85] A. K. Ozturk, H. Altuntas, S. Corekci, Y. Hongbo, S. Ozcelik, and E. Ozbay, "Strain Stress Analysis of AlGaN/GaN Heterostructures With and Without an AlN Buffer and Interlayer," *An International Journal for Experimental Mechanics*, vol. 47, p. 19, 2011.

[86] B. J. Skromme, H. Zhao, D. Wang, H. S. Kong, M. T. Leonard, G. E. Bulman, and R. J. Molnar, "Strain determination in heteroepitaxial GaN Strain determination in heteroepitaxial GaN," *Appl. Phys. Lett.*, vol. 71, p. 829, 1997.

[87] N. Itoh, J. C. Rhee, T. Kawabata, and S. Koike, "Study of cracking mechanism in GaN/a-A1203 structure," *Journal of Applied Physics*, vol. 58, p. 1828, 1985.

[88] V. P. Kelly, M K and, V. M. Phanse, L. Gorgens, and O. Ambacher, "Large Free-Standing GaN Substrates by Hydride Vapor Phase Epitaxy and Laser-Induced Liftoff," *Jpn. J. Appl. Phys.*, vol. 38, p. L217, 1999.

[89] C. L. Chao, C. H. Chiu, Y. J. Lee, H. C. Kuo, P. C. Liu, J. D. Tsay, and S. J. Cheng, "Freestanding high quality GaN substrate by associated GaN nanorods self-separated hydride vapor-phase epitaxy," *Appl. Phys. Lett.*, vol. 95, p. 051905, 2009.

[90] K. Kachel, M. Korytov, D. Gogova, Z. Galazka, M. Albrecht, R. Zwierz, D. Siche, S. Golka, A. Kwasniewski, M. Schmidbauer, and R. Fornari, "A new approach to free-standing GaN using β-Ga2O3 as a substrate," *CrystEngComm*, vol. 14, p. 8536, 2012.

[91] Z. Galazka, R. Uecker, K. Irmscher, M. Albrecht, D. Klimm, M. Pietsch, M. Brützam, R. Bertram, S. Ganschow, and R. Fornari, "Czochralski growth and characterization of β-Ga2O3 single crystals," *Crystal Research and Technology*, vol. 45, p. 1229, Dec. 2010.

[92] S. Ito, K. Takeda, K. Nagata, H. Aoshima, K. Takehara, M. Iwaya, T. Takeuchi, S. Kamiyama, I. Akasaki, and H. Amano, "Growth of GaN and AlGaN on (100) β-Ga2O3 substrates," *Physica Status Solidi (C)*, vol. 9, p. 519, Mar. 2012.

[93] S. Ohira, N. Suzuki, H. Minami, K. Takahashi, T. Araki, and Y. Nanishi, "Growth of hexagonal GaN films on the nitridated β-Ga2O3 substrates using RF-MBE," *Physica Status Solidi (C)*, vol. 4, p. 2306, Jun. 2007.

[94] T.-Y. Tsai, S.-L. Ou, M.-T. Hung, D.-S. Wuu, and R.-H. Horng, "MOCVD Growth of GaN on Sapphire Using a Ga2O3 Interlayer," *Journal of The Electrochemical Society*, vol. 158, p. H1172, 2011.

[95] K. Shimamura, E. G. Víllora, K. Domen, K. Yui, K. Aoki, and N. Ichinose, "Epitaxial Growth of GaN on (100)β-Ga2O3 Substrates by Metalorganic Vapor Phase Epitaxy," *Japanese Journal of Applied Physics*, vol. 44, p. L7, Jan. 2005.

[96] P. L. Liu, Y. J. Siao, Y. T. Wu, C. H. Wang, and C. S. Chen, "Structural, electronic and energetic properties of GaN[0001]/Ga2O3[100] heterojunctions: A first-principles density functional theory study," *Scripta Materialia*, vol. 65, p. 465, Sep. 2011.

[97] C. G. Dunn and E. F. Kogh, "Comparison of dislocation densities of primary and secondary recrystallization grains of Si-Fe," *Acta Metallurgica*, vol. 5, p. 548, 1957.

[98] C. Y. Nam, D. Tham, and J. E. Fischer, "Effect of the polar surface on GaN nanostructure morphology and growth orientation," *Appl. Phys. Lett.*, vol. 85, p. 5676, 2004.

[99] M. Imade, H. Kishimoto, F. Kawamura, M. Yoshimura, Y. Kitaoka, T. Sasaki, and Y. Mori, "Vapor-phase epitaxy of high-crystallinity GaN films using Ga2O vapor and NH3," *Journal of Crystal Growth*, vol. 312, p. 676, Feb. 2010.

[100] T. S. Zheleva, S. A. Smith, D. B. Thomson, K. J. Linthicum, P. Rajagopal, and R. F. Davis, "Pendeo-Epitaxy : A New Approach for Lateral Growth of Gallium Nitride Films," *Journal of Electronic Materials*, vol. 28, p. L5, 1999.

[101] A. Usui, "Gallium Nitride Crystals Grown by Hydride Vapor Phase Epitaxy with Dislocation Reduction Mechanism," vol. 2, p. N3045, 2013.

[102] K. Motoki, T. Okahisa, N. Matsumoto, M. Matsushima, H. Kimura, H. Kasai, K. Takemoto, K. Uematsu, T. Hirano, M. Nakayama, S. Nakahata, M. Ueno, D. Hara, Y. Kumagai, A. Kokitu, and H. Seki, "Preparation of Large Freestanding GaN Substrates by Hydride Vapor Phase Epitaxy Using GaAs as a Starting Substrate," *Jpn. J. Appl. Phys.*, vol. 40, p. L140, 2001.

[103] A. S. Bodke, D. A. Olschki, and L. D. Schmidt, "Hydrogen addition to the Andrussow process for HCN synthesis," *Applied CatalysisA: General*, vol. 201, p. 13, 2000.

[104] J. Gomez-Diaz and N. Lopez, "Mechanistic Switch between Oxidative (Andrussow) and Nonoxidative (Degussa) Formation of HCN on Pt (111) by Density Functional Theory," *The journal of physical chemistry C*, vol. 115, p. 5667, 2011.

[105] D. A. Hickman, M. Huff, and L. Schmidt, "Alternative catalyst supports for HCN synthesis and NH3 oxidation," *Ind. Eng. Chem. Res.*, vol. 32, p. 809, 1993.

[106] V. A. Kondratenko, G. Weinberg, M. M. Pohl, and D. S. Su, "Mechanistic aspects of the Andrussow process over Pt-Rh gauzes. Effect of gauze morphology and oxygen coverage on primary O2NH3CH4 interactions," *Applied Catalysis A, General*, vol. 381, p. 66, 2010.

[107] V. A. Kondratenko, "Mechanistic aspects of the Andrussow process over Pt-Rh gauzes. Pathways of formation and consumption of HCN," *Applied Catalysis A: General*, vol. 381, p. 74, 2010.

[108] E. McKenna and M. Stoukides, "Modeling of HCN synthesis in a solid electrolyte fuel cell," *Chemical Eng. Science*, vol. 47, p. 2951, 1992.

[109] D. Hasenberg and L. D. Schmidt, "HCN synthesis from CH4 and NH3 on clean Rh," *Journal of Catalysis*, vol. 91, p. 116, 1985.

[110] D. Hasenberg and L. Schmidt, "HCN synthesis from CH4 and NH3 on platinum," *Journal of Catalysis*, vol. 97, p. 156, 1986.

[111] M. Diefenbach, M. Bronstrup, M. Aschi, D. Schroder, and H. Schwarz, "HCN Synthesis from Methane and Ammonia : Mechanisms of Pt + -Mediated C-N Coupling," *J. Am. Chem. Soc.*, vol. 121, p. 10614, 1999.

[112] B. Lorenzut, T. Montini, M. Bevilacqua, and P. Fornasiero, "FeMo-based catalysts for H2 production by NH3 decomposition," *Applied Catalysis B, Environmental*, vol. 125, p. 409, 2012.

[113] T. Aruga, K. Tateno, K. Fukui, and Y. Iwasawa, "Restraint of NH 3 dissociation on oxygen-modified Mo(112)," *Surface Science*, vol. 324, p. 17, 1995.

[114] S. C. Hardy, "The surface tension of liquid gallium," *Journal of Crystal Growth*, vol. 71, p. 602, 1985.

List of Figures

List of Abbreviations

2DEG	two dimensional electron gas
a,b,c,m,r	crystal planes
AFM	atomic force microscopy
AT	ammonothermal solution growth
BF	bright-field
pBN	pyrolytycal boron nitride
CCD	charge coupled device
CN	cyanide
CZ	Czochralski
EBSD	electron backscatter diffraction
EDX	energy-dispersive X-ray spectroscopy
ELO	epitaxial lateral overgrowth
EPDM	ethylene propylene diene monomer
FT	Fourier transformation
FTIR	Fourier transform infrared
FWHM	full width at half maximum
HEMT	high electron mobility transistor
HNPS	high nitrogen pressure solution
HP	high power
HRTEM	high resolution transmission electron microscopy
HR-XRD	high resolution x-ray diffraction
HVPE	halide vapor phase epitaxy

IR	infrared
LD	laser diode
LED	light-emitting diode
LPE	liquid phase epitaxy
MBE	molecular beam epitaxy
MCT	mercury-cadmium-telluride
MFC	mass flow controllers
MMIC	monolithic microwave integrated circuit
MOCVD	metal organic chemical vapour deposition
MOVPE	metalorganic vapor phase epitaxy
PAMBE	plasma assisted molecular beam epitaxy
PHVPE	pseudo-halide vapor phase epitaxy
rms	root mean square
SAED	selected area electron diffraction
SE	secondary electron
SEM	scanning electron microscopy
SI	semi-isolating
SIMS	secondary ion mass spectrometry
SNR	signal-to-noise ratio
TDD	threading dislocation density
TEM	transmission electron microscope
TMAl	trimetylaluminum
TMG	trimetylgallium
TMI	trimetylindium
XRD	x-ray diffraction

List of Symbols

α	absorption coefficient
ε	molar absorbtivity
δ	optical path difference
λ	wavelength
μ	reduced mass of the atoms
ρ	dislocation density
ν	frequency of light
$\Delta\omega_{0002}$	measured FWHM
ΔG	change of Gibbs free energy
ΔH	change of enthalpy
ΔS	change of entropy
$[A]$, $[B]$	active mass of the reaction substrates
$[C]$, $[D]$	active mass of the reaction products
a, b, y, z	stoichiometric coefficients of the reaction
A	absorbance
b_c	burgers vector component along the c-axis
B	integral of the absorbance over the band
C	concentration
c	speed of light
F	Fourier frequency of the interferogram
G	total free energy

I	intensity of transmitted beam
I_0	intensity of primary beam
k	force constant
K_{eq}	equilibrium constant
l	optical path length
n	an integer (0,1,3...)
N	number of scans
n_i	amount of the substance
p	pressure
P_i	partial pressure
P_{TOT}	total pressure
R	universal gas constant
S	entropy
SNR	signal to noise ratio
T	temperature
Tr	transmitance
U	internal energy
V	volume
v	moving mirror velocity
$\bar{v}$	wavenumber of the absorbed peak
W	light wavenumber
x	molar concentration

List of Publications

1. D. Siche, **K. Kachel**, R. Zwierz, S. Golka, A. Vodopyanov, I. Izotov, S. Golubev, K.-P. Franke, P. Sudhoff, D. Gogova; *Chlorine-free plasma-based vapor growth of GaN*, Physica Status Solidi (c), vol. **9**, p. 440, 2012

2. **K. Kachel**, M. Korytov, D. Gogova, Z. Gałązka, M. Albrecht, R. Zwierz, D. Siche, S. Golka, A. Kwaśniewski, M. Schmidbauer, R. Fornari; *A new approach to free-standing GaN using $\beta - Ga_2O_3$ as a substrate*, CrystEngComm, vol. **14**, p. 8536, 2012

3. R. Zwierz, S. Golka, **K. Kachel**, D. Siche, R. Fornari, P. Sennikov, A. Vodopyanov, A.V. Pipa; *Plasma enhanced growth of GaN single crystalline layers from Ga vapor*, Crystal Research and Technology, vol. **48**, p. 186, 2013

4. O. B. Gadzhiev, P. Sennikov, A. Petrov, **K. Kachel**, S. Golka, D. Gogova, D. Siche; *The role of NH_3 and hydrocarbon mixtures in GaN pseudo-halide CVD: a quantum chemical study*, Journal of Molecular Modeling, vol. **20**, p. 2473, 2014

Acknowledgements

Being a Ph.D. candidate was one of the greatest challenges, adventure and at the same time pleasure in my professional life. Without help from countless people the completion of my thesis would not be possible. Therefore, here I would like to express my gratitude.

Prof. Dietmar Siche for his support and sharing a knowledge, for the patience while helping to lead this thesis to the final form. Also for giving me the possibility to work in IKZ on such a great topic.

Dr. Sebastian Golka deserves special gratitude for sharing his outstanding know how on designing and constructing machines and using it during the reactors construction. For giving an ideas and many fruitful discussions. For being great office-mate and helping me to survive abroad.

Dr. Radoslaw Zwierz for his support in the lab and sharing ideas.

Prof. Roberto Fornari and **Prof. Matthias Bickermann** for supporting this research, for their supervision and help with improving this thesis.

Dr. Michał Boćkowski for his constructive criticism.

Dr. Maxim Korytov and **Dr. Martin Albrecht** for conducting TEM measurements and introducing me to electron microscopy, also for many fruitful discussions.

Dr. Zbigniew Galazka for supplying the $\beta - Ga_2O_3$ substrates.

Mr. Reiner Nitschke, **Mr. Julius Brömel** and **Mr. Gerd Schadow** for the support in the technical aspect of the work.

Dr. Daniela Gogova for introducing me to the crystal growth community, and for sharing her know how on the crystal growth and characterization methods.

Mr. Albert Kwasniewski and **Dr. Martin Schmidtbauer** for performing XRD measurements and discussing of results.
Mr. Detlef Klimm for explanation of the FactSage software and many fruitful discussions.
Mr. Klaus Irmscher for introduction to the FTIR setup.
Mr. Bernd Spotowitz, **Mr. Uwe Kupfer** for super fast and efficient machining and manufacturing of the parts.
Mr. Uwe Jendritzki, **Mr. Peter Lange** and **Ms. Petra Krause** for support of the set-ups designing, discussing and solving the technical problems.
Prof. Peter Sennikov for supporting the FTIR measurement.
Mr. Münter Friedemann and **Mr. Jens Klose** for ensuring the lab safety and functioning.
Mr. Mattia Capriotti for his sense of humor, fruitful discussions and sharing the motivation to work.
Dr. T. Schulz, Mr. T. Markurt, Mr. S. Mohn, Ms. Andrea Lepper, Ms. Birgit Ruthenberg, Dr. Maike Schröder, Ms. Elvira Thiede, Dr. Carsten Hartmann, Mr. Sven Heron, Mr. Uwe Rehse, Dr. Jürgen Wollweber, Mr. Mario Ziem for their support during every day work

Group of colleagues and friends in **Unipress** for warm welcome and sharing their knowledge about HVPE growth of GaN. For many fruitful discussions and giving me answers to nearly all of the countless questions. For showing me how the worldwide best GaN crystals are grown and giving possibility of being the equally treated member of their great team.

All people involved in supporting any aspect of this work, but not mentioned here.

Last but not least to my wife, friends and family for continuous support and for giving me constant motivation.

Selbstständigkeitserklärung

Ich erkläre, dass ich die vorliegende Arbeit selbstständig und nur unter Verwendung der angegebenen Literatur und Hilfsmittel angefertigt habe.

Ich habe mich an keiner anderen Universität um einen Doktorgrad beworben und besitze keinen entsprechenden Doktorgrad.

Ich habe Kenntnis der dem Verfahren zugrunde ligenden Promotionsordnung der Mathematisch-Naturwissenschaftlichen Fakultät der Humboldt-Universität zu Berlin.

Berlin, den 13. November 2014 Krzysztof Kachel